5-2024

Design, Fabrication, and Characterization of Advanced High-power Single-mode 9xxnm Semiconductor Lasers

Xiaolei Zhao
xiaolei@g.clemson.edu

DESIGN, FABRICATION, AND CHARACTERIZATION OF ADVANCED HIGH-POWER SINGLE-MODE 9XXNM SEMICONDUCTOR LASERS

A Dissertation
Presented to
the Graduate School of
Clemson University

In Partial Fulfillment
of the Requirements for the Degree
Doctor of Philosophy
Photonics Science and Technology

---

by
Xiaolei Zhao
May 2024

Accepted by:
Dr. Lin Zhu, Committee Chair
Dr. Hai Xiao
Dr. Judson D. Ryckman
Dr. Lianfeng Zhao

ABSTRACT

This thesis presents the comprehensive design, fabrication, and demonstration of advanced high-power, high-efficiency single-mode semiconductor lasers operating at a wavelength of 9xxnm. We begin with the design of the laser epitaxial structure, serving as the cornerstone for achieving high-power high-efficiency lasers. Our methodology integrates a semi-analytical calculation model, which accounts for Longitudinal Spatial Hole Burning (LSHB) and Two-Photon Absorption (TPA) effects, facilitating a thorough exploration of how design parameters influence output power and conversion efficiency. This approach offers an effective and time-efficient epitaxial structure optimization strategy compared to conventional full 3D simulation models.

Subsequently, we demonstrate high-power, high-efficiency ridge waveguide (RW) lasers leveraging the optimized epitaxial structure. The RW lasers, with ridge width of 7μm and cavity length of 4mm, exhibit kink-free output and near-Gaussian far-field profiles with the maximum power outputs surpassing 1.6W. Notably, their efficiency demonstrates minimal decline with increasing current, maintaining a remarkable efficiency of 60.2% at 1.52W. Additionally, we introduce narrower RW lasers fabricated with an optimized epitaxial structure featuring reduced aluminum content in the p-cladding layer. The RW lasers, with ridge width of 5μm and cavity length of 5mm, exhibit kink-free near diffraction limit single-mode laser output up to 1W, accompanied by a high efficiency of 59.3%.

To achieve single-transverse-mode laser output in wider emission aperture for higher maximum achievable output power, we propose the triple ridge waveguide (TRW)

laser structure, utilizing the principle of unbroken supersymmetry (SUSY). This innovative design incorporates lossy auxiliary waveguides to effectively suppress unwanted higher-order modes within the laser cavity. By precisely engineering the structural parameters of the TRW, we achieve significant modal discrimination, ensuring stable single-mode lasing. Experimental results demonstrate near-diffraction-limited output in the proposed TRW laser, validating the efficacy of our mode filtering mechanism. To further enhance mode discrimination in practical applications, we propose the introduction of trapezoidal deep-etched trenches in the auxiliary waveguide. These trenches serve to convert guided modes into leaky modes, effectively increasing propagation loss for undesired higher-order modes. This enhancement facilitates more stable single-mode operation, particularly at high power outputs.

Moreover, in response to the increasing demand for highly coherent, low phase noise on-chip laser beams within integrated optics, we employ the self-injection locking technique to combine our demonstrated high-power ridge waveguide Fabry–Pérot (FP) lasers with silicon nitride photonic integrated circuits (PICs). Our experiments yield a stable narrow-linewidth single-frequency laser output with a fiber-coupled power of up to 3.5mW, accompanied by an impressive SMSR exceeding 48dB and an intrinsic linewidth smaller than 25kHz.

Our research provides valuable insights into the advancement of high-power, high-efficiency, single-mode semiconductor lasers, with promising applications across the field of photonics and telecommunications.

ACKNOWLEDGMENTS

First of all, I extend my heartfelt gratitude to all those individuals who have ever helped me throughout my PhD journey.

My deepest appreciation goes to my supervisor, Dr. Lin Zhu, whose invaluable instruction, inspiration and profound insights have been instrumental in shaping my research. Under his guidance, I have gained invaluable knowledge and expertise in the field of photonics, for which I am truly privileged and grateful.

I extend my sincere thanks to Dr. Hai Xiao, Dr. Judson D. Ryckman, and Dr. Lianfeng Zhao for their invaluable contributions as my dissertation committee members. Their insightful feedback and guidance have significantly enriched my research endeavors.

I am indebted to my colleagues for their unwavering support and collaboration throughout my academic pursuit. It has been an honor to work alongside such dedicated individuals, and I am profoundly grateful for their collective efforts.

Additionally, I express my profound gratitude to my friends whose support and companionship have been a source of strength and encouragement throughout my PhD journey.

Last but not least, heartfelt thanks are extended to my family for their enduring love and unwavering support.

TABLE OF CONTENTS

LIST OF TABLES

LIST OF FIGURES

Chapter 1

INTRODUCTION

1.1 Background and motivation

Numerous emerging industry and military applications demand compact and mobile laser systems with high power and brightness, accompanied by reduced size, weight, and power consumption (SWaP). Current High Energy Laser (HEL) systems heavily depend on spectrally beam combined fiber laser technologies, boasting high output power but suffering from the challenges such as relatively low electrical-to-optical efficiency (approximately 40%) and a substantial footprint. Semiconductor diode lasers, capable of directly converting electrical current into laser light, present appealing features including high power conversion efficiency, compactness, reliability, a broad wavelength range, and cost-effectiveness [1-3]. The advancements in direct diode laser systems hold significant promise in meeting the demands of the next generation of high-efficiency HEL systems.

Recent achievements include direct diode laser systems delivering multi-kilowatts of output power by multiplexing a cluster of broad-area emitters using beam shaping optics or beam combining techniques [4-6]. However, these systems fall short of

providing the desired high brightness due to the low beam quality of individual broad-area diode emitters. Consequently, the development of a high-power, high-efficiency single-mode diode emitter becomes crucial for the next generation HEL systems. A significant challenge lies in the conflicting design requirements for single-mode operation and high-power output. High-power operation necessitates a large optical mode size to avoid catastrophic optical damage (COD) and facilitate heat dissipation. Conversely, single-mode operation requires a narrow lateral waveguide to cut off higher-order modes. Additional challenges arise from carrier-induced index suppression, thermal lensing, and spatial hole burning effects, potentially leading to mode instabilities at high injected current levels, resulting in kinks in the light-output (IL) curves, beam steering, and beam-quality degradation [7-10].

In the domain of cutting-edge high-power diode lasers, the preferred wavelength range typically falls within 900nm to 1100nm. This range is favored not only for applications such as pump sources for ytterbium and erbium [11], optical communication [12], atmosphere sensing [13], and direct diode material processing [14] but also for the enhanced reliability associated with decreasing photon energy [15]. This dissertation specifically focuses on constructing an edge-emitting single-mode diode laser with high output power, high efficiency, and good beam quality, operating at the wavelength of 9xx nm.

Moreover, there is a surging demand across diverse cutting-edge technologies for on-chip laser sources featuring narrow linewidths and low phase noise. Their provided highly coherent and stable laser beams holds the potential to significantly enhance the

capabilities, efficiency, and reliability of communication systems [16-18]. Additionally, these advancements extend to emerging application areas such as LIDAR for autonomous vehicles, remote sensing, on-chip optical computing, and more [19-21]. Leveraging the inherent ease of integration of semiconductor lasers, this dissertation also focuses on exploring high-power, narrow linewidth semiconductor lasers by hybrid integrating our Fabry-Perot (FP) lasers with photonic integration circuit chips, aiming to advance on-chip functional photonic circuits and other integrated photonics applications.

1.2 Dissertation outline

To achieve high-power, high-efficiency single-mode semiconductor lasers, we begin with the design of the epitaxial structure, serving as the cornerstone for optimal laser performance. Chapter 2 delves into the essential considerations and strategic approaches for designing the epitaxial structure, with a focus on achieving high power and efficiency semiconductor lasers. We propose an optimization approach for the Extreme Double/Triple Asymmetric Epitaxial Structure, incorporating Longitudinal Spatial Hole Burning (LSHB) and Two-Photon Absorption (TPA) effects. This approach presents a notably more efficient and time-saving optimization method when compared to a full 3D simulation model. Chapter 3 covers the fabrication, packaging, and characterization techniques for our high-power laser diodes. Moving to Chapter 4, we focus on demonstrating high-power, high-efficiency single-mode ridge waveguide (RW) lasers by leveraging the developed ETAS epitaxial structure from Chapter 2. To enhance single spatial mode operation at high output power, we propose an advanced filtering mechanism in the form of a triple-ridge waveguide semiconductor laser based on

supersymmetry in Chapter 5. The chapter extensively covers the principles, design methodologies, and the experimental results related to the TRW lasers. Furthermore, we introduce an innovative design that incorporates embedding deep trenches in the auxiliary waveguide region, advancing the capabilities of the TRW laser. Finally, in Chapter 6, we further utilize the self-injection locking technique to hybrid integrate our high-power RW lasers with photonic integrated circuits (PICs). This integration aims to achieve high-power on-chip narrow-linewidth single-frequency laser output, addressing the growing demand for advanced applications in integrated optics, telecommunications, sensing technologies, and beyond.

Chapter 2

EPITAXIAL DESIGN FOR HIGH-POWER HIGH-EFFICIENCY DIODE LASERS

In this chapter, we will begin by presenting the fundamental configuration of semiconductor diode lasers and the phenomenological laser model describing the behavior of semiconductor lasers. Epitaxial design plays a critical role in realizing high-performance semiconductor lasers. Following this, we will explore the key considerations and strategic approaches for designing epitaxial structure aiming at achieving high power and efficiency semiconductor lasers. Lastly, we propose an optimization approach for the Extreme Double/Triple Asymmetric Epitaxial Structure based on Longitudinal Spatial Hole Burning (LSHB) and Two-Photon Absorption (TPA) effects. The endeavors within this chapter are instrumental in establishing a robust platform for subsequent research and development.

2.1 Basic semiconductor laser concept

2.1.1 Semiconductor laser structure

A semiconductor diode laser, characterized by its stacked structure of epitaxial layers, utilizes semiconductor as gain media, achieving optical amplification through stimulated emission at an interband transition under conditions of a high carrier density in the conduction band. Compared to other types of lasers, semiconductor lasers offer distinct advantages [22, 23]: firstly, semiconductor lasers are the only type capable of converting electrical energy into light energy; semiconductor lasers' basic structure, optical amplification, resonant cavities, and optical waveguides, all can be realized on a compact semiconductor microchip, facilitating chip-level integration; semiconductor lasers outperform other solid-state and gas lasers in terms of gain and electro-optical efficiency due to their substantially higher density of states in the energy bands; and the fourth benefit is the capability of semiconductor lasers to cover a wide spectrum of lasing wavelengths.

Figure 2.1 illustrates a schematic diagram of an edge-emitting semiconductor diode laser. The semiconductor epitaxial structure is typically grown on n-doped substrate. A p-n structure or p-i-n structure is formed through appropriate doping of the different epitaxial layers, thereby enabling the carrier transport. To achieve efficient light emission, it is required to employ direct band-gap semiconductors as the active medium [24]. The active region should exhibit a lower energy gap than the adjacent p or n layers, ensuring that electrons or holes are confined within potential wells in the active area. These adjacent layers, which form potential barriers, are referred to as confinement layers.

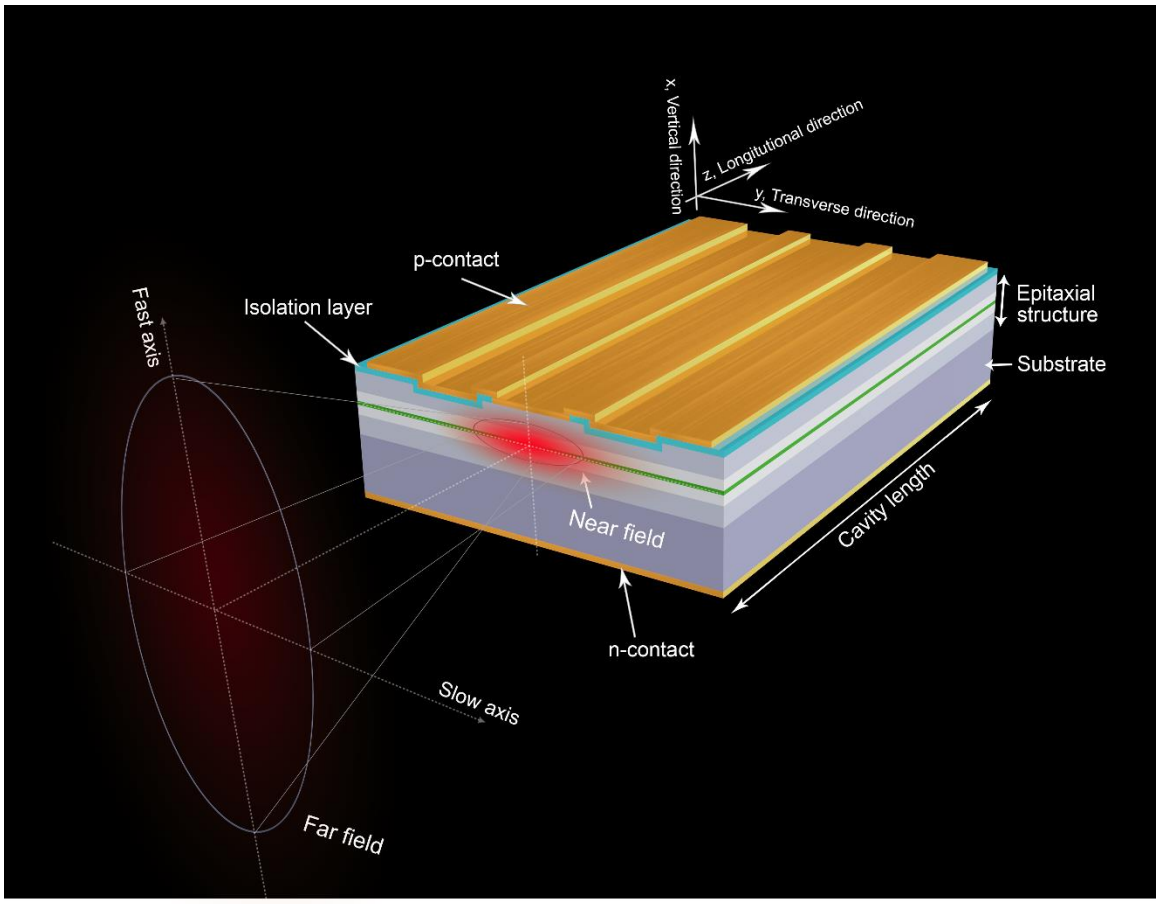

Figure 2.1 Schematic diagram of an edge-emitting semiconductor laser

Modern diode lasers typically use either a quantum well (QW) or quantum dot (QD) as the active region. The utilization of QWs as the active region provides several advantages. Firstly, within a quantum well, the density of states exhibits a stepped distribution, resulting in a significantly higher differential gain and a substantial reduction in threshold current, along with an increased modulation frequency. By varying the thickness of the quantum well, it is possible to alter the sub-level positions within the well, allowing for wavelength tuning within a certain range. Since the well's width is typically smaller than the electron and hole diffusion lengths, it effectively confines

carriers within the well, leading to improved injection efficiency and the ease of population inversion, consequently lowering the threshold current [25, 26]. Quantum well lasers also exhibit superior temperature characteristics compared to standard double heterostructure lasers.

As discussed above, the active region is embedded in the confinement layers with a wider bandgap. Then the confinement layers are embedded between two cladding layers with even larger bandgap. This configuration is primarily employed due to the phenomenon that materials with wider bandgaps tend to exhibit lower refractive indices. Additionally, the confinement layers and cladding layers, featuring wider bandgap energies than the active region, are almost transparent for the light generated during the stimulated emission process. Consequently, the epitaxial structure designed for carrier confinement and transport inherently builds up an optical waveguide, enabling effective optical mode confinement around the active region in the vertical direction. Generally, lateral optical mode confinement is commonly realized through index-guiding or gain-guiding, which we will discuss in more details in the subsequent chapter.

The remaining essential condition for semiconductor lasers to generate laser light is to create a resonant cavity that provides positive feedback. The most common method for achieving a resonant cavity in semiconductor lasers is to directly cleave the laser crystal along two plane that are perpendicular to the active region. These cleaved facets can act as reflective mirrors, between which light reflects back and forth, resulting in optical amplification. For a semiconductor laser to reach threshold and emit laser output (light amplification from stimulated emission), the gain in the active region must be

increased to the point where it compensates all the propagation and mirror losses, so that the electric field exactly replicates itself after one round trip in the cavity, that is, the lasing condition should be fulfilled. For meet the magnification part, the cavity gain per roundtrip equals the cavity loss per roundtrip [27]:

$$R_f R_b \exp\left[2L\left(g_{\text{modal}} - \alpha_i\right)\right] = 1 \tag{2.1}$$

where L represents the cavity length, R_f and R_b represent the reflectivities of the front and back cavity mirrors, g_{modal} represents the mode gain within the cavity, and α_i denotes the internal optical loss. The phase part of the lasing condition is described by (2.2):

$$m\lambda = 2n_{eff}L \tag{2.2}$$

where λ is the modal wavelength in the laser cavity, m is an integer corresponding to the longitudinal mode number, and n_{eff} denotes the effective index of the optical mode.

2.1.2 Phenomenological laser model describing semiconductor diode lasers

The behaviors of semiconductor diode lasers are commonly described using a phenomenological approach, employing a set of coupled rate equations related to photon density, carrier density, and optical gain. The standard one-dimensional (1D) rate equation set generally assumes uniform longitudinal distributions of carrier and photon densities within the laser cavity and can be expressed as follows [27]:

$$\frac{dN}{dt} = \frac{\eta_i I}{qV} - \frac{N}{\tau} - v_g g N_p \tag{2.3a}$$

$$\frac{dN_p}{dt} = \Gamma v_g g N_p - \frac{N_p}{\tau_p} \tag{2.3b}$$

Here, N and N_p respectively represent the carrier and photon densities in the active region. I is defined as the injection current, q as the electron charge, v_g as the photon group velocity and $V = dWL$ as the active region volume with d, W, and L respectively being the active layer thickness, stripe width, and cavity length.

η_i is referred to as the injection efficiency or the internal quantum efficiency, which refers to the fraction of the terminal current generates carriers within the active region [27]. Note that this definition encompasses all the carriers injected into the active region, not solely those participating in radiative recombination. This definition is frequently inaccurately stated in the existing literature. Current leakage is the factor contributing to the reduction of η_i. Carrier leakage occurs when carriers escape from the active region through processes such as thermionic emission or lateral diffusion before undergoing recombination. Consequently, this leakage results in a loss of carriers within the active region that could otherwise contribute to light generation. In semiconductor lasers, the recombination mainly involves stimulated recombination, spontaneous recombination, nonradiative recombination of free-carriers on defects (Shockley-Read-Hall) and Auger recombination. Consequently, η_i can be determined by dividing the integral of the total recombination rate, which comprises the sum of the four mentioned recombination processes, within the active region beneath the p contact, by the injection current.

τ represents the carrier lifetime and is typically expressed as: $1/(A+BN+CN^2)$, where the three terms respectively characterize the Shockley-Read-Hall, spontaneous radiation, and Auger recombination contributions.

g stands material gain in the active region, which is highly dependent on carrier concentration N. The carrier concentration when material gain is zero is referred to as the transparent carrier concentration, denoted as N_{tr}. Γ is the confinement factor, exhibiting the overlap of the optical transverse mode with the active region. Then the optical modal gain $g_{\text{modal}} = \Gamma g$.

τ_p is the photon lifetime. τ_p can be calculated by use of the relation $1/\tau_p = v_g(\alpha_i + \alpha_m)$, where $\alpha_m = -1/(2L)\ln(R_f R_r)$ is the mirror loss. As introduced in the last section, α_i represents the internal optical loss, which mainly comes from the scattering and free carrier induced absorption (FCA). FCA generally increases with the injection current because the carrier density does not pin at threshold but increases with the injection current, i.e., the carrier non-pinning effect [28, 29].

For the steady state, i.e. $dN_p/dt = 0$ and $dN/dt = 0$, we can find the values of N_{th} by solving equation $\Gamma g(N_{th}) = \alpha_i + \alpha_m$. Then the threshold current I_{th} can be further obtained by applying $N_p = 0$ into (2.3a). The idealized output power can be calculated from

$$P_{out}(I > I_{th}) = \frac{\hbar\omega}{q}\eta_d[I - I_{th}] \tag{2.4}$$

where $\eta_d = \eta_i \dfrac{\alpha_m}{\alpha_m + \alpha_i}$ is defined as the differential quantum efficiency (DQE). Due to the increase in internal loss α_i with rising injection current and temperature, DQE decreases as the current and temperature increases.

The slope efficiency is another crucial parameter that characterizes the performance of semiconductor lasers. It signifies the optical output power per unit increase in injection current after the laser has reached the threshold current. Its unit is

expressed as watts per ampere (W/A). Note that the slope efficiency is not equal to the DQE, and many publications tend to confuse them. Slope efficiency and DQE both decrease as the injection current increases. However, slope efficiency is typically employed to describe the experimentally measured current-light (IL) curve, while DQE is a parameter defined in simulations and calculations. It's important to highlight that in equation (2.4) used to derive the DQE, the threshold current I_{th} is current-dependent. Yet, in practical experiments, we can only determine a fixed threshold current. In this sense, the slope efficiency should encompass the impact of changes in DQE and threshold current with varying injection currents.

Semiconductor lasers are optoelectronic devices that directly convert electrical energy into light energy. In comparison to solid-state, gas and fiber lasers, they exhibit higher electrical-to-optical conversion efficiency. Therefore, the optical-electrical conversion efficiency is a parameter of great concern for semiconductor lasers. The electric-optic (EO) conversion efficiency η_c, also known as power conversion efficiency (PCE), quantifies how effectively the total electric power P_{total} supplied to the laser is transformed into optical output power P_{out} and is expressed as a ratio between these two powers:

$$\eta_c = \frac{P_{out}}{P_{total}} = \frac{P_{out}}{IV} \tag{2.5}$$

where V is the voltage of semiconductor laser. Voltage and other electrical characteristics of semiconductor devices can be simulated through the application of Poisson's equation within the drift-diffusion (DD) model. In upcoming section, we will take a more detailed

look at Equation (2.5) to provide a comprehensive explanation of the power distribution within the semiconductor laser.

2.1.3 Power distribution in semiconductor lasers

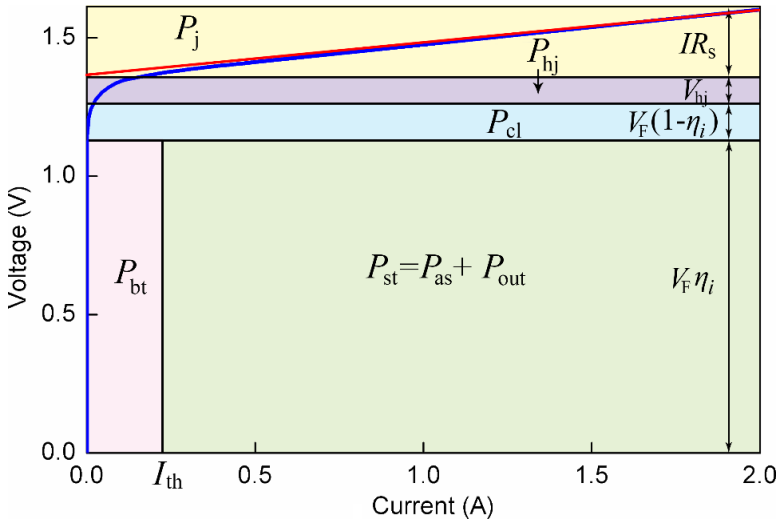

Figure 2.2 A typical IV curve of a semiconductor laser and its corresponding power distribution map

Figure 2.2 shows a typical current-voltage (IV) curve of a semiconductor laser and its corresponding power distribution map. The total power of a diode laser can be express as

$$\begin{aligned} P_{\text{Total}} &= I^2 R_s + V_0 I \\ &= I^2 R_s + \left(V_{hj} + V_F\right) I \\ &= I^2 R_s + V_{hj} I + V_F I(1-\eta_i) + V_F I \eta_i \\ &= I^2 R_s + V_{hj} I + V_F I(1-\eta_i) + V_F I_{th} \eta_i + V_F \left(I - I_{th}\right) \eta_i \\ &= P_j + P_{hj} + P_{cl} + P_{bt} + P_{st} \\ &= P_j + P_{hj} + P_{cl} + P_{bt} + \left(P_{as} + P_{out}\right) \end{aligned} \tag{2.6}$$

where R_s, V_0, and V_F symbolizes the series resistance, the built-in voltage, and the quasi

Fermi voltage, respectively. $P_j = I^2 \cdot R_s$ represents the generated Joule heat, $P_{hj} = V_{hj} \cdot I$ represents the voltage loss due to heterojunction band structure, $P_{cl} = V_F \cdot I \cdot (1-\eta_i)$ denotes the carrier leakage loss, $P_{bt} = V_F \cdot I_{th} \cdot \eta_i$ accounts for the non-radiative loss below the threshold, and $P_{st} = V_F \cdot (I-I_{th}) \cdot \eta_i$ represents the stimulated radiation power. Among this, only a portion of the stimulated radiation power contributes to the useful laser output P_{out} and the remaining part P_{as} is dissipated due to the internal optical loss caused by carrier absorption and scattering.

In Figure 2.2, the total power map is divided into various subregions, each corresponding to the various power terms mentioned earlier. To achieve high efficiency, it's essential to minimize all power losses, except for the useful output power. Various design strategies exist to minimize power wastage, each rooted in different physical factors, and some of these strategies may have conflicting requirements. For example, reducing the laser series resistance (by increasing doping levels) can help decrease Joule heat power P_{hj}, while reducing internal losses (by decreasing doping levels) can reduce absorption power P_{as}. The key challenge is to strike a balance between these strategies and optimize the final design.

2.2 High-power high-efficiency epitaxial structure design

In this section, we focus on discussing several critical considerations and potential solutions in the design of epitaxial structures with the aim of achieving both high power and high efficiency.

- **Minimizing internal optical loss**

Minimizing internal loss can effectively boost output power and conversion

efficiency. As previously mentioned, apart from the scattering loss, internal optical losses primarily arise from free carrier induced absorption (FCA). In epitaxial design, we can employ the following methods to mitigate FCA losses:

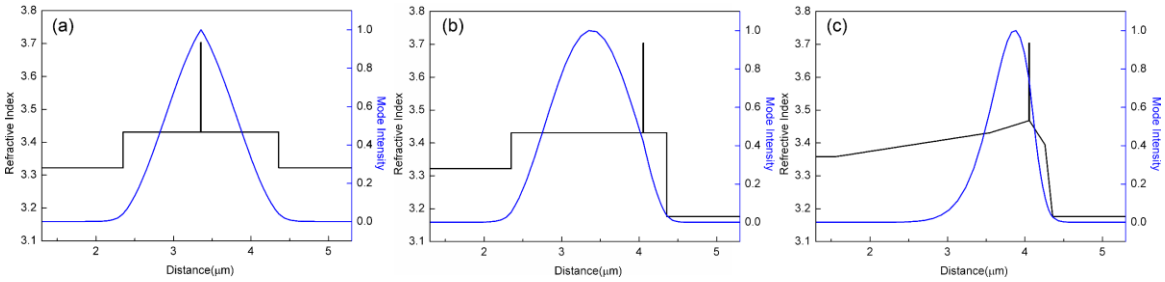

Figure 2.3 Vertical profiles of refractive index (left axis) and the fundamental mode intensity (right axis) of (a) a symmetric, (b) a conventional asymmetric and (c) a novel asymmetric waveguide epitaxial structure

1. *Asymmetric waveguide epitaxial structure combined with compositionally graded layer.* Considering that the absorption cross-section due to free holes in GaAs and AlGaAs materials at 9xxnm is approximately three times higher than electrons [26], shifting the optical mode towards the n-side is an effective method to reduce the internal loss. This can be achieved by carefully designing an asymmetric waveguide structure featuring a thick n-waveguide, a thin p-waveguide, and a large refractive index step at the waveguide-cladding interface on the p-side. In this manner, the resulting optical mode has minimal overlap with the p-doped region, thereby decreasing the overall internal loss. Traditional asymmetric large optical cavity waveguide structures inherently operate with a low optical confinement in the active region, leading to higher threshold current that limits their performance. We can implement of compositionally graded layers to offer more degrees of freedom in

manipulating the optical modal shape. Through introducing an asymmetrically graded-index waveguide and a separate confinement layer near the active region, the optical modal profile can be tailored for a higher optical confinement in the active layer while keeping internal loss at a low level. Figure 2.3 illustrates three distinct epitaxial waveguide designs: a symmetric waveguide structure (a), a conventional asymmetric waveguide structure (b), and a novel asymmetric waveguide structure (c) incorporating compositionally graded layers. Simulated results indicate that Design A exhibits the highest internal loss at 1.421 cm^{-1}. Design B helps to reduce the loss level, resulting in a much lower internal loss of 0.972 cm^{-1}. The design C outperforms the others, achieving the lowest internal loss of 0.324 cm^{-1}. Moreover, the calculated confinement factors for these three structures are 0.75%, 0.268% and 0.853%, respectively, signifying a substantial enhancement in optical confinement factor than the conventional asymmetric laser structure.

2. *Avoiding abrupt heterojunction by inserting compositionally graded layer*. Incorporating a compositionally graded layer between the waveguide layer and the confinement layer can enhance the quality of the heterojunction interface, resulting in fewer crystal defects and subsequently reducing scattering losses due to abrupt structural changes. Furthermore, this can mitigate carrier blocking arising from abrupt energy level shifts, thus enhancing overall carrier injection efficiency.
3. *Optimizing the doping profile*. An undoped waveguide layer proves advantageous in reducing internal optical losses. Nonetheless, in epitaxial designs featuring a wide waveguide structure, an excessively thick undoped waveguide layer can elevate the

series resistance and voltage, subsequently diminishing electro-optical conversion efficiency. Consequently, it is necessary to optimize the doping profile of the waveguide layer.

- **Reducing Carrier Leakage Loss**

Carrier leakage has a direct impact on internal quantum efficiency and threshold current density, which deteriorate the electro-optic characteristics, temperature characteristics, and other aspects. Carrier leakage in semiconductor lasers can result from carriers escaping from the active region (vertical carrier leakage) and lateral current spreading (lateral carrier leakage). In order for injected carriers to reach the active region, they must pass through multiple heterojunctions in the epitaxy structure, formed by the barriers between the cladding layer, the waveguide layer and the quantum well. The drift diffusion model can be used to resolve the carrier distribution near these heterojunctions and analyze the vertical carrier leakage effect. Electrons are more prone to leakage than holes because of their much smaller effective mass and higher mobility. A portion of electrons escapes from the quantum well to the p-waveguide layer and even the cladding layer, leading to the increased non-radiative recombination loss and degraded thermal performance. Therefore, in the process of epitaxial structure design, we should monitor the carrier distribution and combine it with an analysis of internal quantum efficiency and non-radiative recombination rate, trying to reduce carrier leakage. First, we need to ensure that there is a sufficient barrier height between the quantum well and the confinement layer. For InGaAs/AlGaAs/GaAs lasers, we can achieve this by increasing the aluminum content or by using GaAsP barrier layers. As shown in Figure 2.4, the

GaAsP barrier effectively suppresses carrier leakage and contributes to lower the device voltage. Moreover, a compositionally graded layer can be applied to optimize the heterojunction interface state, reduce the voltage drop and hence achieve high carrier injection efficiency.

In the lateral direction, current spreading is associated with the electrode width. Lateral current spreading is of relatively lower significance in the case of broad-area diodes; however, for ridge waveguide lasers, the lateral spreading typically cannot be ignored. The implementation of a double isolation trench structure helps to suppress lateral carrier leakage and thus increase the injection efficiency.

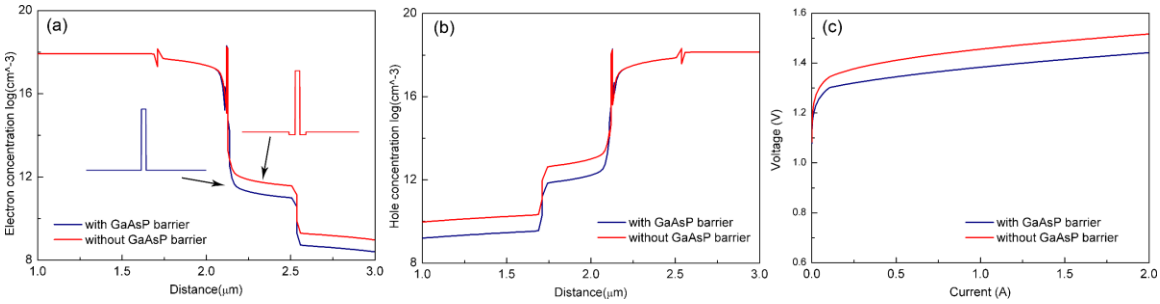

Figure 2.4 Comparison of (a) electron concentration distributions, (b) hole concentration distributions at I = 1.6A, and (c) IV curves with and without GaAsP barrier

- **Reducing Series Resistance**

The series resistance plays an important role in determining the efficiency and the thermal performance of semiconductor lasers. The resistance R for each layer within the epitaxial structure can be calculated using the formular $R = d/\left[LW\left(ne\mu_e + pe\mu_p \right) \right]$, where d, μ_e and μ_h represent the layer thickness, electron mobility, and hole mobilty, respectively. In conventional epitaxy design, the p-side resistance accounts for a large

proportion of the total device resistance because holes have much lower mobility than electrons. Therefore, employing an asymmetric waveguide epitaxial structure with a thin p-waveguide layer can reduce the device's series resistance. Another approach to reduce the series resistance is to use lower aluminum (Al) composition, which contributes to reduce both electrical resistance and thermal resistance, and thus can improve the PCE efficiency at high current injection. To demonstrate this effect, a broad-area diode laser structure is investigated with various Al compositions, as depicted in Figure 2.5(a). As expected, the slope of the VI curve (i.e. the series resistance) notably decreases as the Al composition decreases, resulting in an increase in PCE. However, reducing the Al composition also decreases the barrier height and might potentially lead to carrier leakage, as shown in Figure 2.5(c). An optimized value for the Al fraction should balance the resistance and slope efficiency, ultimately maximizing the PCE.

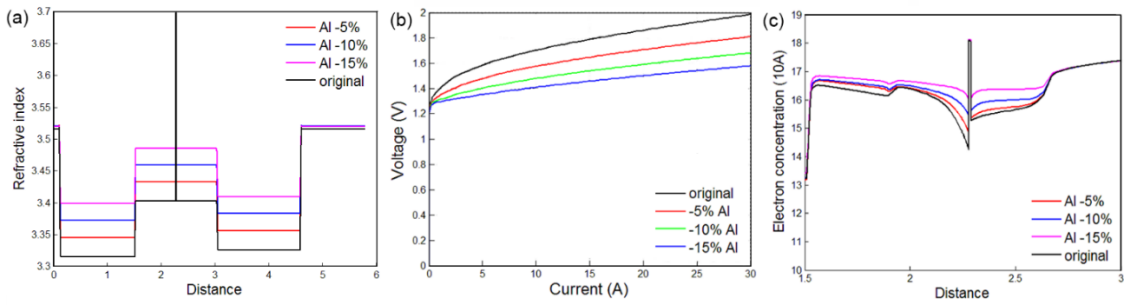

Figure 2.5 Effect of aluminum fraction on the performance of a 100μm wide broad-area laser: (a) the refractive index profile, (b) the simulated IV curve, and (c) electron concentration distribution at I = 10A with reduced Al compositions.

- **Catastrophic optical mirror damage (COMD)**

COMD represents a crucial issue limiting the maximum output power and reliability of single-mode diode lasers. Several specific factors may contribute to the

occurrence of COMD, with the most important being the high optical power density near the cavity surface. In epitaxial design, the large optical cavity (LOC) structure proves effective in reducing the optical power density by expanding the mode size, thereby raising the output power level where COMD occurs. This reduction in optical power density also helps to lower the photon absorption loss caused by scattering, diffraction, and impurity absorption at the heterojunction interfaces.

Another significant factor contributing to COMD is the presence of surface states, that is, intrinsic defects on the cavity surface. Surface defects and impurities act as traps, capturing nearby electrons and forming non-radiative recombination centers. The increase in non-radiative recombination results in a rapid elevation of the cavity surface temperature, causing a reduction in the surface bandgap and an increase in photon absorption. This, in turn, accelerates non-radiative recombination, setting off a positive feedback loop that ultimately leads to COMD. Hence, it is crucial to reduce the non-radiative recombination rate and improve the quality of diode laser cavity surfaces. To address this issue, strategies such as implementing a current injection-free region near the cavity facet and applying passivation treatments and coatings to the laser facet can be employed. These methods pertain to laser structure design rather than epitaxial design.

- **Active Region Design Optimization**

The quantum well (QW) design exerts a profound influence on the emission wavelength and ultimate performance of diode lasers. The limited thickness of QWs enables the use of materials with varying compositions, which may not always perfectly match with the lattice constant of the substrate, leading to the introduction of strain to the

QW. Depending on the relative lattice constants of the QW material to the substrate, the strain can be either compressive or tensile stress. The strain in the QW layer significantly alters the two-dimensional energy dispersion of the electronic sub-bands. Compared with the lattice matched QW, the strained QW can provide higher differential gain at the same injection level, enabling lower threshold current density. Compressive strain increases the band gap, which raises to the threshold energy for Auger recombination and consequently suppresses heat generation. This enhances the temperature stability of the semiconductor laser. Moreover, the strained QW also shows better laser polarization properties and better noise suppression, accompanied by a reduction in the linewidth enhancement factor.

A multiple QW (MQW) structure generally provide a higher optical confinement factor and a larger gain factor than a single QW design. Given a certain COMD power-density value P_{COMD}, the maximum output power P_{max} of the diode laser can be expressed by the formula:

$$P_{max} = \frac{d}{\Gamma} W \left(\frac{1-R}{1+R} \right) P_{COMD} \tag{2.7}$$

where d and W represent the thickness and width of active region. Γ is the optical confinement factor, and R is the reflectivity of the front and rear facets. It can be found from above equation that increasing the value of $\frac{d}{\Gamma}$ is a straightforward way to increase the maximum output power of the device. However, as the number of quantum wells increases, the values of d and Γ increase simultaneously, so a MQW design does not necessarily correspond to higher maximum output power.

2.3 Optimization of Extreme Double/Triple Asymmetric Epitaxial Structure based on LSHB and TPA effects

Extreme, double/triple asymmetric (EDAS/ETAS) structures are a new advanced epitaxial structure introduced in recent years, characterized by an ultra-thin p-waveguide design and a large waveguide and cladding index difference in p side. They offer distinct advantages in enhancing Power Conversion Efficiency (PCE) through the reduction of series resistance, minimal optical loss, and the suppression of power saturation [30-37]. An EDAS-based BAL with a 100 μm stripe width and 4 mm cavity length was reported to reach a power conversion efficiency of 60% at 12W CW power under room temperature conditions [33]. An ETAS-based 100μm-width BAL with optimized confinement factor delivered an efficiency of 63% at 14W [34]. It was also recently reported that very high efficiency > 70% was achieved from the 4mm-long 186um-wide ETAS based BAL by balancing the confinement factor and front facet reflectivity [35]. Further increase of the output power and efficiency is challenging.

High-power laser diodes often feature front and rear facets coated with highly asymmetric reflective films, aiming to increase the slope efficiency and extract most of optical power from the front facet. Furthermore, they typically incorporate longer cavities to reduce thermal resistance, thus improving thermal management and enhancing overall reliability. However, these two design features result in an inhomogeneous distribution of photon and free carrier densities and thus non-uniform optical gain profile along the laser longitudinal direction, leading to the so-called longitudinal spatial hole burning (LSHB) effect [38-42] and a reduction in laser output power. Moreover, two-photon absorption (TPA), a nonlinear process in semiconductors, is also considered to be one of the

fundamental factors limiting the maximum achievable optical power in high-power laser diodes [43-45].

In this section, we propose a semi-analytical calculation model that incorporates LSHB and TPA effects to gain an in-depth understanding of how laser design parameters affect the output power and the conversion efficiency, thereby achieving design optimization of EDAS/ETAS-based diode lasers. To make the model better reflect the real situation, the commercial software LASTIP is used to provide the basic L-I and V-I curves of the designed BAL devices without considering LSHB and TPA effects. LASTIP is a two-dimensional (2D) simulator for edge-emitting Fabry-Perot laser diodes, which can self-consistently combines multi-mode wave guiding, carrier transport, quantum well optical gain, and heat flow in the transverse plane.

Our work provides a promising semi-analytical method for obtaining high-power and high-efficiency ETAS-based BALs, which is much more efficient and time-saving compared with a full 3D simulation model.

2.3.1 Comparative Analysis of Epitaxial Structures Disregarding LSHB and TPA Effects

We first explore the output characteristics of three representative epitaxial structure designs (conventional, EDAS, and ETAS) when LSHB and TPA effects are not considered. The refractive index and the fundamental vertical mode intensity profiles for the three epitaxial designs are plotted in Figures 2.6(a-c), respectively. The three epitaxial structures use the same active region designs of a compressively strained InGaAs single

quantum well (thickness d = 8nm) and GaAsP barriers. Their main difference lies in the AlGaAs waveguide structure. As for the conventional design, the active region is placed in a symmetric waveguide structure with the waveguide core thickness of 800nm. The EDAS design has a very asymmetric waveguide structure with thick graded index (GRIN) n-waveguide layers, very thin GRIN p-waveguide layers and a large index step at the waveguide-cladding interface on the p-side. The resulting fundamental mode shifts to the n-side and thus has only a small overlap with the p doped region, leading to much less optical free carrier absorption loss. The thin p-layers also ensure lower series resistance and carrier leakage. On the other hand, the EDAS structure is generally inherited with a small optical confinement factor and thus low modal gain. In the EDAS design, as shown in the inset of Figure 2.6(b), the thicknesses of the n- and p-GRIN waveguide layers closest to the active region (in the following we refer to them as the confinement layers) are equal, that is, t_n=t_p. Different from EDAS, the ETAS design adopts an additional (third) asymmetry ($t_n \neq t_p$) in the waveguide structure, as illustrated by Figure 2.6(c), providing a new degree of freedom to tailor the optical modal shape and optimize device performances. For example, by adjusting the size of t_n with other structural parameters unchanged, we can flexibly control the confinement factor to vary in a relatively large range while not introducing excessive light intensity in the p-doped region, thereby maintaining the low optical loss level.

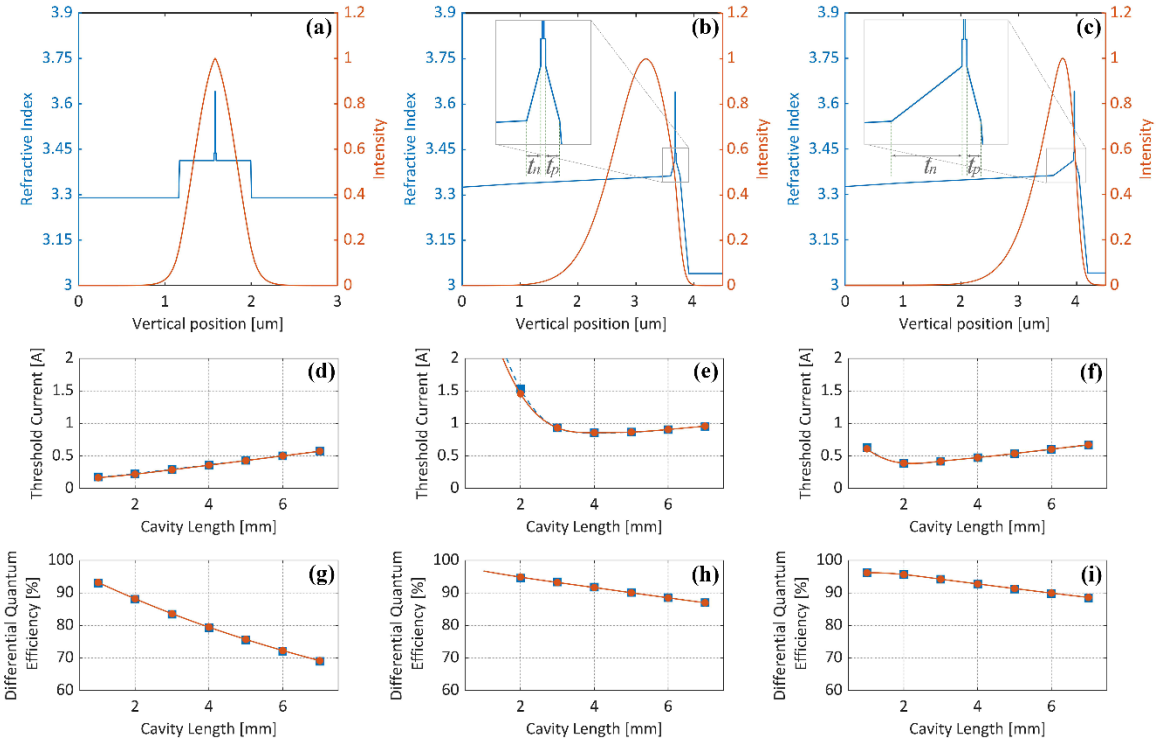

Figure 2.6 Refractive index (Blue, left axis) and fundamental vertical mode intensity (Red, right axis) profiles for (a) a conventional epitaxial structure, (b) an EDAS (t_n = t_p = 70nm) and (c) an ETAS (t_n = 350nm, t_p = 70nm) epitaxial design. Calculated threshold current (d-f) and differential quantum efficiency (g-i) of broad area lasers based on the three designs as a function of laser cavity length (stripe width W = 100μm, reflectivities of the front and rear facet R_f = 1% and R_r = 98%). Blue rectangle and red circle symbols are respectively the simulation results from LASTIP and the calculation results by solving equation (2.3). Dashed and solid curves are the corresponding spherical linear interpolations.

LASTIP simulations for BALs based on the above three epitaxial designs are performed first. We assume the p-side contact width to be W = 100μm. Full 2D simulations are conducted to better reveal the current spreading and multi-lateral mode behavior in BALs. The vertical optical mode is calculated by solving the vertical Helmholtz wave equation. The effective index method is used to treat the multi-lateral

modes with ten transverse standing waves considered. The reflectivities of the front and rear facets are respectively fixed as R_f = 1% and R_r = 98%. The extracted threshold currents of the three BAL designs as a function of laser cavity length are plotted as the blue rectangles in Figures 2.6(d-f). As expected, the threshold currents of the conventional design are smallest among the three designs since it has the largest confinement factor. It can also be found that its threshold current gradually increases as the cavity length L increases. Although the reduction in mirror loss will result in a lower threshold current density J_{th} for a longer cavity length, the increase in the contact area eventually causes the threshold current I_{th} to increase with the increase of cavity length. EDAS design has the largest threshold current on account of its smallest confinement factor. In addition, for the short cavity lengths, i.e. when the mirror loss is relatively high, the small modal gain in EDAS makes it more difficult to reach the threshold condition. Therefore, the threshold current of the EDAS-based BAL increases sharply when the cavity length L is smaller than 3 mm. For the ETAS design, the third asymmetry helps to increase its confinement factor and thus threshold currents are effectively reduced. Figures 2(g-i) show the simulated DQE of the three BAL designs versus cavity length at the injection current I = ~3A. Owing to the relatively high internal loss, the DQE of the conventional BAL design drops significantly as the cavity length increases, which indicates that this design needs further improvement for high power operation. The low internal loss level in the EDAS and ETAS-based BALs enables them to maintain a high DQE even with a long cavity length, so they have great potential for high power applications.

Following this, we extract several key parameter values from LASTIP simulations, including the internal quantum efficiency η_i, the carrier density dependent material gain curve $g(N)$, the confinement factor Γ, and current-dependent internal loss $\alpha_i(I)$. These values will be used to solve rate equation set (2.3). The red circles depicted in Figures 2.6(d-i) represent the calculated results obtained by solving equation set (2.3) using the parameters extracted from LASTIP. In the calculations, the coefficients of Shockley-Read-Hall $A = 7.1\times10^{8}$ s^{-1}, spontaneous radiation $B = 1\times10^{-10}$ cm^3s^{-1}, and Auger recombination $C_n = C_p = 2\times10^{-30}$ cm^6s^{-1} are taken from literature [31]. It is evident that, apart from minor discrepancies in threshold current values in the case of a short cavity, the calculated results closely align with LASTIP simulation results. This demonstrates that the 1D rate equations are reliable for predicting the power output characteristics of BAL diodes employing various epitaxial structures.

2.3.2 Equations with LSHB and TPA Effects

For high-power diode lasers, the carrier and photon inhomogeneity along the longitudinal direction significantly affects the laser characteristics especially at high injection currents, which is not considered in the standard rate equation set (2.3). In addition, given the high optical light intensities in high-power diode lasers, the nonlinear optical losses caused by TPA effect become important and non-negligible under high injection levels. More specifically, the TPA effect involves, in fact, two mechanisms contributing to the nonlinear optical losses [45]: (i) the direct effect of nonlinear loss due to TPA, and (ii) the indirect effect of the TPA serving as another source of carrier

accumulation in semiconductor lasers, creating additional optical losses through free carrier induced absorption.

The direct TPA loss at any local point in the laser cavity can be given as [45]

$$\alpha_{TPA}^{\text{direct}}(x,z)=\beta(x)\Psi(x,z) \tag{2.8}$$

where $\beta(x)$ [cm/GW] denotes the TPA coefficient. β is material composition dependent, so here it shows a dependence on the vertical coordinate x. For the specific calculation method of β, please refer to Ref [43]. $\Psi(x, z)$ represents the local light intensity. If it is assumed that the optical power is uniformly distributed in the lateral direction, then $\Psi(x, z)$ can be written as $\Psi(x,z)=P(z)\varphi^2(x)/W$, where $P(z)$ is the local power and $\varphi^2(x)$ is the normalized optical mode intensity profile, i.e., $\int_{-\infty}^{+\infty}\varphi^2(x)\mathrm{d}x=1$. The modal loss caused by the direct TPA effect can be calculated as

$$\begin{aligned}\alpha_{TPA}^{\text{direct, modal}}(z)&\approx\int_{-\infty}^{+\infty}\alpha_{TPA}^{\text{direct}}(x,z)\varphi^2(x)\,\mathrm{d}x\\&\approx\frac{P(z)}{W}\int_{-\infty}^{+\infty}\beta(x)\varphi^4(x)\,\mathrm{d}x\end{aligned} \tag{2.9}$$

The local power $P(z)$ can be expressed by the average photon density in the active region. That is,

$$P(z)=\frac{dW}{\Gamma}\left[v_g\hbar\omega N_p(z)\right] \tag{2.10}$$

After substituting (2.10) into (2.9), we obtain that

$$\begin{aligned}\alpha_{TPA}^{\text{direct, modal}}&\approx\frac{d}{\Gamma}v_g\hbar\omega N_p(z)\int_{-\infty}^{+\infty}\beta(x)\varphi^4(x)\,\mathrm{d}x\\&\approx\beta_{TPA}^{\text{direct, modal}}N_p(z)\end{aligned} \tag{2.11}$$

with $\beta_{TPA}^{\text{direct, modal}} = \frac{d}{\Gamma} v_g \hbar\omega \int_{-\infty}^{+\infty} \beta(x) \varphi^4(x)\, \mathrm{d}x$ defined as the direct modal TPA coefficient. Figure 2.7 plots the dependance of the calculated direct modal TPA coefficient $\beta_{TPA}^{\text{direct,modal}}$ (blue, left axis) and the confinement factor Γ (red, right axis) of the ETAS epitaxy on the *n*-confinement layer thickness t_n. The confinement factor Γ increases monotonically with t_n. But its growth rate gradually slows down for relatively large values of t_n, indicating that Γ is close to its maximum achievable value. Continuing to increase Γ requires additional adjustments to the epitaxial layer composition. The calculated direct modal TPA coefficient $\beta_{TPA}^{\text{direct,modal}}$ shows a strong dependance on the epitaxial structure. As t_n increases, $\beta_{TPA}^{\text{direct,modal}}$ initially declines rapidly, reaching a minimum at t_n = 280 nm and increasing slightly thereafter.

As for the indirect TPA effect, its contribution to the optical internal loss is determined by the TPA-generated free electron density $\Delta N_{e,TPA}$ and hole density $\Delta N_{h,TPA}$. That is,

$$\begin{aligned} \alpha_{TPA}^{\text{indirect, modal}}(z) \approx \sigma_e \int_{-\infty}^{+\infty} \Delta N_{e,TPA}(x,z) \varphi^2(x)\, \mathrm{d}x \\ + \sigma_h \int_{-\infty}^{+\infty} \Delta N_{h,TPA}(x,z) \varphi^2(x)\, \mathrm{d}x \end{aligned} \tag{2.12}$$

where σ_e and σ_h are respectively the free-electron and free-hole absorption cross-sections. To obtain $\Delta N_{e,TPA}$ and $\Delta N_{h,TPA}$, we should solve the carrier transport equation of the full drift-diffusion model with the TPA generation term given by the TPA rate [45]:

$$G(x,z) \approx \frac{\beta(x)}{\hbar\omega} \left[\frac{P(z)^2}{W} \right] \varphi^4(x) \tag{2.13}$$

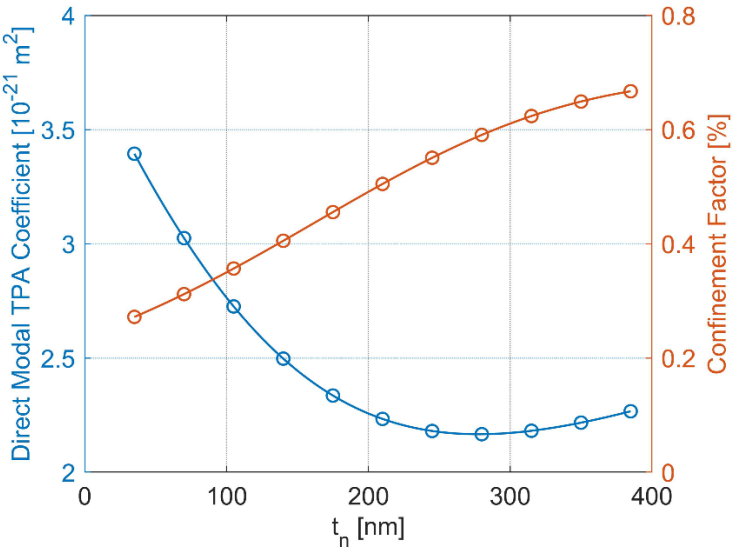

Figure 2.7 The calculated direct modal TPA coefficient $\beta_{\mathrm{TPA}}^{\mathrm{direct,modal}}$ (blue, left axis) and confinement factor Γ (red, right axis) of the ETAS epitaxy as function of the n-confinement layer thickness t_n.

The new version of LASTIP follows this model and automatically includes the TPA-generated free carrier density in its calculations if the TPA coefficient is properly defined. The definition of TPA coefficient in LASTIP is same as (2.11). Therefore, in this work we use LASTIP to calculate the TPA-generated free carrier density distribution $\Delta N_{e,TPA}(x)$ and $\Delta N_{h,TPA}(x)$. Note that the longitudinal direction z dependance of $\Delta N_{e,TPA}$ and $\Delta N_{h,TPA}$ is ignored as LASTIP is a 2D simulator. Figure 2.8(a) shows the calculated TPA-generated free carrier density distribution of 4mm-long ETAS BALs at injection current I = 40A. It can be observed that the TPA-generated free electrons and holes both mainly concentrate in the active region and the n-side cladding layer (especially around the interface where high doping begins). Using the data of $\Delta N_{e,TPA}(x)$ and $\Delta N_{h,TPA}(x)$, we can obtain the indirect TPA modal absorption by (2.12). Figures 2.8(b) and (c) respectively show the dependance of the calculated indirect TPA absorptions $\alpha_{TPA}^{\mathrm{indirect,modal}}$ of

4mm-long ETAS-based BALs on the injection current I and the n-confinement layer thickness t_n. As expected, $\alpha_{TPA}^{\text{indirect,modal}}$ increases with the injection current owing to the square term of power in the indirect TPA generation rate. The dependance of the indirect TPA absorption $\alpha_{TPA}^{\text{indirect,modal}}$ on t_n is similar to that of the direct one $\alpha_{TPA}^{\text{direct,modal}}$. The difference is that the position of the minimum of $\alpha_{TPA}^{\text{indirect,modal}}$ shifts towards a larger t_n value of ~315nm.

Taking into account the LSHB and TPA effects discussed above, the steady state 1D rate equations are modified as

$$\frac{\eta_i I}{qV} - \frac{N(z)}{\tau\left[N(z)\right]} - v_g g\left[N(z)\right]\left[N_p^+(z) + N_p^-(z)\right] = 0 \tag{2.14a}$$

$$\frac{dN_p^{\pm}(z)}{dz} = \pm\left\{\begin{array}{l}\Gamma v_g g\left[N(z)\right]N_p^{\pm}(z) - \\ \left[\alpha_i(I) + \alpha_{TPA}^{\text{indirect,modal}}(I)\right]N_p^{\pm}(z) \\ -\beta_{TPA}^{\text{direct,modal}} N_p^{\pm}(z)^2\end{array}\right\} \tag{2.14b}$$

where z stands for the longitudinal axis position, $N(z)$ is the local carrier density, $N_P^+(z)$ and $N_P^-(z)$ are forward and reverse propagating photon densities, respectively. Instead of the average mirror loss in the standard rate equation, the forward and reverse propagating photon densities in the modified equations should satisfy the boundary conditions at the front facet ($z = 0$) and the rear facet ($z = L$) to accommodate their spatial non-uniformity:

$$N_p^+(0) = R_f N_p^-(0) \tag{2.15a}$$

$$N_p^-(L) = R_r N_p^+(L) \tag{2.15b}$$

By solving the coupled differential equations with the boundary conditions, the output power is then determined as

$$P_{out} = v_g W \frac{d}{\Gamma} \hbar\omega \left[N_p^- (0)\left(1-R_f\right) + N_p^+ (L)\left(1-R_r\right) \right] \tag{2.16}$$

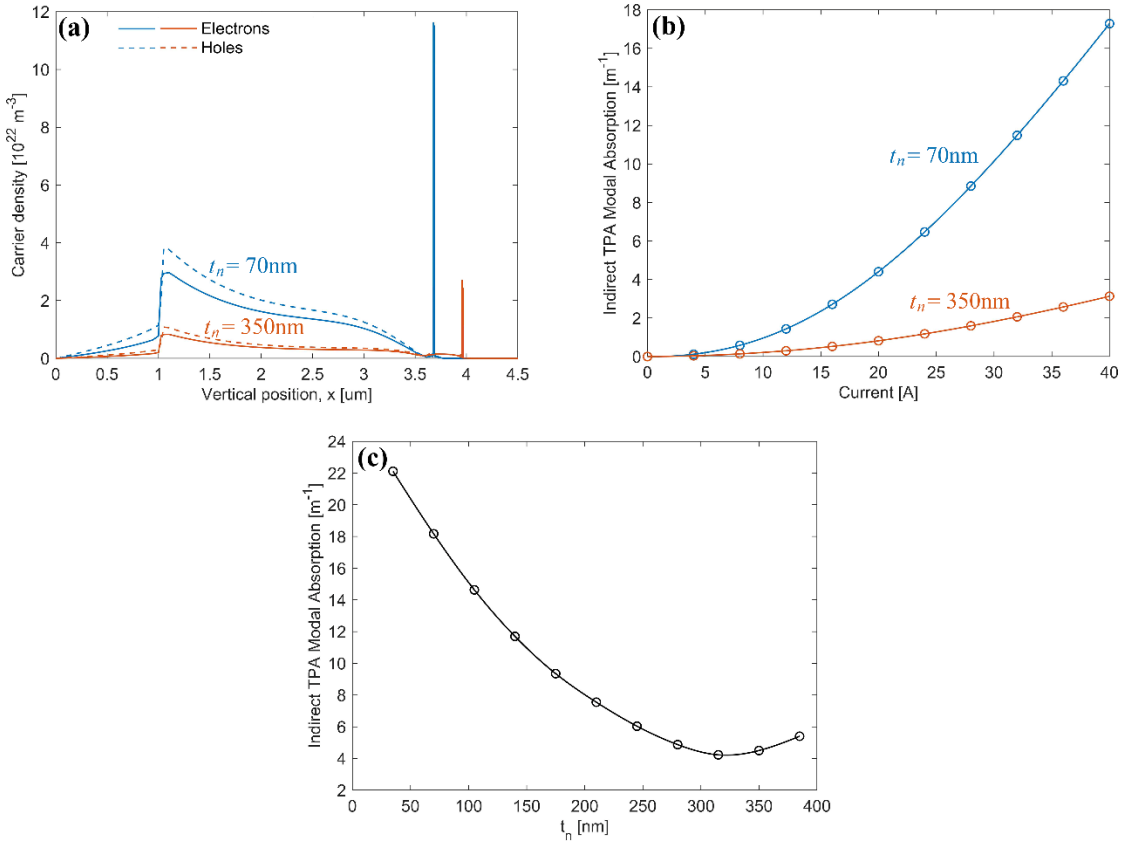

Figure 2.8 Calculated spatial distributions of TPA-generated free carrier densities at I = 40A (a), and dependance of indirect TPA absorption on injection current (b) for 4mm-long ETAS BALs. Blue: t_n = 70nm; and red: t_n = 350nm. (c) Calculated indirect TPA absorption as a function of the n-confinement layer thickness t_n at I = 40A.

2.3.3 Design Optimization for Pulsed Operation

Based on the rate equations with LSHB and TPA effects discussed in Section 2.3.2, we will investigate how the laser structural parameters of the ETAS-based BAL impact its output power and efficiency. In this section, we do not consider the impact of

thermal effects, which effectively corresponds to pulsed (quasi-CW) operation regime. The calculated *L-I* characteristics and conversion efficiencies for the representative EDAS and ETAS-based BALs with cavity length of 4mm are respectively plotted in Figures 2.9(a) and (d), where the dashed lines are the idealized results neglecting LSHB and TPA effects, the dashed-dotted lines are the calculation results with only LSHB effect, and the solid lines are the results with both LSHB and TPA effects. The reduction in output power and conversion efficiency can be seen after LSHB and TPA effects are taken into account. The LSHB and the TPA power penalties (*i.e.*, the percentages of power reductions caused by the LSHB and the TPA effects respectively) for the two designs are also calculated in dependence on the injection current, as shown in Figure 2.9(c) and (f). It can be seen that LSHB effect dominates the power penalty in the low bias regime. As discussed in previous references [42, 44], the magnitude of the LSHB penalty is directly correlated with the internal loss value. Since the internal loss of the EDAS/ETAS design is rather low, the performance degradation induced by the LSHB effect is not very serious. The calculated LSHB power penalties of the EDAS-based and ETAS based BALs are ~3.75% and ~2.5% respectively at the injection current of 30A. The LSHB power penalty values remain relatively stable (the LSHB penalty of the EDAS design even decreases) with the increasing injection current. Conversely, the TPA power penalty grows with the injection current owing to the increasing photon density and outweighs the LSHB power penalty in the high injection regime.

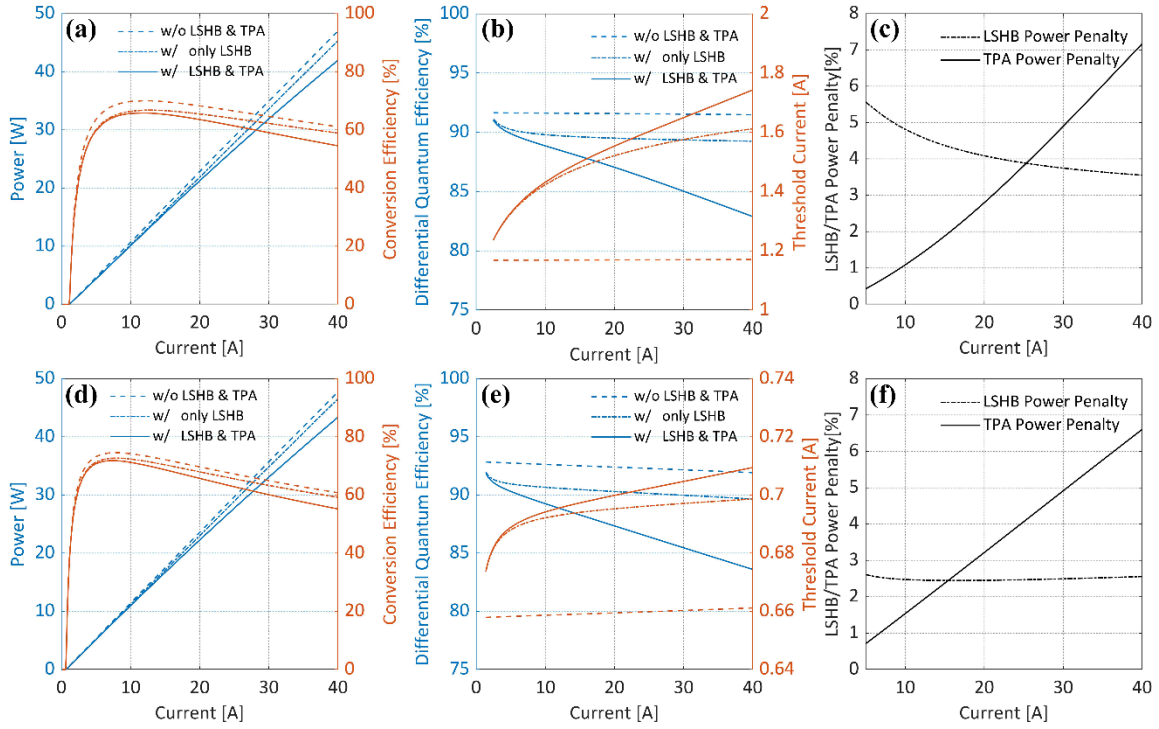

Figure 2.9 Calculated L-I characteristics (Blue, left axis) and conversion efficiency (Red, right axis) for (a) the 4mm-long EDAS-based BAL design with t_n = t_p = 70nm and (d) the 4mm-long ETAS-based BAL design with t_n = 350nm and t_p = 70nm; DQE (Blue, left axis) and threshold current (Red, right axis) versus injection current for (b) the EDAS BAL and (e) the ETAS BAL; Calculated LSHB and TPA power penalty versus injection current for (c) the EDAS BAL and (f) the ETAS BAL. Here thermal effects are not considered.

Although, as shown in Section 2.3.2, the calculated values of direct modal TPA coefficient $\beta_{TPA}^{\text{direct,modal}}$ and indirect TPA absorption $\alpha_{TPA}^{\text{indirect,modal}}$ of the EDAS epitaxy (t_n = 70nm) are much larger than those of the ETAS one with t_n = 350nm, the narrower modal shape (narrower near field) and thus higher photon density in the ETAS-based BAL results in roughly the same TPA power penalties for both designs (*e.g.*, the calculated TPA power penalties for the EDAS and ETAS designs at I = 30A are both around 4.9%). The current-dependent DQE and threshold current for the two devices are provided in

Figure 2.9(b) and (e) in order to better illustrate how the LSHB and TPA effects directly affect the laser output performance. As indicated by the figures, the LSHB effect accounts for most of the increase in the effective threshold current, whereas TPA just slightly increases the threshold current, indicating that the LSHB effect affects the non-stimulated recombination more than the TPA effect. Since the TPA effect affects the laser output power mainly via increasing the internal loss, that is, reducing the DQE, the drop in the DQE with the high injection current correlates to the increase in the TPA power penalty.

As for the EDAS design, the smaller confinement factor leads to a larger threshold current and thus a lower maximum conversion efficiency (~5.5% lower than the ETAS one). On the other hand, the conversion efficiency of the ETAS design drops faster at high injection currents due to the large resistance and the serious TPA effect. To find the optimal values of structural parameters for the highest output power and efficiency, we sweep the *n*-confinement layer thickness t_n from 35nm to 385nm. The sweeping results for the output power and efficiency are plotted in Figures 2.10(a) and (b), respectively. Clearly, the t_n value which leads to the maximum power and efficiency changes with the injection current. Figures 2.10(c-e) respectively show the output power (upper panel) and the conversion efficiency (lower panel) as a function of t_n at three different currents I =20A, 30A and 36A. Since the output power and efficiency values change slowly near the peak values, we define the 0.5% drop ranges of maximum output power and efficiency as the optimal t_n ranges, which are indicated as the translucent colored areas in Figures 2.10(c-e). It can be seen that a large t_n value is in favor of high

output power. As current grows and the TPA effect becomes more pronounced, the optimal t_n range shifts slightly to the smaller side. The optimal t_n ranges for the efficiency are lower than those for the output power. The overlaps of the translucent areas for the power and efficiency indicate the optimal ranges of the t_n parameter at the specific injection level. For I = 20A, 30A, and 36A, the optimal t_n range are centered at ~325nm, ~255nm, and ~240 nm, respectively. Taken together, for 4mm-length ETAS-based BAL under pulsed operating mode (i.e., no thermal effects) to achieve both high power and high efficiency in the current range of 20-36A, the optimal range of t_n is about 250-300nm.

The cavity length plays an important role in the performance of high-power diode laser. As discussed earlier, in the case of no LSHB and TPA effects, the threshold current generally increases and DQE decreases with the increase of cavity length. As a result, the achievable output power at a certain injection current decreases as the cavity length increases. Since LSHB and TPA effects are more serious as the cavity length increases, there is no doubt that under a certain injection current, the maximum output power will monotonically decrease with the cavity length, which is shown in the upper panels (left axis, hollow squares) of Figure 2.11. To better illustrate the contribution of LSHB and TPA effects to the power reduction, Figure 2.12 plots the LSHB and TPA power penalty at the maximum output power versus cavity length. For longer cavity length, the longitudinal spatial non-uniformity is more severe. It is evident from Figure 2.12 that both LSHB and TPA power penalties at maximum output power monotonically increase with cavity length. Furthermore, the TPA power penalties under different cavity lengths

are higher than the LSHB ones at these three injection currents, which is consistent with the previous discussion that the TPA effect dominates in the high injection regime.

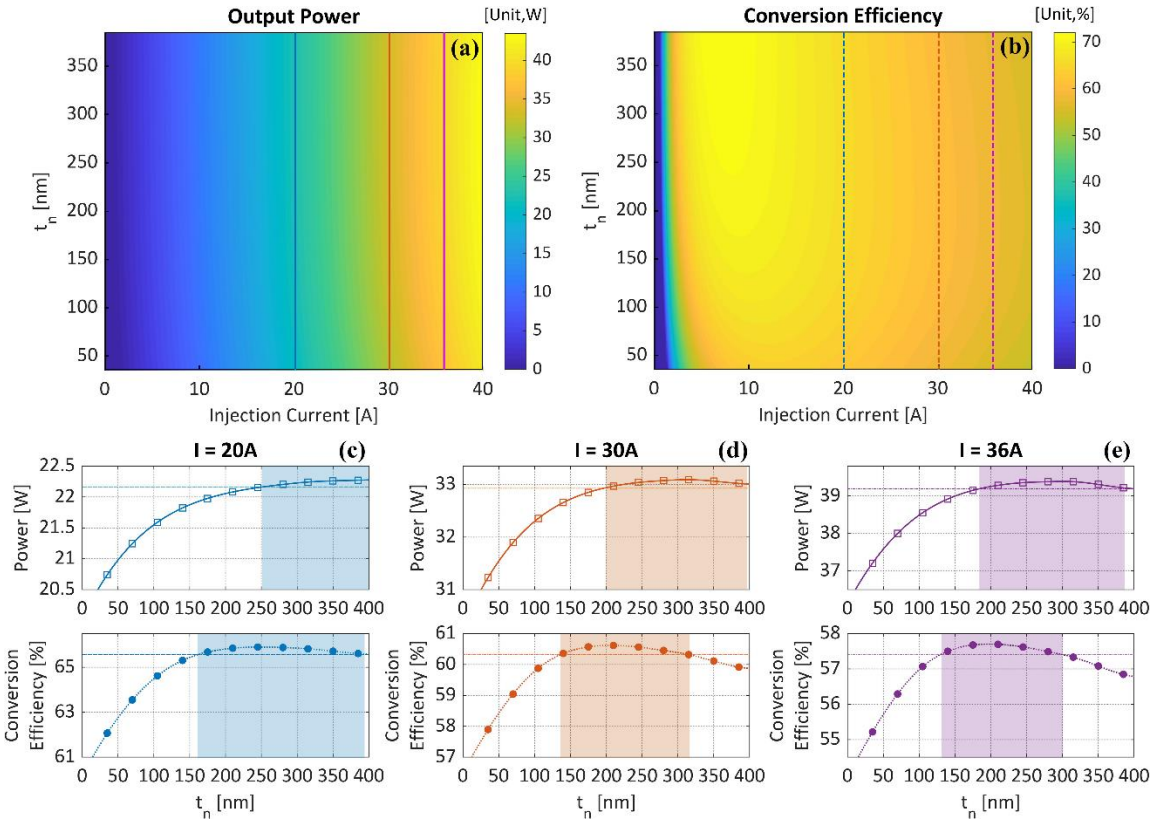

Figure 2.10 The sweeping results for the output power (a) and conversion efficiency (b) of the 4mm-long ETAS-based BAL as a function of the injection current I and n-confinement layer thickness t_n with both LSHB and TPA effects taken into account. (c-e) Output power (upper panel) and conversion efficiency (lower panel) as a function of t_n at various injection currents: (c) I = 20A, (d) I = 30A, and (e) I = 36A. Thermal effects are not considered here. The rectangle and circle symbols are the calculation results, and the solid and dotted curves show the corresponding spherical linear interpolations.

On the other hand, longer cavity means lower device resistance, and thus higher conversion efficiency might be achieved. The conversion efficiencies of the ETAS-based BALs in dependence on the cavity length are also plotted in the upper panels (right axis,

filled circles) of Figure 2.11, which clearly illustrate the trade-off between the maximum achievable power and efficiency at a given injection level. At the three targeted injection currents I =20A, 30A, and 36A, the maximum efficiencies are found at cavity length of 5mm, 5mm, 6mm, respectively. Moreover, with the increase of pumping level, the impact of cavity length on conversion efficiency becomes more obvious. At I =36A, the highest efficiency can reach 58.7% with a cavity length of 6mm, whereas the highest efficiency is only 56.4% with a cavity length of 3mm. The length-dependent optimal t_n overlap range for the power and efficiency are shown as the translucent colored areas in the middle panels of Figure 2.11 and the corresponding optimal confinement factor overlap ranges are shown in the lower panels. As can be seen, the optimal t_n and confinement factor Γ range varies little with different cavity lengths at a specific injection current. The optimal t_n and Γ range tends to get smaller overall as the current increases to reduce the increasing negative effects of LSHB and TPA. To enable the ETAS-based BAL to have the most favorable performance under pulsed high-power operation for various cavity lengths from 3mm to 7mm and for a wide current range from 20A to 36A, the optimal choices of t_n and Γ are around 300nm and 0.61%.

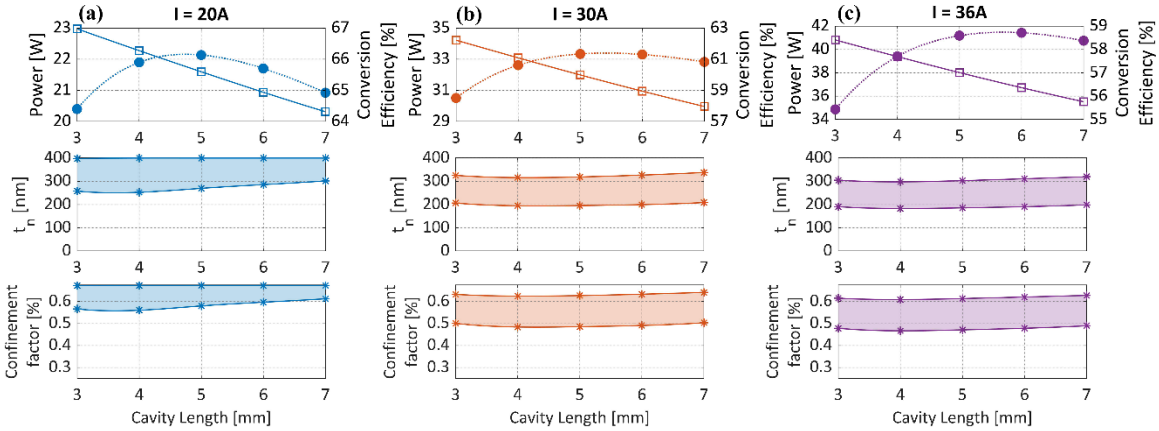

Figure 2.11 Upper panels: the highest output power (left axis, hollow squares) and the highest conversion efficiency (right axis, filled circles) under different injection currents: (a) I = 20A, (b) I = 30A, and (c) I = 36A. Middle/lower panels: the translucent areas show the overlap regions between the length-dependent optimal t_n/Γ ranges for power and efficiency under different injection currents. The symbols and curves respectively show the calculation results and the corresponding spherical linear interpolations. LSHB and TPA effects are included, while thermal effects are not considered here.

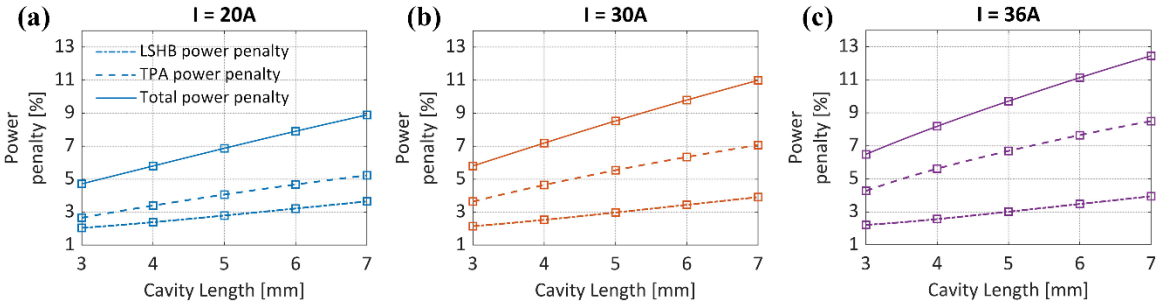

Figure 2.12 Calculated LSHB and TPA power penalties of ETAS-based BALs at the maximum output power (corresponding to the hollow squares in the upper panels of Figure 2.11) versus cavity length under different injection currents: (a) I = 20A, (b) I = 30A, and (c) I = 36A. (Thermal effects are not considered here)

2.3.4 Design Optimization with Thermal Effects

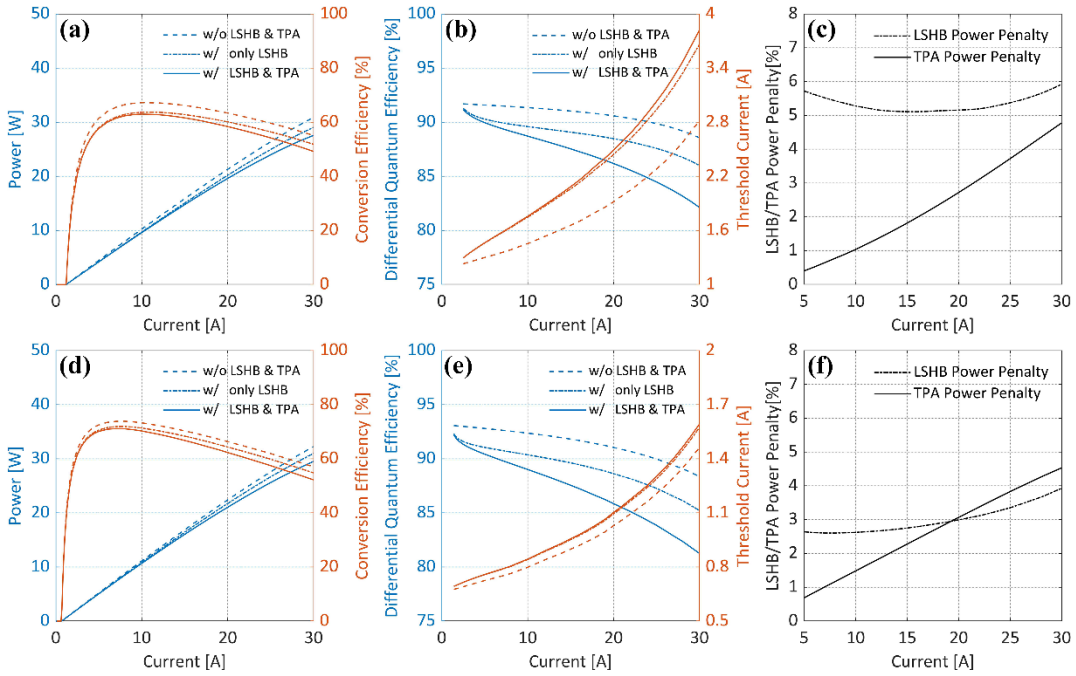

Figure 2.13 Calculated L-I characteristics (Blue, left axis) and conversion efficiency (Red, right axis) for (a) the EDAS-based BAL design with t_n = t_p = 70nm and (d) the ETAS-based BAL design with t_n = 350nm and t_p = 70nm; DQE (Blue, left axis) and threshold current (Red, right axis) versus injection current for (b) the EDAS BAL and (e) the ETAS BAL; Calculated LSHB and TPA power penalty versus injection current for (c) the EDAS BAL and (f) the ETAS BAL. Here thermal effects are included.

As for a diode laser operating under CW mode, self-heating is another critical factor that limits its output power and efficiency. In this section, we will investigate the laser performance of EDAS/ETAS-based BALs with LSHB and TPA effects under CW operation. LASTIP is used here to better address the thermal effects of BALs with different design parameters. The BALs are assumed to be mounted p-side down onto CuW submounts. The heat sink is assumed to be kept at room temperature of 298K. In the LASTIP simulation, we apply the bottom n-type GaAs substrate with zero outgoing heat flux. For the top p-type contact, we assume it to be connected to a thermal conductor

with a specified thermal conductance, the value of which is fitted from the experiment results in Refs [46, 47]. The extracted T_0 and T_1 characteristic temperatures of 4mm length ETAS-based BALs are 183.5K and 572.8K for t_n = 70nm, and 223.5K and 813.1K for t_n = 350nm, respectively, which show good agreement with the experimental results reported in [26, 28] that the epitaxial structures with higher confinement factors show relatively higher T_0 and T_1 values. To account for the thermal effects in the modified rate equation, we need to add the temperature and wavelength dependance to the material gain, that is, replace $g(N)$ with $g(N, T, \lambda)$, where T represents the temperature of the quantum well.

The calculated *L-I* and conversion efficiency curves of the representative 4mm-long EDAS and ETAS-based BALs after considering the thermal effects are shown in Figures 2.13(a) and (d). The corresponding current-dependent effective threshold current and DQE are also plotted in Figures 2.13(b) and (e), serving as an alternative representation of *L-I* characteristics. Since the CW-driven diode lasers usually have the thermal roll-over and break down at a lower injection level than those under the pulsed mode, we reduce the studied current range to 0-30A. It is worth pointing out that 30A is still an ambitious operation point for a CW-driven BAL with 100μm-wide stripe. According to state-of-the-art experiments, the sustainable range for CW operation is about 15-20A. It can be clearly seen that the effective threshold currents of both designs, especially for the EDAS design with a small confinement factor, rise substantially with increasing bias current. This is because as the junction temperature increases with the bias current, the broadening of the Fermi distribution leads to a decrease in material gain

[26]. To compensate the lower gain and the higher optical loss, the carrier density in the quantum well is increased (non-pinning) accordingly. This non-pinning effect of the carrier density results in increased carrier loss due to nonradiative recombination and carrier leakage, thereby leading to increased effective threshold current [29]. In addition, the increasing carrier density with temperature exacerbates the impact of LSHB.

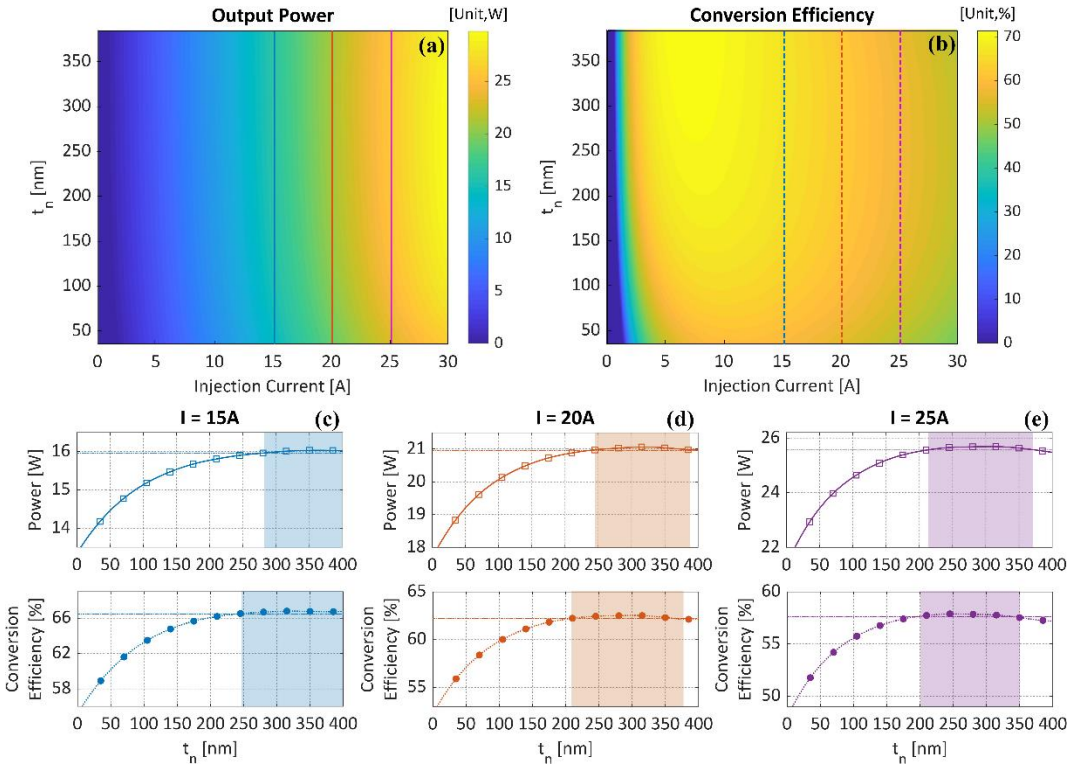

Figure 2.14 The sweeping results for output power (a) and conversion efficiency (b) (with both LSHB and TPA effects) of the 4mm-long ETAS-based BAL as a function of the injection current I and n-confinement layer thickness t_n after considering the thermal effects. (c-e) Output power (upper panel) and conversion efficiency (lower panel) as a function of t_n at various injection currents: (c) I = 15A, (d) I = 20A, and (e) I = 25A.

Figures 2.13(c) and (f) respectively shows the calculated LSHB and TPA power penalty as a function of bias current for the two designs with thermal effects, which

clearly show that the LSHB power penalty becomes larger than the case of no thermal effects. Moreover, the LSHB power penalty increases with bias in the high current region. TPA power penalties of both designs are basically the same as those in the case of no thermal effects. Accordingly, for the EDAS design with thermal effects, LSHB replaces TPA effect as the dominant effect in reducing output power within the targeted current range. The proportion of LSHB in the total power penalty of ETAS design is also considerably enhanced.

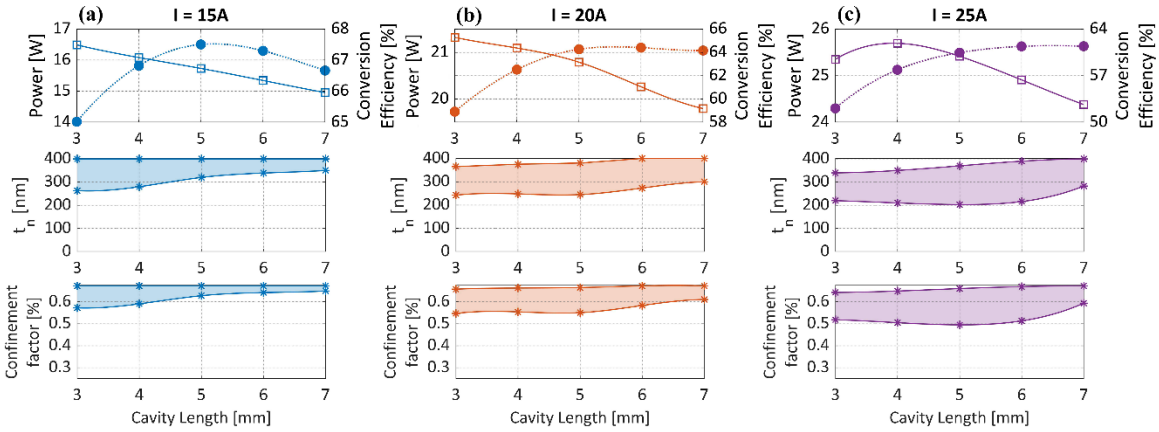

Figure 2.15 Upper panels: the highest output power value (left axis, hollow squares) and the highest conversion efficiency value (right axis, filled circles) as a function of the cavity length under different injection currents (a) I = 15A, (b) I = 20A, and (c) I = 25A; Middle/lower panels: the translucent areas show the overlap regions between the length-dependent optimal t_n/Γ ranges for power and efficiency under different injection currents. The symbols and curves respectively show the calculation results and the corresponding spherical linear interpolations. LSHB, TPA, and thermal effects are all included here.

To find the optimal confinement factor at which the joint effect of LSHB and TPA on the device are minimum, n-confinement layer thickness t_n is swept from 35nm to

385nm, as illustrated in Figures 2.14 (a) and (b). To better illustrate the change trend of optimal t_n with the pumping level, Figures 2.14(c-e) show the output power and conversion efficiency as a function of t_n at three different injection currents of I = 15A, 20A and 25A. Here we also use the colored translucent areas to denote the 0.5% drop range of maximum output power and efficiency. Compared with the sweeping results in the absence of thermal effects shown in Figure 2.10, it can be observed that the optimal t_n ranges for the output power and efficiency tend to overlap more in the presence of the thermal effects. For I = 15A, 20A, and 25A, the optimal t_n overlap range are centered at ~340nm, ~311nm, and ~280 nm, respectively. This result suggests that a relatively large t_n and confinement factor Γ should be adopted in the design of 4mm-long ETAS-based BALs under the CW mode, which is consistent with the experimental results in [29] that a high-Γ ETAS design is beneficial for improving CW and short pulse performance at high currents. As can be seen from Figure 2.14, there is considerable overlap (280nm-350nm) between the optimal t_n ranges for the power and efficiency at these three different currents, indicating a large design margin in practice to achieve both high power and efficiency over a wide current range. Note that the power and efficiency drop rapidly as t_n approaches the lower sweeping limit of 35nm. This is because the high nonradiative recombination in the low confinement factor design exacerbates the thermal effects, causing the rapid growth of effective threshold with the increase of the injection current.

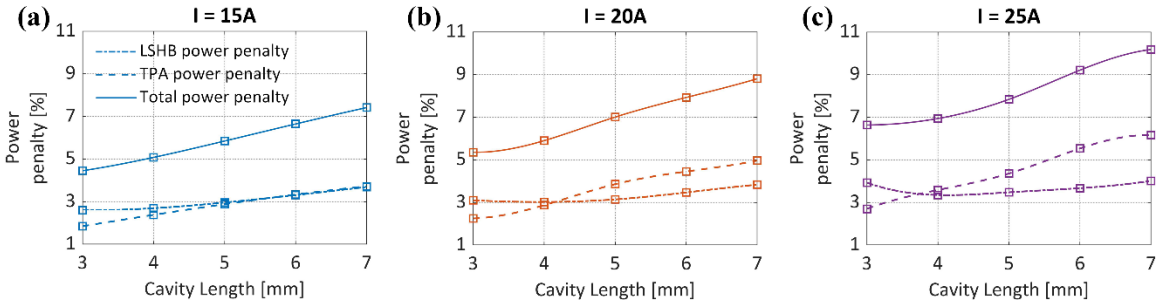

Figure 2.16 Calculated LSHB and TPA power penalties of ETAS-based BALs at the maximum output power (corresponding to the hollow squares in the upper panels of Figure 2.15) versus cavity length under different injection currents: (a) I = 15A, (b) I = 20A, and (c) I = 25A. (Thermal effects are considered here)

As mentioned earlier, the longer cavity length contributes to better thermal management owing to its lower thermal resistance. How to adjust the design parameters with different cavity lengths to achieve the best output performance of ETAS-based BALs under CW mode is studied. The calculated maximum output power and conversion efficiency of ETAS-based BAL as a function of cavity length under three different injection levels are plotted in the upper panels of Figure 2.15. Figure 2.16 shows the calculated LSHB and TPA power penalties at maximum output power versus cavity length. It can be noticed that the LSHB effect accounts for a larger fraction of the total power penalty for the shorter cavity length, where the thermal effects are more severe. The length-dependent optimal t_n and Γ overlap range for the power and efficiency areas are respectively shown in the middle and lower panels of Figure 2.15, Evidently, longer cavity lengths do help increase the conversion efficiency, especially at the higher injection level (e.g., I = 25A). For I = 20A/25A, the maximum efficiency is increased by 5.6%/9.3% by increasing the cavity length from 3mm to 5.5/7mm. Although at a certain

bias current, a slight decrease in the output power with the increase of cavity length can be observed, their correlation becomes very weak at high injection levels. Hence, a relatively long cavity length (5-6mm) is preferred for the ETAS-based BAL operating at high injection levels under the CW mode. As indicated by the middle and lower panels of Figure 2.15, the optimal t_n and confinement factor Γ ranges tend to be a bit larger overall as the cavity length increases. Overall, the optimal t_n/Γ value for the CW driven ETAS-based BALs to maintain the optimum performance over a wide range of injection current and cavity length are around 345 nm/0.645%.

2.3.5 Conclusion

Structural parameter optimization of EDAS/ETAS epitaxial designs for high-power and high-efficiency BALs is investigated by employing the modified rate equations with the LSHB and TPA effects taken into account. To better predict the performances of BALs based on different epitaxial structures, simulation software LASTIP is used to provide several key parameters that are required in rate equations, the TPA-generated free carrier densities for indirect TPA absorption calculation, the electric characteristics for conversion efficiency analysis, and thermal simulation under CW operation. The dependence of the two parameters describing the TPA effect in the modified rate equation—direct modal TPA coefficient $\beta_{\mathrm{TPA}}^{\mathrm{direct,modal}}$ and indirect TPA absorptions $\alpha_{TPA}^{\mathrm{indirect,modal}}$—on the n-confinement layer thickness t_n are discussed. It is found that, in the case of pulsed mode operation, *i.e.*, in the absence of thermal effect, TPA effect acts as the dominant power saturation mechanism at high injection currents. As for

the case of CW operation mode, the thermal effects exacerbate LSHB effect, and as a result, the proportion of LSHB power penalty to the total power penalty significantly boosts. For both cases, with or without thermal effects, relatively large values of n-confinement layer thickness t_n and confinement factor Γ are beneficial to improve the output power and efficiency. Calculation results suggest that the optimal t_n/Γ value for the ETAS-based BAL design to maintain the optimal performance over a wide range of injection current and cavity length are ~300nm/0.61% for the pulsed mode and ~345nm/0.645% for the CW mode. It is noteworthy that the level of the confinement factor mentioned in this article is a relative term. The confinement factors of the ETAS structures are generally relatively low compared with a conventional symmetric waveguide epitaxial structure. Regarding the optimal choice of cavity length, there is a trade-off between the maximum achievable power and efficiency. The maximum output power generally decreases as the laser cavity increases, whereas the optimal cavity length for maximum conversion efficiency is around 5-6mm depending on the injection level for both cases of with or without thermal effects. For the case of CW mode, the increase in cavity length only results in a slow decrease in maximum output power but greatly improves the conversion efficiency. For example, by choosing the optimal cavity length, conversion efficiency improvements of 5.6% and 9.3% can be achieved at I = 20A and 25A, respectively. The facet reflectance will also affect the optimization results, as the LSHB effect strongly depends on the difference between the reflectivities of the front and rear facets. The more unbalanced the reflectivity of the front and rear facets is, the more severe the LSHB effect is. Our work is important for realizing high-power and high-

efficiency BALs based on the EDAS/ETAS epitaxial structure as well as provides valuable guidelines for ongoing experimental implementation.

Chapter 3

FABRICATION, PACKAGING AND CHARACTERIZATION TECHNIQUES OF HIGH-POWER SEMICONDUCTOR LASERS

In this chapter, we will discuss the preparation processes we employ to fabricate both broad area lasers and ridge waveguide lasers. Following this, we will introduce the techniques associated with the packaging and mounting of high-power diode lasers. Lastly, we will delve into the measurement setup and characterization method of high-power semiconductor lasers.

3.1 Fabrication of Broad-area lasers and ridge waveguide lasers

The semiconductor laser fabrications for this study were conducted in the cleanrooms at Georgia Tech and Clemson University, or at the Masimo foundry for wafer-scale laser preparation.

3.1.1 Fabrication of broad-area lasers

Gain-guided broad area lasers achieve transverse optical confinement based on variations in the gain profile across the laser's active region, eliminating the need for constructing an optical waveguide, and thus they the simplest semiconductor lasers to fabricate. We typically fabricate broad-area lasers to evaluate the quality of an epitaxial wafer. Figure 3.1 summarizes the primary fabrication process of gain-guided broad area lasers.

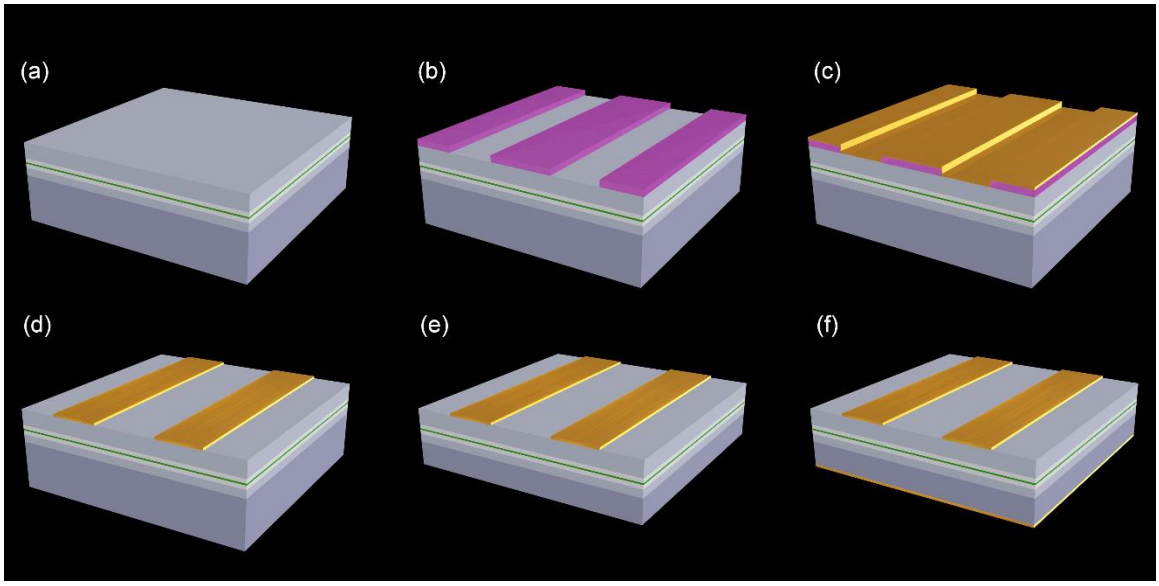

Figure 3.1 Fabrication processing flow of gain-guided broad-area lasers

Step (a): Surface cleaning.

It follows a standard cleaning process (Subject the sample to a 3-minute ultrasonic treatment in acetone, and then rinse sequentially by flowing acetone, Isopropyl Alcohol (IPA) and Deionized (DI) water) and a native oxide removal process. Due to long-term exposure to the air, epitaxial wafers develop a very thin oxide layer on their surfaces, which can sometimes hinder the formation of good Ohmic contacts. Therefore, we need

to remove them using a mild acid. Next, employ nitrogen gas (N_2) to remove the residual water and perform a dehydration bake at 180°C for 2-3 mins.

Step (b): Photolithography

The photolithography is carried out using either a mask aligner or a maskless aligner (MLA), and the photoresist can be ether positive or negative. Generally, the reverse trapezoidal profile created by negative photoresist is more advantageous for the lift-off process. Table 3.1 lists the process recipe of negative resistor NR9-1500P using MLA.

Table 3.1 Recipe of NR9-1500P

Parameter	Value
Spinning	Acc 250rpm/s, SS 500rpm, Dwell 5s Acc 1000rpm/s, SS 3000rpm, Dwell 40s
Pre-bake	150 °C, 1min
Exposure	375nm
Dose	750mJ/cm^2
Post-bake	100°C, 1min
Development	RD6 12s, rinse by flowing DI water, N_2 blow dry

Step (c): P contact deposition

The composite for the p-contact we utilize consists of Ti/Pt/Au. It can be deposited by using Electron beam (E-beam) evaporator or Magnetron sputtering.

Step (d): Lift-off

The extra metal contact can be lifted off by immersing it in acetone. In the event of successful photolithography, the excessive metal contact may naturally detach due to the high strain. If this doesn't occur, a gentle ultrasonic bath can facilitate the lift-off process.

Step (e): Lapping

We typically lap the substrate to a thickness of 100-120μm to facilitate cleaving and reduce device resistance. We perform the lapping process using the auto-lapping tool (Ultra Tec).

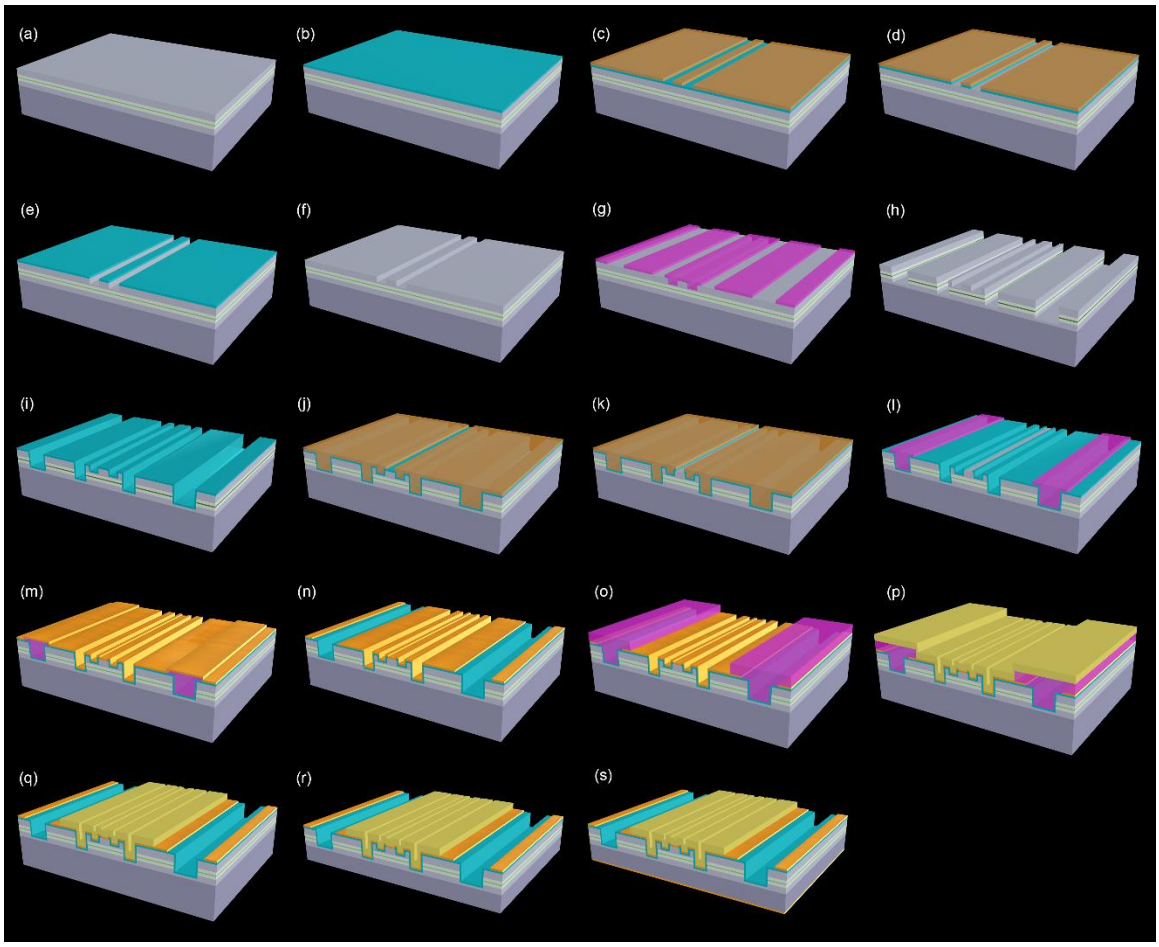

Figure 3.2 Fabrication processing flow of ridge waveguide lasers

Step (f): N contact deposition

The composite for the n-contact we utilize consists of Ni/Ge/Au/Ni/Au. Following this, we usually perform rapid thermal annealing (RTA) at 400°C for 60 seconds, which contributes to lowering the turn-on voltage and the resistance.

3.1.2 Fabrication of ridge waveguide lasers

Broad area lasers typically produce multimode laser output and find their primary use in applications where beam quality requirements are not stringent. Conversely, for applications that demand high beam quality, index-guided ridge waveguide lasers are employed. The ridge waveguide lasers effectively control lateral modes through constructing the ridge waveguide, as demonstrated in Figure 3.2, which details our fabrication process for such lasers.

Step (a): Surface cleaning

This step involves a standard sample cleaning procedure and dehydration bake.

Step (b): SiO_2 deposition

Given that the etchant used for dry etching GaAs-based compound semiconductors typically involves a heated etching chamber at around 180°C, the photoresist is often carbonized at such high temperatures and is unsuitable as a mask layer for dry etching GaAs. Consequently, a 300nm-thick SiO_2 layer is initially deposited as the hard mask layer for subsequent dry etching processes. We employ the PECVD method for SiO_2 deposition.

Step (c): Ebeam lithography (EBL)

EBL is employed to write the ridge laser pattern and alignment markers. We utilize ZEP520a as the EBL resist, and the corresponding recipe is detailed in Table 3.2. To reduce the EBL writing time, a current of 30nA is utilized. For the fabrication of lasers on a wafer scale, photolithography is employed as an alternative to E-beam lithography.

Table 3.2 Recipe of ZEP520a

Parameter	Value
Spinning	Acc 100rpm/s, SS 500rpm, Dwell 5s Acc 800rpm/s, SS 4000rpm, Dwell 60s
Pre-bake	180 °C, 2min
Development	Amyl acetate 2min, soak in IPA 30-60s, N_2 blow dry

Step (d): SiO_2 dry etch

Inductively Coupled Plasma (ICP) dry etching is used to transfer the pattern to SiO_2 layer to form the hard mark. We use an optimized perfluorocyclobutane (C_4F_8) based etch recipe for SiO_2 dry etch, which is shown in Table 3.3. The C_4F_8 gas reacts with the SiO_2 and the Ar_2 provides a physical etching effect. The thermal ICP tool is specifically designed for 4-inch standard silicon wafers. When working with smaller-sized samples, we apply cool grease, an electrically insulating and thermally conductive paste, to affix the samples to the carrier wafer. The cool grease efficiently facilitates heat transfer between the sample and carrier wafer due to its excellent thermal conductivity. After transferring the pattern of EBL resist layer to SiO_2 layer, we can remove EBL resist by soaking in heated (85 ^oC) N-Methyl-2-pyrrolidone (NMP) overnight or at least 20mins.

Table 3.3 Oxide dry etch recipe

Parameter	Value
Pressure	5 mT
RIE power	40 W
ICP power	800 W
Ar	4 sccm
C_4F_8	15 sccm
CO_2	28 sccm

Step (e): GaAs dry etch

We employ the ICP method to perform dry etching of GaAs using an etch recipe based on boron trichloride (BCl_3) and chlorine (Cl_2). Prior to initiating the dry etching process, it is essential to conduct a thorough physical cleaning of the chamber's sidewalls and a pre-cleaning procedure (O_2 plasma for a duration of 60 minutes or longer) to remove contaminants within the chamber. Failure to ensure proper chamber cleanliness may result in peculiar patterns on the top surface of the dry-etched GaAs. Table 3.4 list the etching recipe, in which Ar provides the physical etching effect, and the mixed gas of BCl_3 and Cl_2 chemically reacts with the GaAs material.

Table 3.4 GaAs dry etch recipe

Parameter	Value
Pressure	5 mT
RF1	70 W
RF2	500 W
Ar	5 sccm
BCl_3	8 sccm
Cl_2	32 sccm

He pressure	5 T
He flow	4 sccm

It is worth to mention that the etching rate also depends on the trench width. As shown in Figure 3.3, When the trench width is relatively small, the etch rate significantly increases as the width increases. However, when the trench width exceeds 2μm, the etch rate stabilizes and exhibits minimal change with increasing width.

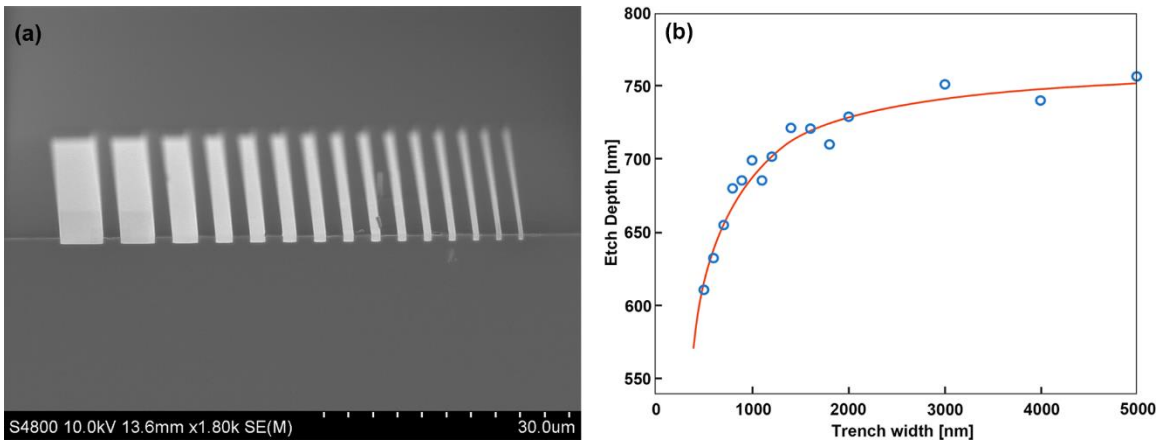

Figure 3.3 (a) Scanning Electron Microscope (SEM) image of etched trenches with varying widths on pure GaAs substrate, (b) measured etch depth (blue circles) as function of the trench width. The red line represents the fitting curve.

Step (f): SiO_2 hard mask removal

Remove the SiO_2 hard mask using the Buffered Oxide Etchant (BOE), a solution composed of hydrofluoric (HF) acid and an ammonium fluoride (NH_4F) buffer.

The subsequent steps (g) and (h) involve the creation of isolation trenches. There are two types of isolation trenches: one positioned near the ridge to inhibit lateral carrier diffusion and improve injection efficiency, while the other is situated along the boundary between

the two emitters. During the segmentation of the laser bar into individual emitter dies, there is a risk of damaging the isolation layer near the cleaving lines, potentially causing leakage current during p-side-down bonding. To avoid this, the isolation trenches are designed to provide recesses along the sidewalls of the dies, thereby preventing the side walls from contacting with solder and the resulting leakage current.

Step (g): Photolithography

Step (h): Isolation trench etch

Since there is no need for precise control of the trench dimensions, wet etch is sufficient for this step. To enhance control over the wet etching rate, a solution consisting of H_3PO_4, H_2O_2, and H_2O in a ratio of 34.6:10:1000 is employed for GaAs wet etching. The etching rate can be tuned by adjusting the proportion of H_3PO_4 within the mixture. To maintain a consistent etching rate for GaAs, the etchant mixture is maintained in a temperature-stable water bath at 20 ^oC.

Please note that when using a photoresist pattern as a protective layer, wet etching is non-directional. As a result, the final trench opening width is approximately equal to twice the etch depth plus the photoresist opening width. Figure 3.4 illustrates a SEM image of the profile of isolation trenches.

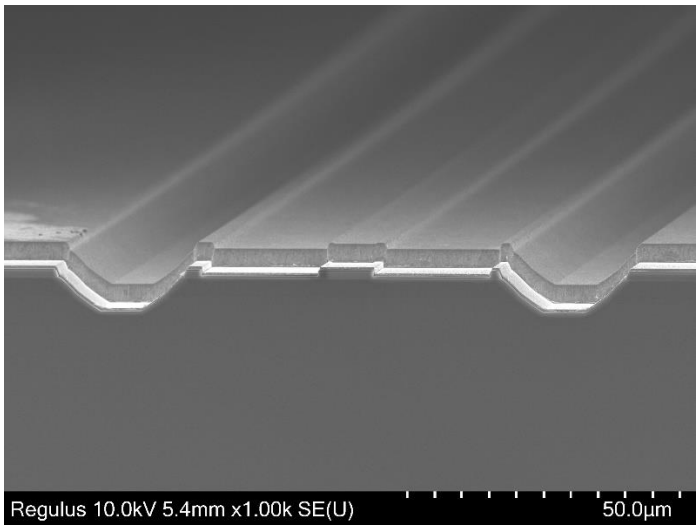

Figure 3.4 SEM image of the cross-section profile of a ridge waveguide laser with isolation trenches

Step (i): SiO_2 deposition

About 250nm-thick of SiO_2 is deposited to serve as the isolation layer of the lasers.

Step (j): E-beam lithography

In contrast to step (c), the EBL writing in this case necessitates an alignment procedure to precisely determine the position of the window opening. Typically, four cross-shaped alignment markers, each with a length of 100μm and a width of 4μm, are employed to achieve a high degree of alignment accuracy (with alignment errors of less than 500nm).

Step (k): SiO_2 window open

This step can be performed by either dry etching or wet etching with BOE. The critical part is to precise control of the etch depth to avoid over-etching the laser epitaxial layers. Figure 3.5 illustrates the occurrence of an over-etching issue. When designing the epitaxial layers, it is advisable to slightly increase the thickness of the p-contact layer to 100-150nm. This adjustment ensures that even in the event of minor over-etching, good

Ohmic contacts can still be prepared without affecting the laser's performance. Additionally, as mentioned in the previous chapter, non-injection regions can be introduced near the laser facet to reduce non-radiative recombination rates of the facet surfaces. When designing the layout, we keep a 5μm distance between the pattern of the SiO_2 window opening and the laser facet, as described by Figure 3.6.

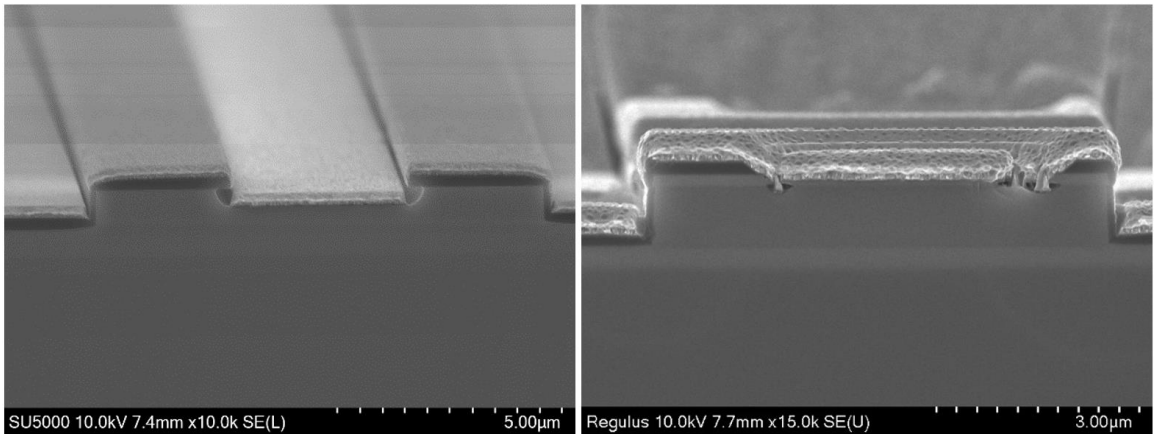

Figure 3.5 SEM images of the cross-section view of ridge waveguide lasers, showcasing instances of over-etching issues that occurred during the SiO_2 window opening process. The window on the left is produced through the dry etching method, while the one on the right is fabricated using the wet etching method.

Steps (l-n) involve the fabrication of the p-contact, following the same procedure as steps (b-d) used in the fabrication of broad-area lasers. Prior to step (I) photolithography, native oxide remove procedure is recommended. It's worth noting that e-beam evaporation exhibits strong directionality, which means that if the sidewalls of the ridge are straight, the metal layer on the sidewalls may become excessively thin, potentially leading to electrical disconnection fractures at the bottom. To avoid this problem, we employ the non-directional sputtering method for p-contact deposition. Sputtering

method helps to deposit sufficient gold coating on the vertical side walls, thereby preventing the issue of electric disconnection. Another approach is to incorporate a thicker metal overlay on the top of the p-contact layer.

Step (l): Photolithography

Step (m): P contact deposition

Step (n): Lift-off

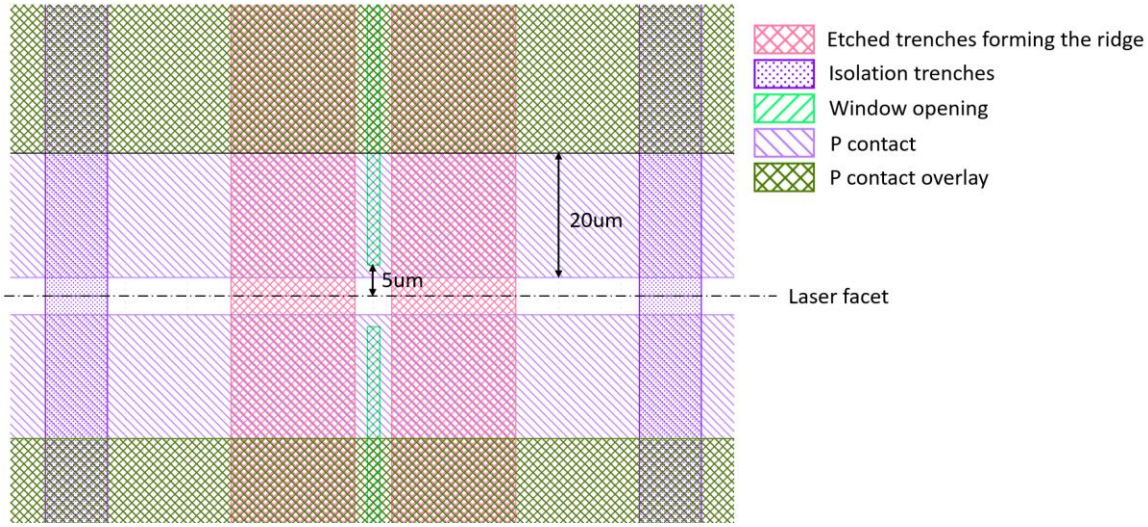

Figure 3.6 Layout of designed ridge waveguide lasers

Steps (l-n) involve the fabrication of the thick p-contact overlay. Our thick overlay consists of a layer of 20nm Ti followed by 3μm Au using an E-beam evaporator. It's important to avoid placing a thick metal overlay near the facet since it can impact the cleaving process at the facet, and there is a risk of the thick metal layer protruding from the end face. As depicted in Figure 3.6, our overlay pattern design consistently maintains a 20um indent from the p-contact pattern. To successfully achieve a 3μm-thick overlay for liftoff, we need to use a thicker photoresist.

Step (o): Photolithography

Step (p): P contact overlay deposition

Step (q): Lift-off

Steps (r) an (s) are the same procedure as steps (e-f) used in the fabrication of broad-area lasers.

Step (r): Lapping

Step (s): N contact deposition and RAT

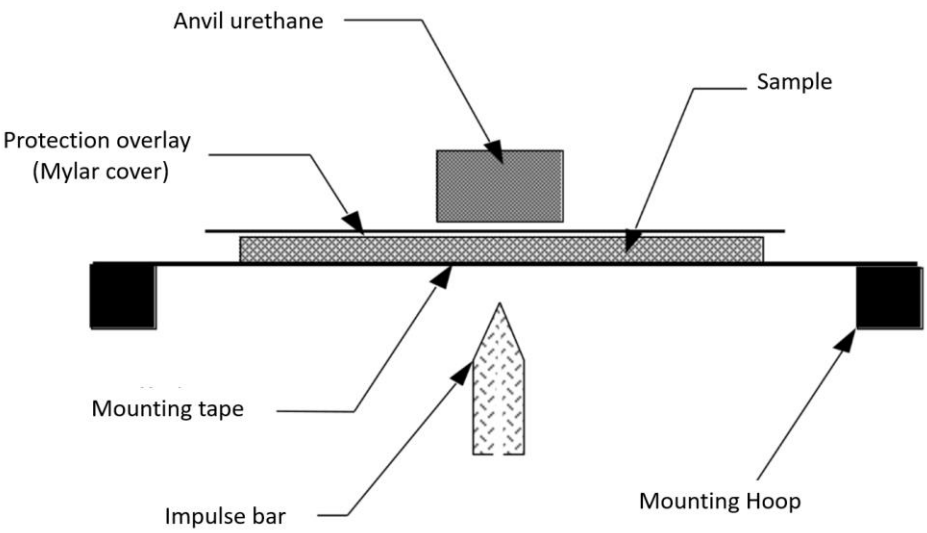

Figure 3.7 Schematic diagram illustrating the impulse/anvil break assembly

The preparation of a BAL or a RW laser is completed following the above process. The final step in forming the laser is to cleave the front and rear facets to create the laser cavity. We use Dynatex DTX 150 scribe and break tool to cleave our laser chips. This tool is designed for high-precision scribing and breaking of crystalline materials. It utilizes a diamond head to perform a scribe near the edge surface of the sample, which

establishes a predetermined fracture line, and then it applies a controlled force to the back side of the sample to break the sample along the scribe line. The angle of diamond head with respect to sample surface significantly influence aggressiveness of cut. For cleaving delicate material such as GaAs and InP, the angle is generally kept being smaller than 35.0 degrees (referred to as “toe” angles). Figure 3.7 shows the schematic of the break assembly. The break type depends on whether there is a flat anvil on top serving as a backstop, distinguishing between impulse break (without the anvil) and anvil break (with the anvil). This means that, in comparison to the impulse break, the anvil break involves an additional compressive force. To protect the sample surface during anvil break, it is required to place a mylar overlay as a protective layer. GaAs, with a zinc-blende crystal structure and the relative weak bonding, provides well-defined cleavage planes, making it easy to cleave a perfect mirror facet. Therefore, we use impulse break type for cleaving laser chip, which does not damage sample surface.

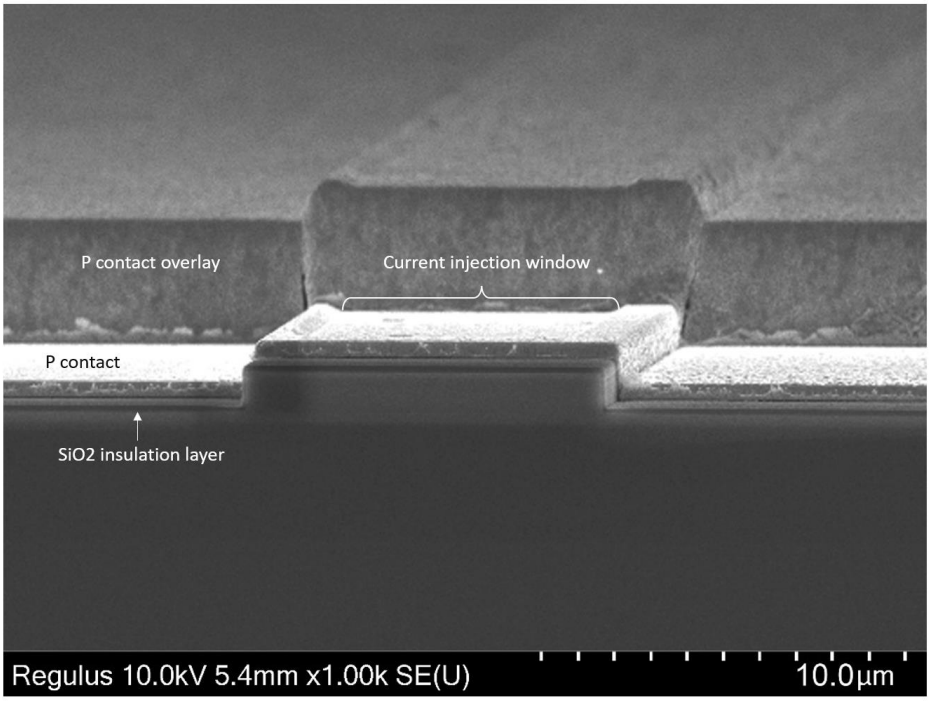

Figure 3.8 SEM image of the cross-section view of a ridge waveguide laser near the ridge waveguide region

We'll first cleave the facets of the laser to create laser bars, conduct an initial test, and subsequently cleave in a direction perpendicular to the facet to separate each laser emitter/laser die. Figure 3.8 shows the SEM image of the cross-section view of a fabricated ridge waveguide laser, featuring excellently cleaved facets precisely located as per the design. A laser without coatings on its front and rear facets will exhibit equal laser output from both sides. To achieve single-sided laser output, anti-reflective (AR) and high-reflective (HR) coatings should be deposited separately on the front and rear facets of the laser.

3.2 Packaging of high-power semiconductor laser

Due to the typically small size of laser die components, which pose challenges in terms of handling and measurement, it is necessary to package the laser die within a larger mounting structure. Except for facilitating ease of handling, the laser packaging also providing essential functionalities including electrical connectivity, heat dissipation and mechanical stability, and thus ensuring the reliable performance of the laser diode. Laser packaging involves a two-step process, which consists of die bonding followed by wire bonding. Die bonding is to bond the laser die to mount/submount through soldering. Wire bonding is to connect the laser die to the external circuitry using very fine wires, typically gold wires.

3.2.1 Die bonding

The most used laser heat sink in our lab is the C-mount, which is primarily composed of copper (Cu) and has an outer coating of Ti/Ni/Pt/Au to prevent oxidation. Cu has a high thermal conductivity of 395 W/mK and Coefficient of Thermal Expansion (CTE) of $CTE_{Cu} = 17.1 \cdot 10^{-6}\ K^{-1}$ [48], which is much higher than that of the diode laser crystal $CTE_{GaAs} = 5.73 \cdot 10^{-6}\ K^{-1}$ [49]. The mismatch in CTE will cause thermomechanical failures of the semiconductor laser when it heats up during the operation. Copper-Tungsten (CuW) submounts are generally employed to avoid this problem, as CuW provide a lower CTE ($CTE_{CuW} = 6.5 \cdot 10^{-6}\ K^{-1}$) and relatively high thermal conductivity of 180 W/mK [50].

Regarding the solder, we use both indium (In) and Gold/Tin (AuSn). Indium is a soft solder with a relatively low melting temperature. It can be used to directly bond laser die on a C-mount due to its softness and malleability. On the other hand, AuSn is a eutectic solder with a higher melting temperature of 280^{o}C. AuSn has a much lower CTE ($CTE_{AuSn} = 16 \cdot 10^{-6}$ K^{-1}) compared to indium ($CTE_{In} = 32 \cdot 10^{-6}$ K^{-1}), allowing it to better absorb mechanical stress [51]. Additionally, since indium is prone to oxidation in the air, commercial CuW submounts typically use AuSn as the solder material.

Die bonding can be implemented as either p-side down or p-side up bonding. P-side down bonding provides better heat dissipation as the heat source (active region) is in closer proximity to the heat sink. However, it places higher requirements for the bonding process and the condition of the laser die. Since the epitaxial structure is very close to the melting solder in p-side down bonding, it is susceptible to laser facet contamination. Furthermore, any damage to the isolation layer near the side wall of the laser die may result in current leakage. As discussed in Section 3.1, we have designed isolation trenches to address this issue. In contact, p side up bonding is more straightforward process and is better suited for hybrid integration applications.

We utilize the Finetech Lambda and Femto2 die bonding tools for our processes. To achieve the best AuSn soldering results, it is critical to ensure proper AuSn reflow. Two key factors must be addressed to attain the desired AuSn reflow. The first key factor is accurate temperature control. The temperature of the AuSn must be sufficiently high to ensure complete melting. Since the C-mount is heated from the bottom, there is a significant temperature difference between the top (the actual temperature of the AuSn)

and the bottom (the set temperature) due to the relatively large height of the C-mount. The second key factor is to isolate the air to prevent the surface oxidation of AuSn during the reflow process. The oxidation of AuSn can cause the formation of a film or crust that hinders proper flow. Prolonged exposure of molten AuSn to air exacerbates the oxidation concern. Consequently, the reflow duration is typically kept around 5s.

3.2.2 Wire bonding

There are two primary techniques for wire bonding: ball bonding and wedge bonding. The key distinction between these methods lies in the type of bond head used. Ball bonding employs capillaries as the bond head, as depicted in Figure 3.9(a), whereas wedge bonding uses a wedge-shaped tip, as depicted in Figure 3.9(b). In the case of ball bonding, a small free-air ball is initially created beneath the capillary through a spark before the actual bonding process. Upon contact with the bond pad's surface, the bonding tool applies force and ultrasonics to deform the ball, facilitating inter-diffusion between the wire and the bond pad metallization and ultimately forming the intermetallic bond.

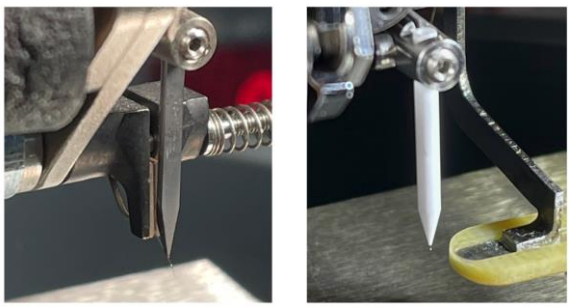

Figure 3.9 Bond head images of (a) ball bonding and (b) wedge bonding

On the other hand, wedge bonding utilizes ultrasonic energy and pressure to flatten the wire beneath the wedge-shaped tip, directly creating a bond between the wire

and the bond pad without the initial ball formation. Ball bonding is generally approximately two to three times faster than wedge bonding. Owing to the absence of the ball on the first bond, wedge bonding allows for applications requiring finer pitch. Our wire bonding tool is equipped with both ball and wedge bonding capabilities. We use gold bonding wire with diameter of 1 mil (25 μm), elongation of 3-5% and tensile strength of 8 g. Considering that our specific application does not necessitate fine pitch wire bonding and taking various factors into account, such as the ease of wire threading and the minimal damage to device surfaces, we prefer to use the ball bonding method more often.

3.3 Characterization method of high-power semiconductor laser

3.3.1 Measurement stage

For unpackaged laser bar and die's test, we use probe station as shown in Figure 3.10 (left). It is equipped with an air-cooling thermal chunk, probe manipulators, and a top-view microscope system. The top-view microscope assists in aligning the probe with the electrodes of the laser emitter under test to establish electrical connections. Unpackaged laser emitters are commonly subjected to Quasi Continuous (QCW) testing, while for packaged emitters, we carry out Continue Wave (CW) testing. Figure 3.10 (right) shows the measurement stage designed for laser emitters on C-mount. The stage is a water-cooling stage connected to a water chiller and use TEC to accurate control the temperature. At times, our lasers lack a coating, emitting equal power from both ends. Therefore, when designing the mounting apparatus for the laser, it is essential to ensure

that the laser's rear facet remains unobstructed by metal (which exhibits high reflectivity in the infrared spectrum). This is necessary to maintain accurate power measurements.

3.3.2 LIV curves

Pulsed current source or is used to drive the semiconductor lasers during QCW measurements and Thorlabs ITC4020DC is used to work as the DC current driver for CW measurements. In cases where a pulsed current source is utilized, it is advisable to keep the lead wire as short as possible to mitigate inductance and enhance load impedance matching. Poor impedance matching can lead to serious distortions and oscillations in current and voltage waveforms.

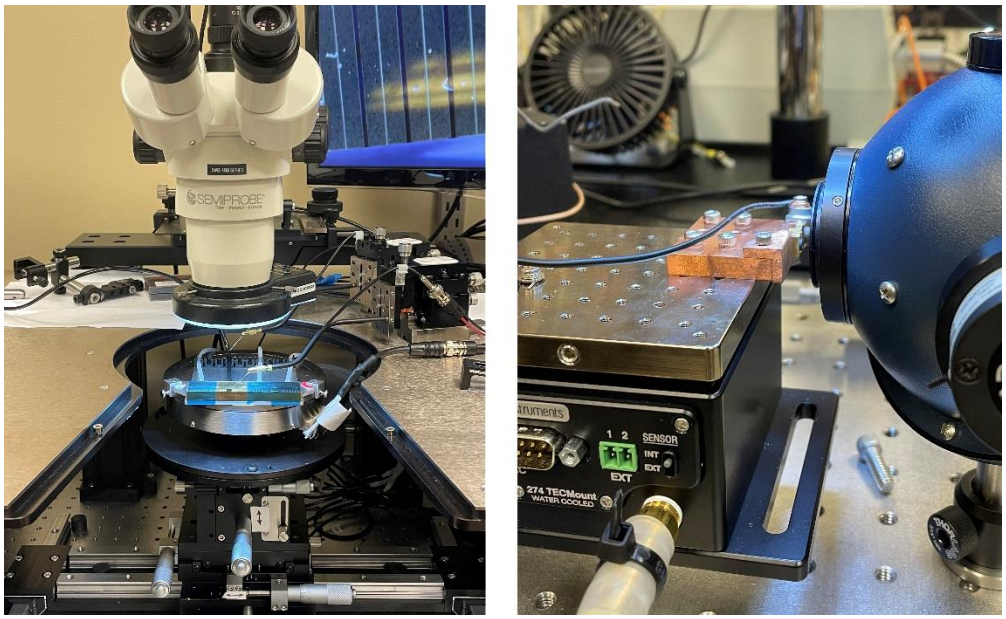

Figure 3.10 Photo of laser test stage: probe stage for unpackaged lasers (left) and lasers packaged on C mount (right)

We use Newport calibrated integrating sphere photodiode sensor, specifically the 819D-SL-5.3-CAL2 model, for power measurement purposes. The sensor is connected to the power meter 843-R-USB (handheld) or 2936-R (benchtop) for obtaining power readings. Note that for QCW power measurement, this power sensor offers the average power across multiple pulses. Consequently, to determine peak power, we should divide the measured average power by the duty cycle.

We employ the four-probe method for IV curve measurements to eliminate the influence of lead wires' resistance. For IV curve measurements of unpackaged laser emitters, we use the Keithley 4200A-SCS semiconductor parameter analyzer. Since the parameter analyzer utilizes DC current for measurements, we typically set the current compliance to 100 mA to protect unpackaged lasers from potential damage. For CW

measurements of packaged lasers, the LI and IV measurements are conducted simultaneously. We use the voltage functionality provided by the ITC4020DC to read the laser's voltage values.

3.3.3 Far field

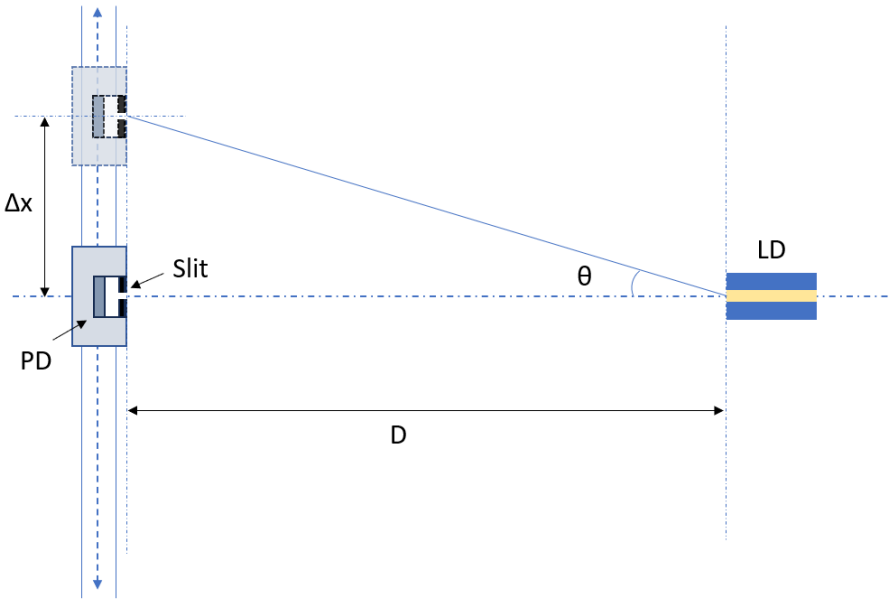

Figure 3.11 Schematic of the far field measurement setup on a motorized linear stage

The laser diode produces an orthogonal astigmatic beam due to its asymmetric light emission beam width in the lateral and vertical directions. As a result, it exhibits distinct divergence angles in these two planes, and the evolution of the beam in these two planes can be independently described. The lateral direction is typically referred to as the "slow axis," while the vertical direction is referred to as the "fast axis," as shown in Figure 2.1. The mode profile in the vertical/fast-axis direction of the laser diode is determined by the epitaxial structure and is typically single-mode and diffraction limited.

Therefore, in this study, we primarily focus on far-field measurement in the lateral/slow-axis direction.

We utilize two setups for conducting far field measurements. One of these setups involves the use of an infrared (IR) camera, which is positioned in front of the semiconductor laser. The output obtained from the IR camera represents the far field image and can be transformed into angular distribution based on the separation between the laser diode and the camera. However, it's worth noting that the IR camera does not exhibit a linear response to light intensity. For example, when the exposure time is set too high, light saturation may occur at certain locations, resulting in less precise far field results obtained from this method.

Our alternative setup for far field measurement is illustrated in Figure 3.11. A photodetector (PD) with a rectangular slit is placed on a motorized linear stage. In this setup, we place a photodetector (PD) with a rectangular slit on a motorized linear stage. The laser diode emitter is positioned at the center of the stage, ensuring that the laser emission direction is perpendicular to the stage. By moving PD along the linear stage, we are able to scan the far-field profile. Assuming a distance of D between the laser diode's front face and the slit, we can calculate the rotation angle using the formula:

$$\theta = \arctan\left(\frac{\Delta x}{D}\right) \tag{3.1}$$

The step size for moving PD should be equal to or greater than the width of the slit. Furthermore, we should wait for the photodetector's position to stabilize after each movement (setting time) before taking power readings.

We typically use the slit width of 50μm or 100μm to enhance the accuracy of angle, we can either reduce the slit width and the step size, or increasing the value of D. Moreover, it's worth mentioning that our current setup is most effective when dealing with divergence angles that are not too large. This is because, as Δx increases, the fixed width of the slit corresponds to a smaller angle, and with an increasing incident angle, the photodetector's response to power decreases. These factors can lead to reduced power readings and, consequently, a measured divergence angle smaller than the actual value. In this context, it is advisable to position the sensor panel as close to the slit as possible. Furthermore, the photodetector (PD) should be placed on a rotating stage. This allows for the simultaneous movement of the PD to a specific position Δx and its rotation to an angle θ (as shown in Figure 3.12), which ensures that the PD's front face remains perpendicular to the incident direction, thereby maximizing power readings. For even greater precision, it is recommended to replace the linear rail with a circular rail. The use of a circular rail is essential when measuring far fields with significant divergence, such as the fast axis farfield measurement. It's important to note that if a circular rail is employed, the laser diode's front face must be positioned at the center of the circle.

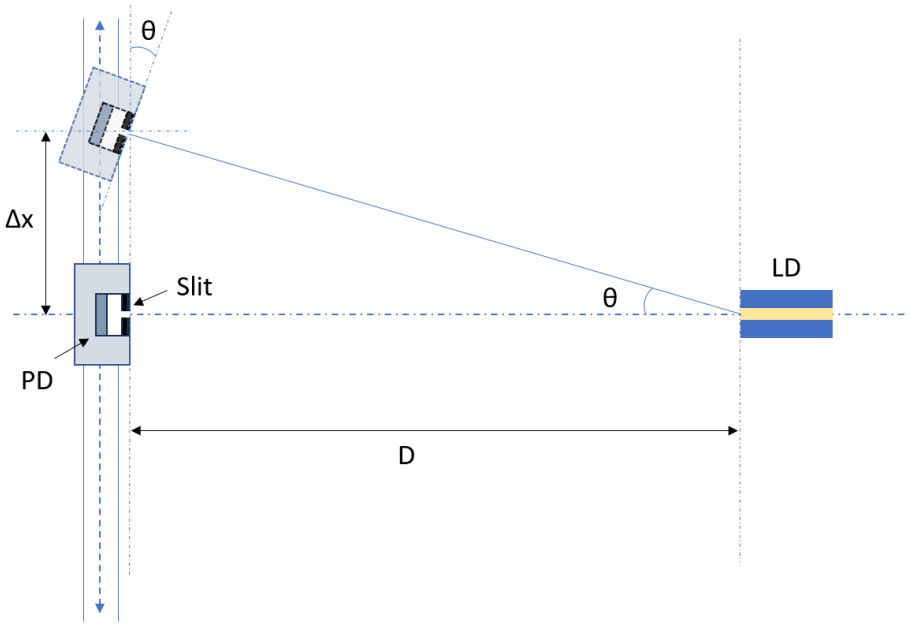

Figure 3.12 Schematic of the far field measurement setup with a motorized linear stage and a rotation stage

3.3.4 Near field

We capture the image of the laser output facet for near-field measurements. This is achieved by setting up an optical imaging system, depicted in Figure 3.13. The laser facet is imaged using a near-infrared (NIR) infinity-corrected objective lens and a tube lens, with the resulting image being recorded by an infrared (IR) camera. The magnification of the imaging system is determined by the ratio of the focal lengths of the tube lens and the objective lens, which is calibrated using a slit with known width. One benefit of this imaging system configuration is that it allows for the insertion of optical filters between the objective lens and tube lens without affecting the image quality. We

use Neutral Density (ND) filters to reduce the light intensity when performing near-field measurements of high-power laser beams.

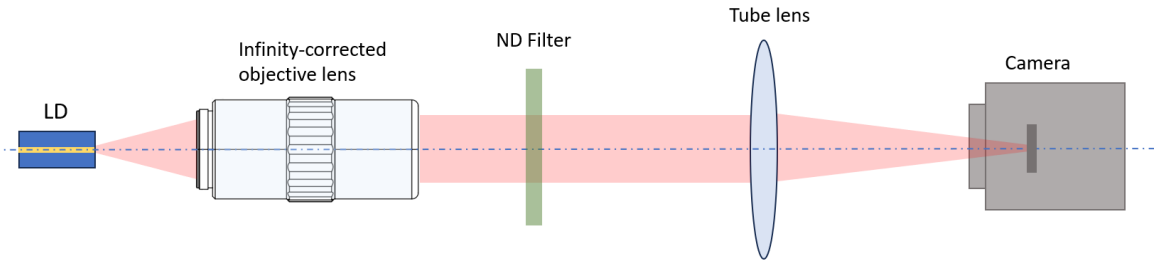

Figure 3.13 Optical path setup for the measurement of near field profiles

3.3.5 Spectrum

To analyze the optical spectrum, we employ an Optical Spectrum Analyzer (OSA) or . There are two approaches to collect the output beam into an optical fiber. One approach involves utilizing the optical fiber output interface of the integrated sphere and collecting the laser output using an optical multimode fiber. This method incurs a considerable level of loss, and the magnitude of this loss can be estimated by dividing the fiber core size by the integrated sphere's inner surface area. Therefore, larger fiber cores result in reduced losses. In our case, we use a multimode optical fiber with a 600μm core diameter. This method is chosen for the measurement of the optical spectrum of the laser output under CW mode.

For optical spectrum analyzing under the QCW mode, we use the second approach. The output light is first collimated by a NIR objective lens and then collected and focused onto a multimode optical fiber by fiber collimator, as shown in Figure 3.14

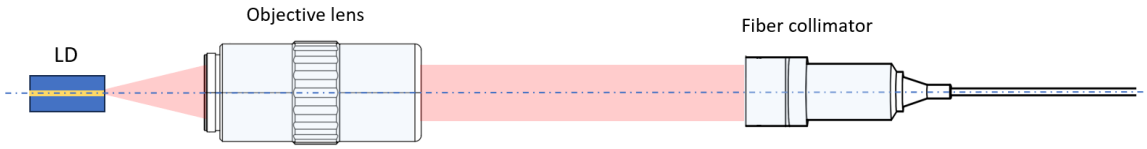

Figure 3.14 Experimental setup for optical spectrum measurement

Chapter 4

HIGH-POWER HIGH-EFFICIENCY SINGLE-MODE RIDGE DIODE LASERS

High-power, high-efficiency diode lasers operating in the fundamental transverse mode are essential components greatly sought after in various applications. They play a crucial role in achieving diffraction-limited focusing and are in high demand across a wide spectrum of fields, including optical communications, laser sources for pumping , laser surgery, and direct-diode material processing [52-56]. Among the various techniques available, the ridge waveguide (RW) diode laser is a fundamental and effective means to achieve single-mode laser output. In this chapter, we will leverage the developed ETAS epitaxial structure from Chapter 2 to demonstrate high-power high-efficiency single-mode ridge waveguide lasers.

4.1 Ridge waveguide laser structure design and simulation

Based on the different lateral guiding mechanisms in edge-emitting laser diodes, they can be categorized into two types: gain-guided and refractive index-guided lasers

[57]. In the passive state, gain-guided lasers do not impose specific constraints on carriers and photons in the lateral direction. However, in the presence of current injection, they rely on varying gain profiles in different regions to constrain the optical field. Gain-guided lasers tends to exhibit poor output beam quality. Index-guided lasers process fabricated waveguide structures, offering rigid refractive index differences in the lateral direction. This effectively confines carriers and photons to the lasing region, improving linear optical power output characteristics and achieving stable mode properties. However, they are less conducive to fundamental mode operation and may result in higher-order mode lasing. In practical operation, RW edge-emitting lasers often involve a competitive interplay between gain-guided and refractive index-guided mechanisms, leading to laser mode instability. Therefore, achieving and maintaining fundamental transverse mode operation at high power levels require careful optimization of the waveguide structure's refractive index differences to attain favorable mode control conditions.

We initially consider the passive waveguide case, where the mode analysis is solely determined by the ridge waveguide geometry and epitaxial structure, and the other effects inducing refractive index changes, such as carrier injection, local thermal heating, and mechanical stress, are ignored. The epitaxial wafer we use for RW laser design is the ETAS structure covered in Chapter 2. The final designed ETAS wafer incorporates an InGaAs single quantum well along with AlGaAs barriers, resulting in a measured peak photoluminescence wavelength of 968nm. Its confinement factor is designed to be 0.6%,

and its refractive index and fundamental mode intensity profiles in the vertical direction are plotted in Figure 4.1.

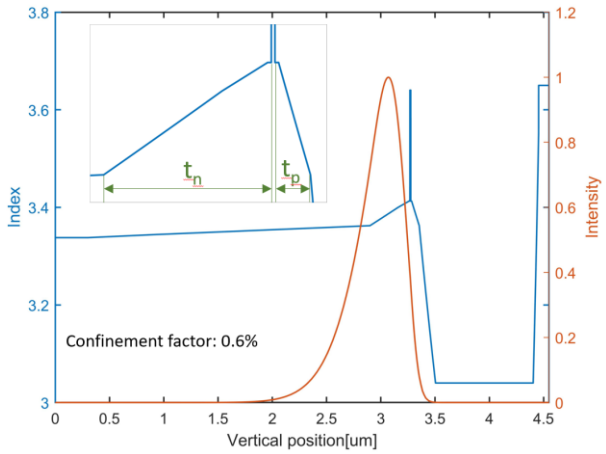

Figure 4.1 Refractive index and fundamental vertical mode intensity profiles of the ETAS epitaxial structure used for RW laser fabrication

We conduct two-dimensional mode analyses of the ridge waveguide using the Finite-difference Eigenmode (FDE) solver of Ansys Lumerical. The structural parameters dominating the fundamental mode stability are the ridge width and the ridge height/etch depth. Figure 4.2 shows the fundamental mode stability plot of ETAS-based RW laser with considerations based on the ridge width and etch depth. The blue and red curves in the graph represent, respectively, the etch depths corresponding to the cutoff of the fundamental mode and the first-order mode. In this context, the shallow region indicates the exclusive area where the fundamental mode exists within the passive waveguide configuration of the RW laser. When RW laser operating at low injection levels, the carrier concentration in the ridge region typically exceeds that of the surrounding areas. This non-uniform distribution of carriers can lead to a carrier-induced anti-guiding effect, potentially resulting in mode changes and instability. Consequently, it's important to

ensure that the effective refractive index difference of the waveguide is not too small, and the etch depth is adequately deep. To enhance output power, we fabricated a broader waveguide with ridge width of 7μm and 9μm, and taking into account a etch depth deviation of about ±50 nm across the wafer, we ultimately settled on a targeted etch depth of 1050nm.

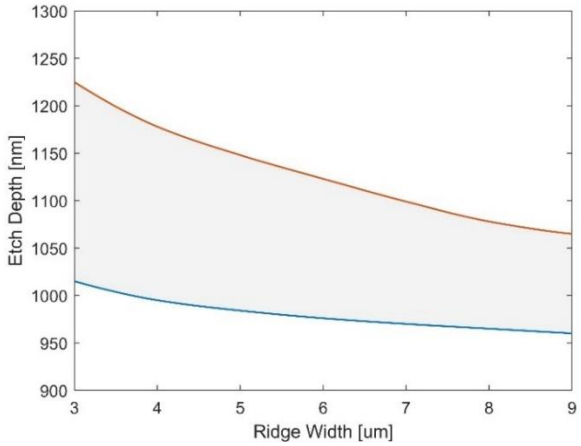

Figure 4.2 The fundamental mode stability plot of ETAS-based RW laser based on the ridge width and the etch depth.

4.2 Experimental results of ETAS-based RW laser

4.2.1 9μm-wide RW lasers with AR and HR coatings

In this section, the 8μm-width RW lasers under examination feature 2% AR and 95% HR coatings on their front and rear facets, respectively, applied by K Lab Corporation. The measured voltage, light power and conversion versus current are plotted in Figure 4.3(a)-(c). As expected, the laser with the shorter cavity length exhibits higher resistance and, consequently, higher voltage compared to the one with the longer cavity length. Table 4.1 provides the extracted threshold currents and slope efficiencies values

for these lasers. With an increase in cavity length from 3mm to 5mm, there is a slight rise in the threshold current and a modest decrease in slope efficiency, indicating a low internal loss level in the epitaxial wafer. In terms of conversion efficiency, the 4mm laser performs the best, with a maximum efficiency of 59% at 0.7A and 55% at 1.5A.

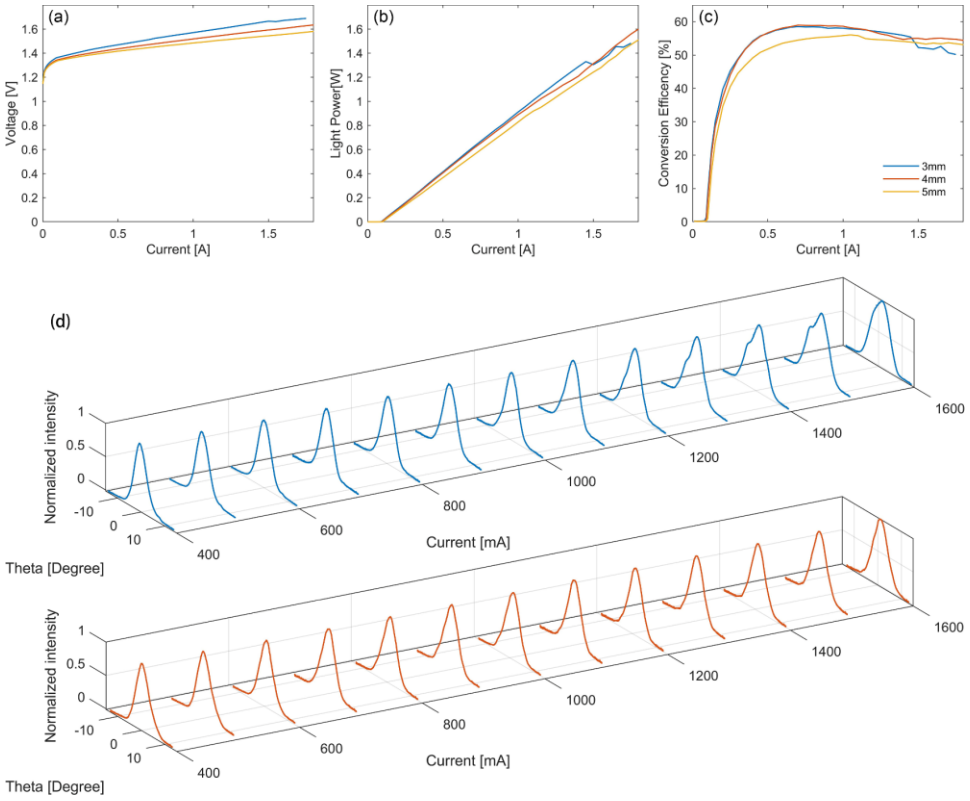

Figure 4.3 Measured voltage (a), optical power (b), and conversion efficiency versus (c) of injection current for ETAS-based 9μm-width ridge lasers, and (d) far field evolution versus injection current for the laser with cavity length of 4mm (up, blue) and 5mm (bottom, red). The lasers have front and rear reflectivity of R_{front} = 2% and R_{rear} = 95%. The experimental conditions include p-side up mount on C-mount, CW mode operation and passive cooling stage set at 18°C.

Figure 4.3(d) depicts the measured far field evolution of the 4mm (in blue) and 5mm (in red) lasers as the injection current increases. The far-field divergence angle

gradually increases with the growing current. Beyond 1.2 A, the far field of the 4mm laser deviates from its nearly Gaussian shape. The far-field expansion of the 5mm laser is more favorable compared to the 4mm laser, maintaining a nearly Gaussian shape until 1.5A. This is attributed to the smaller internal resistance and relatively weaker thermal effects in the 5mm laser. Additionally, the longer cavity length contributes to raising the threshold current for higher-order modes, thereby aiding in suppressing the lasing of the higher-order modes.

Table 4.1 Extracted threshold currents and slope efficiencies of ETAS-based 9μm-width ridge lasers with AR and HR coatings.

Cavity length[mm]	**Threshold [mA]**	**Slope efficiency [W/A]**
3	87	0.976
4	89	0.924
5	97	0.876

4.2.2 7μm-wide RW lasers with AR and HR coatings

Figure 4.4 presents the measured results of the 7μm wide RW ETAS-based lasers with AR and HR coatings. This batch of lasers are packaged using our optimized AuSn solder reflow process, which helps to reduce the resistance introduced during the laser packaging procedure, consequently leading to reduced voltage and improved overall performance. The extracted threshold current and slope of the 4mm laser is 80mA and 1W/A, respectively. It achieves the maximum efficiency as high as 62% at the current of 1.06A and the output power of 1W, and 60.2% at 1.6A and 1.52 W. Figure 4.4 (d) depicts the evolution of the measured far-field pattern with increasing injection current. Both the

4mm and 5mm lasers maintain near-Gaussian far-field profiles up to high injection currents of 1.7A.

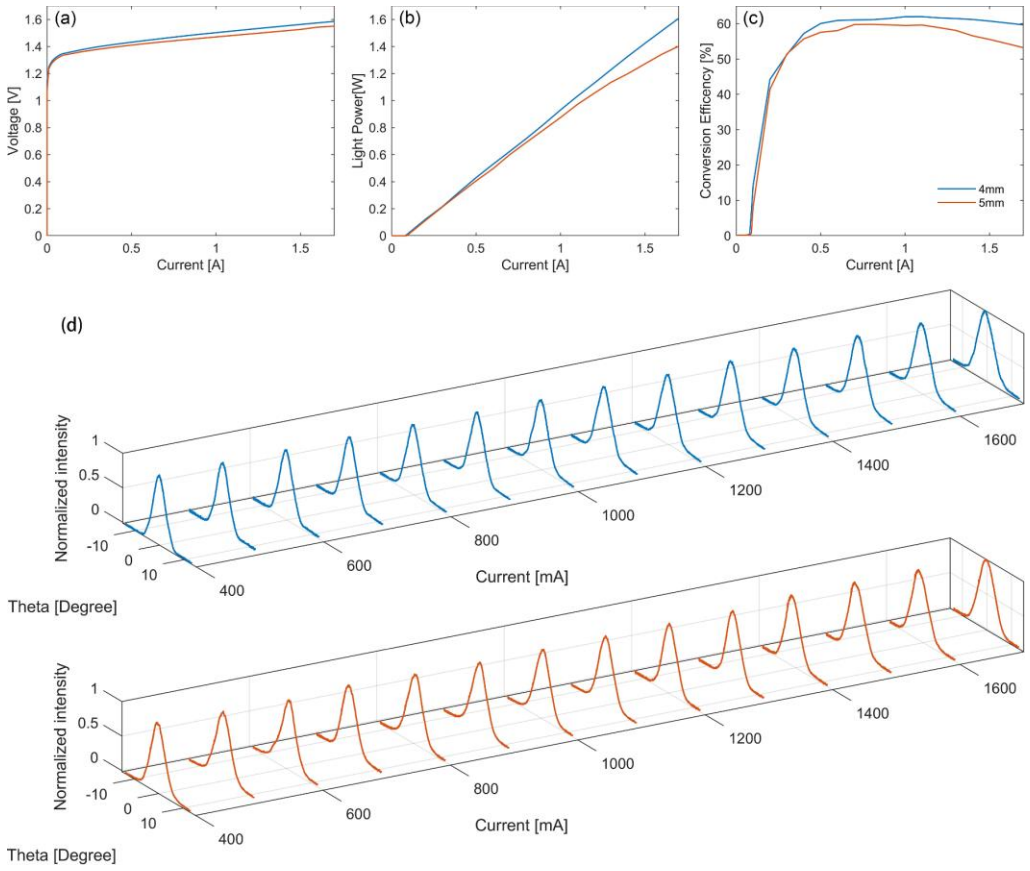

Figure 4.4 Measured voltage (a), optical power (b), and conversion efficiency versus (c) of injection current for ETAS-based 7μm-width ridge lasers, and (d) far field evolution versus injection current for the laser with cavity length of 4mm (up, blue) and 5mm (bottom, red). The lasers have front and rear reflectivity of R_{front} = 2% and R_{rear} = 95%. The experimental conditions include p-side up mount on C-mount, CW mode operation and passive cooling stage set at 18°C.

4.2.3 7μm-wide RW lasers without AR and HR coatings

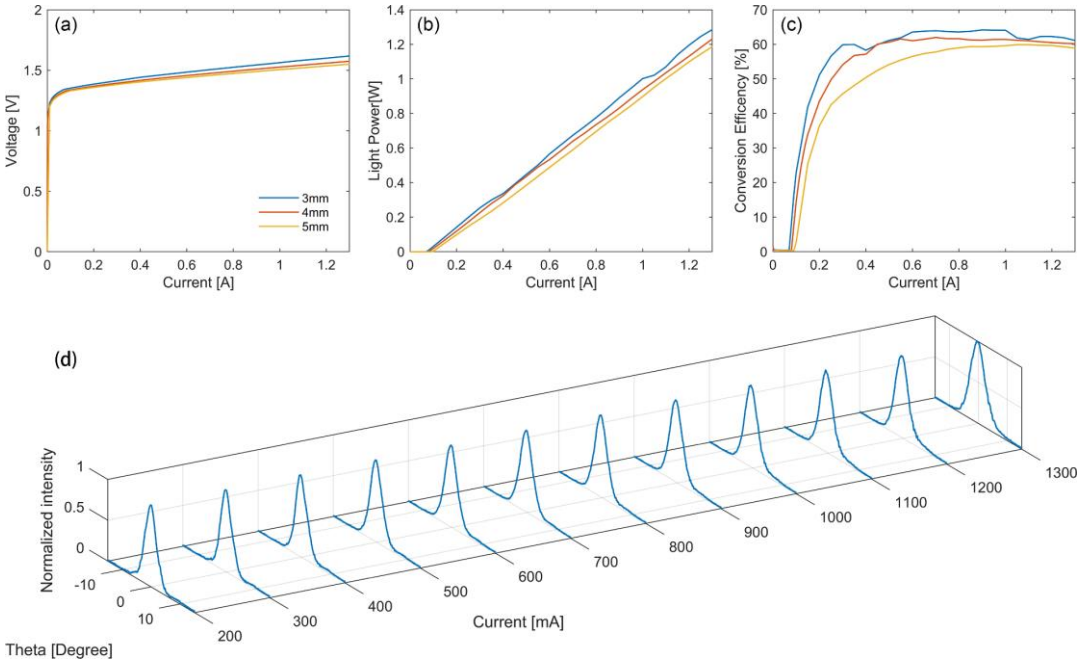

Figure 4.5 Measured voltage (a), optical power (b), and conversion efficiency versus (c) of injection current for ETAS-based 7μm-width ridge lasers without AR and HR coatings, and (d) far field evolution versus injection current for the laser with cavity length of 5mm. The experimental conditions include p-side up mount on C-mount, CW mode operation and passive cooling stage set at 18°C.

We further test the 7μm-wide RW lasers without AR and HR coatings. The measured voltage, power and conversion efficiency results are plotted in Figure 4.5. Table 4.2 lists their extracted threshold and slope efficiencies. The 3mm laser has the lowest threshold current of 71mA and highest slope efficiency of 1.068W/A. But we can observe two kinks at around 0.5A and 1.05A, indicating mode switch and resulting in obvious conversion efficiency drops. For the 5mm laser, there is no kinks and more smooth conversion efficiency curve as function of injection current. The 3mm, 4mm and 5mm lasers delivers 1W laser output with the conversion efficiency of 64%, 61.2% and 59.9% respectively. The measured farfield evolution of 5mm laser is plotted in Figure

4.5(d), showing near-Gaussian far-field profiles up to high injection currents of 1.3A.

Table 4.2 Extracted threshold currents and slope efficiencies of ETAS-based 7μm-width ridge lasers without AR and HR coatings.

Cavity length[mm]	Threshold [mA]	Slope efficiency [W/A]
3	71	1.068
4	80	1.017
5	96	1.012

4.3 Experimental results of 5μm-wide RW laser based on improved asymmetric waveguide epitaxial wafer

The ETAS epitaxial structure relies on a high aluminum composition in the p cladding layer to form a substantial index change. However, reducing the aluminum composition can enhance the carrier mobility, thereby improving the laser's electrical and thermal performance. As such, we optimize the ETAS epitaxial structure by decreasing the aluminum composition in the p cladding layer from 85% to 38%. Figure 4.6 shows the refractive index and mode profile of the new epitaxial structure. Subsequently, 5μm-wide 5mm-long RW lasers, utilizing this epitaxial structure, are fabricated. The lasers are uncoated and packaged on Cmount with pside up. The corresponding measurements of voltage, light power, and conversion versus current are presented in Figure 4.7 (a)-(c). The extracted threshold and slope are 80mA and 0.97W/A, respectively. Its maximum conversion efficiency is 61.1% at 0.7A, and the efficiency for an output power of 1W is 59.3%.

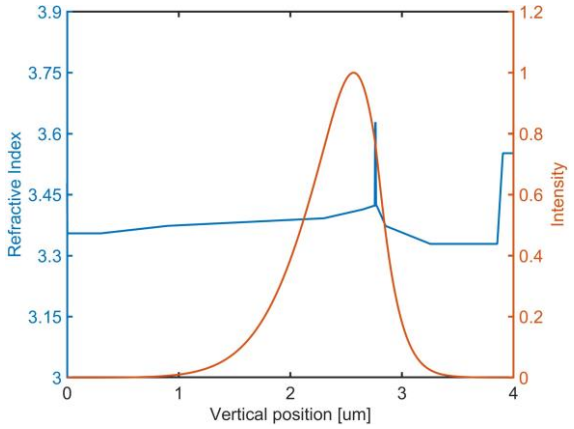

Figure 4.6 Refractive index and fundamental vertical mode intensity profiles of the improved asymmetric epitaxial structure

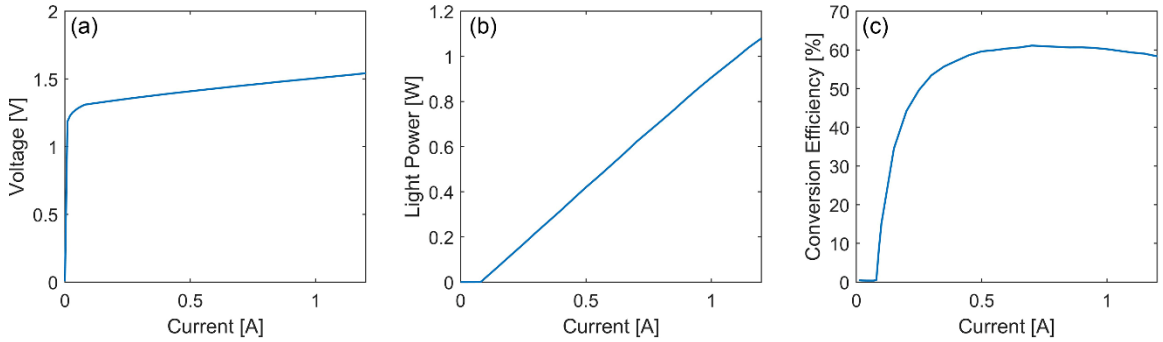

Figure 4.7 Measured voltage (a), optical power (b), and conversion efficiency versus (c) of injection current for 5μm-width ridge lasers based on the improved asymmetric epitaxial structure. The experimental conditions include p-side up mount on C-mount, CW mode operation and passive cooling stage set at 18°C.

To further quantify the changes in the quality of the output beam as the current increases, the diffraction parameter M^2 is extracted. The value of M^2 can be determined from the near-field beam width/waist w ($1/e^2$) and the far-field full divergence angle Θ ($1/e^2$) using the following relationship:

$$\Theta = M^2 \frac{4\lambda}{\pi w} \tag{4.1}$$

Here, Θ is the full divergence angle. M^2 is also referred to as the Times-Diffraction-Limit-Factor. For a purely Gaussian beam, the M^2 value is 1. A beam of higher order or a beam with mixed modes exhibits a larger beam waist and faster divergence, resulting in a higher M^2 value.

Figure 4.8 shows the measured beam width, divergence angle, and M^2 values as a function of the injection current. We can see that M^2 value keeps basically close to 1, indicating the stable near-diffraction-limit single mode emission.

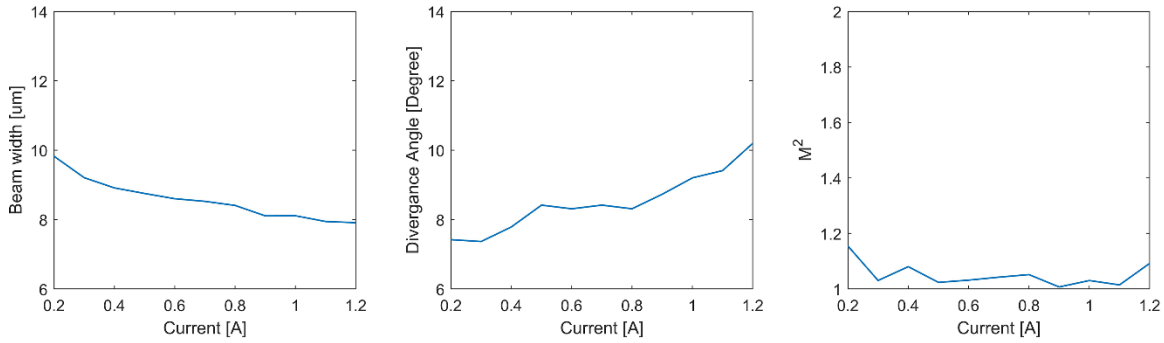

Figure 4.8 The measured beam width, divergence angle, and M^2 values versus injection current for 5μm-wide 5mm-long RW lasers under CW operation mode.

4.4 Conclusion

In this chapter, we demonstrate high-power high-efficiency RW lasers based on ETAS epitaxial structure. The 7μm-wide 4mm-long RW lasers with AR and HR coatings achieve kink-free output and near-Gaussian far-field profile with maximum power higher than 1.6W. Its extracted threshold current and slope of is 80mA and 1W/A, respectively. At a current of 1.06A and an output power of 1W, it achieves peak efficiency as high as 62%. Its efficiency shows minimal decline as current increases, maintaining a high efficiency of 60.2% at 1.6A and 1.52W. 7μm-wide RW lasers without AR and HR

coatings demonstrate comparable performance to those equipped with coatings. However, uncoated lasers, lacking facet passivation, exhibit a lower maximum achievable power compared to coated lasers.

Additionally, we fabricate narrower RW laser based on an improved epitaxial structure featuring reduced aluminum content in the p-cladding layer. 5μm-wide 5mm-long RW laser exhibits kink-free output up to 1W with a high efficiency of 59.3%. Its measured M^2 value remains consistently close to 1, suggesting near-diffraction-limit single-mode emission.

Chapter 5

HIGH POWER SINGLE MODE TRIPLE-RIDGE WAVEGUIDE SEMICONDUCTOR LASER BASED ON SUPERSYMMETRY

Chapter 4 delves into the exploration of high-power single transverse mode lasing within the framework of a single ridge waveguide (RW) laser design, which incorporates an index-guided RW structure to ensure single spatial mode operation. As previously discussed, within the design of a single RW laser, there exists a contradiction between the mode control mechanism and high-power output. A broader ridge design with weak effective index contrast is necessary to scale up the maximum single-mode output power. However, this weak index contrast makes the waveguide structure susceptible to effects such as carrier-induced index suppression, thermal lensing, and spatial hole burning. It tends to support multiple transverse modes at high drive currents, resulting in mode instabilities manifesting as kinks in the light-output (IL) curves, beam steering and beam-quality degradation [10]. Hence, it is desirable to introduce additional mechanisms within single RW laser design to prevent the onset of higher-order modes while simultaneously

achieving high power. Various approaches have been investigated to implement mode filtering in the transverse direction such as angled gratings lasers [58, 59] and anti-resonant reflective optical waveguide (ARROW) lasers [60]. Photonics crystal resonators are proposed in surface-emitting-type semiconductor lasers for the realization of single-mode operation with larger emission area [61-63]. In recent years, by harnessing notions from the selective breaking of parity-time (PT) symmetry, a novel PT symmetric design approach is established to achieve single mode lasing in transversely multi-mode microring lasers [63-65]. To further scale up the output power, super symmetric coupled laser arrays based on the principle of unbroken supersymmetry (SUSY) are proposed, showing great promise in generating high-power diffraction-limited lasing output in strip waveguide arrays [66, 67], micro ring resonator arrays [68], and most recently proposed higher-dimensional microlaser arrays [69]. In light of the SUSY principle, we propose a high-power single transverse mode laser by constructing a triple-ridge waveguide (TRW) structure.

5.1 Operation principle of TRW lasers

In classical quantum mechanics, the Hamiltonian describing a quantum mechanical system must possess Hermiticity in mathematics. This property ensures that its eigenvalues are real but also guarantees that the modulus of the wave function remains constant during its time evolution, which upholds the reality of observable quantities and the conservation of system probabilities. This means that the system is isolated and does not exchange energy with the external world [70]. However, in 1998, Bender and Boettcher pointed out that Hermiticity is not a necessary condition for real eigenvalues

[71]. For non-Hermitian Hamiltonians that satisfy parity-time symmetry (PT symmetry), all of their eigenvalues are real before the symmetry is broken, but they become complex after the symmetry is broken. The so-called PT symmetry means that the Hamiltonian remains unchanged in form after undergoing a Parity (P) and time-reversal (T) operation.

Consider generally a Hamiltonian $\hat{H} = \hat{p}^2/2m + V(\hat{x})$, where $\hat{x}$ and $\hat{p}$ are position and momentum operators respectively, m represents the mass and V is the potential. In the case of an isolated Hermiticity system, the potential function, $V(\hat{x})$, is a real-valued function. However, when dealing with the non-Hermitian systems, the potential $V(\hat{x})$ becomes a complex function. To establish PT symmetry in the Hamiltonian operator, it is derived as a necessary (but not sufficient) condition that the potential function should fulfill $V(\hat{x}) = V^*(-\hat{x})$, owing to the fact that the kinetic energy term in $\hat{H}$ is invariant under both parity and time-reversal.

In optics, based on the mathematical analogy between the Schrödinger equation in quantum mechanics and the paraxial equation of electromagnetic wave propagation under the slowly varying envelope approximation, the non-Hermiticity PT-symmetry photonic systems can be established by judiciously engineering the index guiding and gain/loss distributions. In this context, the refractive index distribution plays the role of the potential. The optical guided mode profiles and the corresponding propagation constants are respectively analogous to the eigenfunction and eigenvalues. Therefore, given that the complex refractive-index distribution $n(x) = \Re\{n(x)\} + i\Im\{n(x)\}$ serves as an optical

potential, we can design a PT-symmetric photonics system by meeting the conditions: $\Re\{n(x)\} = \Re\{n(-x)\}$ and $\Im\{n(x)\} = -\Im\{n(-x)\}$ [72-74].

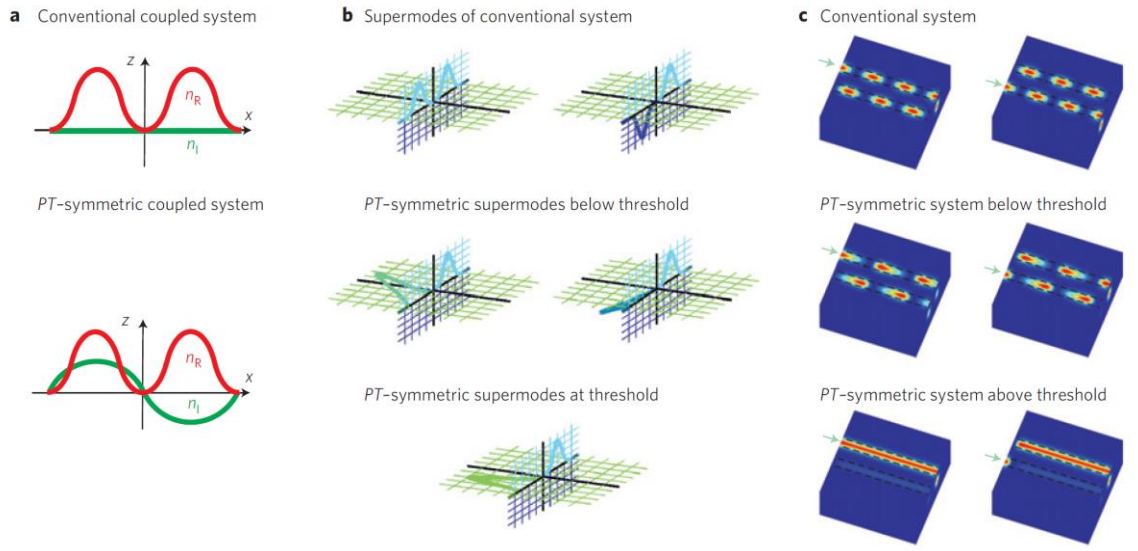

Figure 5.1 Conventional and PT-symmetric coupled optical systems: (a) Real (n_R, red line) and imaginary (n_I, green line) parts of the complex refractive-index distribution; (b)Supermodes of a conventional system and of a PT-symmetric system; (c) Optical wave propagation when the system is excited in Channel 1 or 2. In the conventional case, wave propagation is reciprocal while in a PT-symmetric system, optical waves exhibit non-reciprocal propagation characteristics both below and above the threshold [75].

In 2010, Rüter et al. [75] investigated a symmetric coupled waveguide system in integrated optics. As shown in Figure 5.1, the system comprises two coupled waveguides Channel 1 and Channel 2 with coupling coefficient κ. One of the waveguides is pumped to have a net gain coefficient of γ and the other waveguide has an equal amount of loss -γ, thereby constructing a complex refractive index distribution that satisfied PT symmetry. Through the coupled-mode method, the optical field dynamics in two coupled

waveguides can be described by the following equations:

$$\begin{aligned} i\frac{dE_1}{dz} - i\frac{\gamma}{2}E_1 + \kappa E_2 = 0 \\ i\frac{dE_2}{dz} + i\frac{\gamma}{2}E_2 + \kappa E_1 = 0 \end{aligned} \tag{5.1}$$

where E_1 and E_2 represent the amplitude of the mode fields in Channel 1 and 2, respectively. The system can be described by the following Hamiltonian:

$$H = \begin{pmatrix} i\frac{\gamma}{2} & -\kappa \\ -\kappa & -i\frac{\gamma}{2} \end{pmatrix} \tag{5.2}$$

By determining the eigenvectors and eigenmodes of the coupled waveguides, we can observe distinct system behaviors below and above a threshold, known as phase-transition point $\gamma/(2\kappa)=1$. It is worth noting that, unlike Hermitian systems, the eigenmodes of this non-Hermitian system are no longer orthogonal, which suggests optical-beam dynamics with non-reciprocal responses and power oscillations. For a conventional Hermitian system (γ=0), any superposition of the two eigenmodes/supermodes (symmetric and antisymmetric, as shown in Figure. 5.1b (top)) results in reciprocal wave propagation: the optical wave distribution exhibits left-right symmetry as depicted in Figure. 5.1c (top).

For the PT-symmetry non-Hermitian cases with gain/loss contrast γ, when $\gamma < 2\kappa$ (below the threshold), the system is in a PT-symmetric phase and the eigenvalues of the system are real numbers $\lambda_{1,2} = \pm\cos\theta$, where $\sin\theta = \gamma/(2\kappa)$. The corresponding eigenmodes are given by $|1,2\rangle = (1, \pm\exp(\pm i\theta))$. The modes undergo a balanced gain and

loss, leading to zero imaginary parts of their eigenvalues. As illustrated by Figure 5.1c (middle), the optical wave propagation is now non-reciprocal. At the threshold of $\gamma = 2\kappa$, the eigenvalues of the system are $\lambda_{1,2} = 0$ with eigenmodes $|1,2\rangle = (1, i)$. The field amplitudes in the two channels have the same magnitude, and their relative phase difference is $\pi/2$, as illustrated in Figure 5.1b (bottom). In the regime $\gamma > 2\kappa$ (above the threshold), the system is in the PT-broken phase, and the eigenvalues of the system are complex numbers $\lambda_{1,2} = \mp i \sinh\theta$ with $\cosh\theta = \gamma/(2\kappa)$. The corresponding eigenmodes are $|1,2\rangle = (1, i\exp(\mp\theta))$. Clearly, $|E_1|$ is now not equal to $|E_2|$, which implies that one supermode is predominantly localized in the gain waveguide, experiencing exponential amplitude increase, while the other supermode is primarily localized in the loss waveguide, undergoing exponential amplitude decay. As a result, only one supermode effectively survives. As illustrated by Figure 5.1c (bottom), Light consistently exits from Channel 1 with gain, regardless of the input. The optical wave propagation optical wave propagation clearly follows a non-reciprocal behavior. It's important to point out that the prior discussion applies to PT-symmetric systems featuring a symmetric gain/loss profile. However, any coupled system with an asymmetric gain/loss profile can be mathematically converted into a PT-symmetric system. Hence, achieving PT symmetry in practice doesn't necessitate a perfectly symmetrical gain/loss profile.

Supersymmetry (SUSY) theory, initially introduced within the context of particle physics, has emerged as a prominent subject in modern physics. Its applications span across various disciplines, including quantum mechanics [76, 77], condensed matter

physics [78] to photonics [79, 80]. SUSY exhibits notable effectiveness in tailoring mutual interactions in any arbitrary lattice of evanescently coupled elements, regardless of its complexity and size [69]. With the unbroken SUSY, the lattice Hamiltonian can be transformed into a new superpartner Hamiltonian with a reduced matrix dimension. This new Hamiltonian preserves nearly identical eigen spectrum, except for the absence of the ground/lowest energy mode. To illustrate this, consider a one-dimensional infinite potential well as an example. In the unbroken SUSY regime, all eigenvalues of the primary potential are exactly matched those of its superpartner, except for the ground state. When the ground state finds an equivalent counterpart in its superpartner, bearing the same eigenvalue, the supersymmetry is broken. Likewise, in the field of optics, one can begin with a given primary optical structure and construct its superpartner, which shares an identical eigen spectrum except for the fundamental mode.

Recently, it was recognized that the integration of SUSY with PT-symmetry non-Hermitian photonics provides innovative avenues for achieving mode control and selection in the design of lasers and laser arrays [67]. In laser systems, mode discrimination, the net gain difference between the fundamental mode and higher-order modes, is the most critical factor that determines whether the laser operates in a single-mode configuration. SUSY proves to be a powerful approach for enhancing the mode discrimination, enabling only the selected mode to participate in the lasing action. By establishing an unbroken SUSY, enhancing mode discrimination becomes readily attainable through selectively pumping the primary optical structure or introducing the additional optical loss to the superpartner. This method ensures that undesired higher-

order modes adhere to PT-symmetry, experiencing the balance of gain and loss and effectively filtering them out, while the desired fundamental mode remains unaffected in the PT-broken region. Thus, this approach provides unprecedented control over single-mode operation. Within this framework, we put forward the design of the electrically pumped high-power single-mode Triple Ridge Waveguide (TRW) laser.

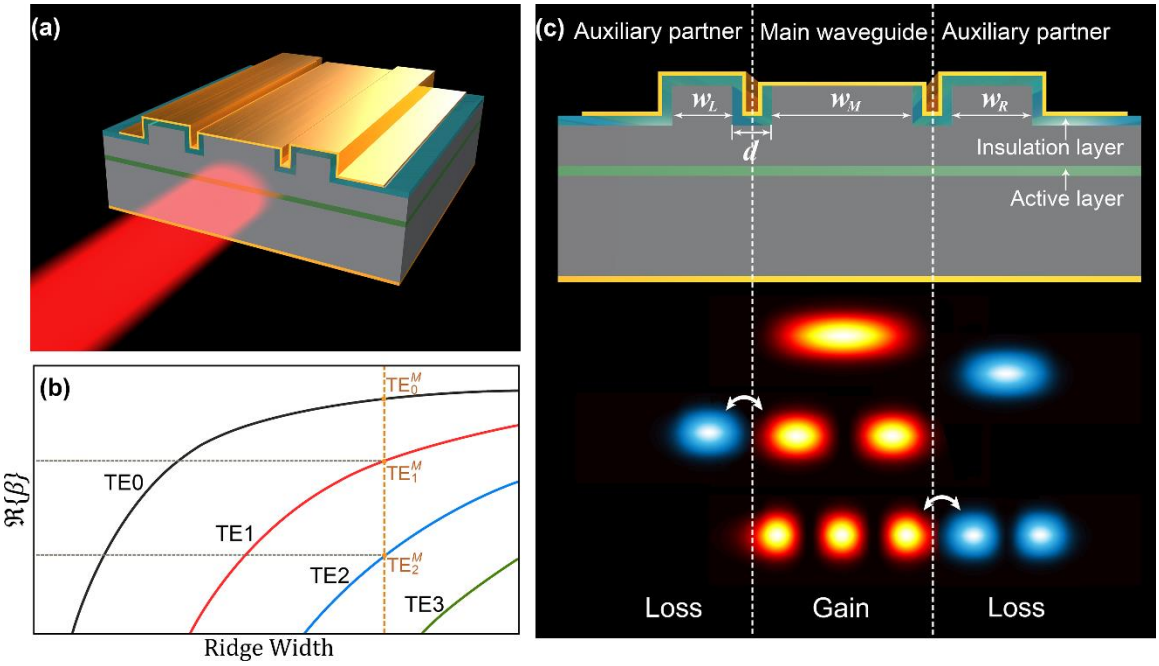

Figure 5.2 Fundamental principle of single-mode lasing in the proposed TRW laser. (a) Schematic of the TRW laser structure. (b) The propagation indices of guided modes in a single ridge waveguide structure as a function of the ridge width. (c) Cross-section of the TRW laser structure with the illustration of mode coupling mechanism.

Figure. 5.2(a) illustrates the schematic view of our proposed TRW laser structure. Instead of using the laser arrays in the previous SUSY arrangement [67], our proposed TRW structure consists of a main broad waveguide in the middle and a pair of auxiliary partner waveguides on both sides. We allow the main waveguide to support high order

modes so that the waveguide width is increased without reducing the index contrast. The pump current is injected in the main waveguide to provide optical gain, while extra optical loss is introduced in the two auxiliary partner waveguides. The auxiliary waveguides are designed to support guided modes that only couple with the high order modes of the main waveguide, which effectively filters out these high order modes in the main waveguide. By appropriately manipulating the modal discrimination of the modes in the TRW structure, one can effectively suppress all the undesired modes below the lasing threshold while keeping the fundamental one almost intact, thereby ensuring the single-mode lasing with a larger emitting aperture and accordingly a higher output power than a conventional RW laser. Compared with SUSY laser array, the proposed TRW is simpler in design and thus experimental implementation. Additionally, avoiding etching in the main ridge waveguide is beneficial to achieving lower optical internal loss and better electrical characteristics. Moreover, the proposed TRW structure does not require a small effective index difference, making it less susceptible to the carrier induced index suppression and thus providing the stable single-mode operation at high injection currents. Moreover, the proposed strategy has no specific requirements for the epitaxial structure and is compatible with the fabrication of a conventional RW laser, making it promising for low-cost and mass production. It is worth noting here that our proposed strategy is different from the reported evanescent spatial filtering in RW or broad area lasers [67, 81-83], which introduces selective losses for higher order modes by applying the fact that higher order modes experience greater spatial extent outside the guide (inside the lossy region). These methods do not require phase matching and thus provide

relatively low modal discrimination. In addition, since it is difficult for them to keep the fundamental mode intact, the lasers usually show increased thresholds and decreased slopes. By virtue of the novel mode engineering in our proposed TRW structure, more efficient and stable mode filtering with much better modal discrimination can be realized in practice.

As shown in the schematic and cross-section views of the proposed TRW structure (Figure 5.2 (a) and (c)), the primary (main) waveguide is formed by a broad ridge which supports three transverse electric (TE) modes. To implement the unbroken optical SUSY framework, we construct a lossy superpartner (two lossy auxiliary partner waveguides in the TRW structure) with propagation constant values that match with those of guided modes associated with the main waveguide apart from the fundamental mode. To roughly obtain the ridge widths of the two auxiliary waveguides, we sweep the propagation constants of TE modes versus the ridge width in a single ridge waveguide, as shown in Figure 5.2(b). The propagation constants β are generally complex in a laser cavity. In this figure only the real parts of propagation constant are considered. As indicated by the vertical dotted line in Figure 5.2(b), the main waveguide supports three modes TE_0^M, TE_1^M and TE_2^M. As indicated by two horizontal dotted lines, the TE_1^M and TE_2^M modes can respectively find a match in $\Re\{\beta\}$ with the narrower ridge waveguides. In a weakly coupled waveguide system, according to the coupling mode theory, the coupling strength between two modes is determined by the coupling coefficient, phase detuning (difference in $\Re\{\beta\}$) and gain-loss contrast. Efficient coupling will split the coupled modes into symmetric (in-phase) and anti-symmetric (out-of-phase) supermode pairs.

Therefore, by engineering the two lossy narrow auxiliary waveguides to phase match with the higher order modes in the main waveguide, all the higher order modes will split into supermode pairs except for the fundamental mode. which is the so-called unbroken case in the SUSY laser array. Since extra optical loss has been added in the auxiliary waveguides, the supermodes will experience higher modal loss and accordingly higher lasing thresholds. In this regard, we should appropriately control the coupling coefficient in the TRW laser structure in such a way that the amplitude distributions of the supermodes have a large spatial overlap with the lossy region. On the other hand, the fundamental mode TE_0^M in the main waveguide, which is decoupled with the lossy auxiliary waveguides, will hold the lowest threshold in the cavity and becomes the lasing mode in the mode competition. Therefore, the proposed TRW structure can effectively suppress the unwanted higher order modes and ensure the single mode lasing in a broad ridge waveguide. As a side note, the main waveguide in the TRW structure is not restricted to support only three modes, which will be discussed in detail later.

5.2 TRW laser design and experimental results

5.2.1 TRW laser design

In this section, we will present two TRW designs, in which a conventional InGaAs/GaAs epitaxial wafer with symmetric waveguide design is employed. Note that the proposed TRW strategy is applicable to any epitaxial structure. We assume that the insulation layer (SiO_2) has a thickness of 200nm, and the p-metal contact has a thickness of 300nm. The peak photoluminescence wavelength of the InGaAs SQW is approximately 1μm. Therefore, in the subsequent simulation, we assume the operation

wavelength (λ) to be this value. The widths of the three ridges are respectively denoted as w_L (left), w_M (main) and w_R (right), as depicted in Figure 5.2(c). The two trench widths between the three ridges are set equal, and consequently referred to as d. Mode analysis is conducted using the Finite Difference Eigenmode (FDE) solver in Lumerical. The semiconductor materials are represented by a complex refractive index, denoted as $n=n_r+i\cdot n_i$, with the real refractive index, n_r, calculated based on the material's composition, and the imaginary part $n_i=-g\lambda/4\pi$, where g represents the gain (positive) or loss (negative). The value of background internal loss depends on specific the epitaxial wafer used and is unrelated to the calculated modal discrimination. Two strategies are available to increase mode discrimination. Strategy One involves providing equal gain to all modes and introducing higher loss for the unwanted higher-order modes. Strategy Two, on the other hand, involves an equal loss for all modes while providing a higher gain to the fundamental mode than the higher-order modes. The two strategies can be combined by implementing higher gain and lower loss for the fundamental mode, while employing lower gain and higher loss for the unwanted higher-order modes. In the simulations, we follow Strategy One and apply uniform gain to the entire structure while assuming a constant loss of 20 cm^{-1} in the auxiliary waveguides. In this section, our primary emphasis is on elucidating the operational principles of the TRW laser structure. The methods for introducing additional loss will be addressed in the subsequent section. Furthermore, the simulation does not account for charge transport and thermal effects in diode lasers. However, it's important to note that the thermal lens effect under continuous

wave (CW) mode can be well addressed in the TRW structure through pre-design adjustments and meticulous heat control.

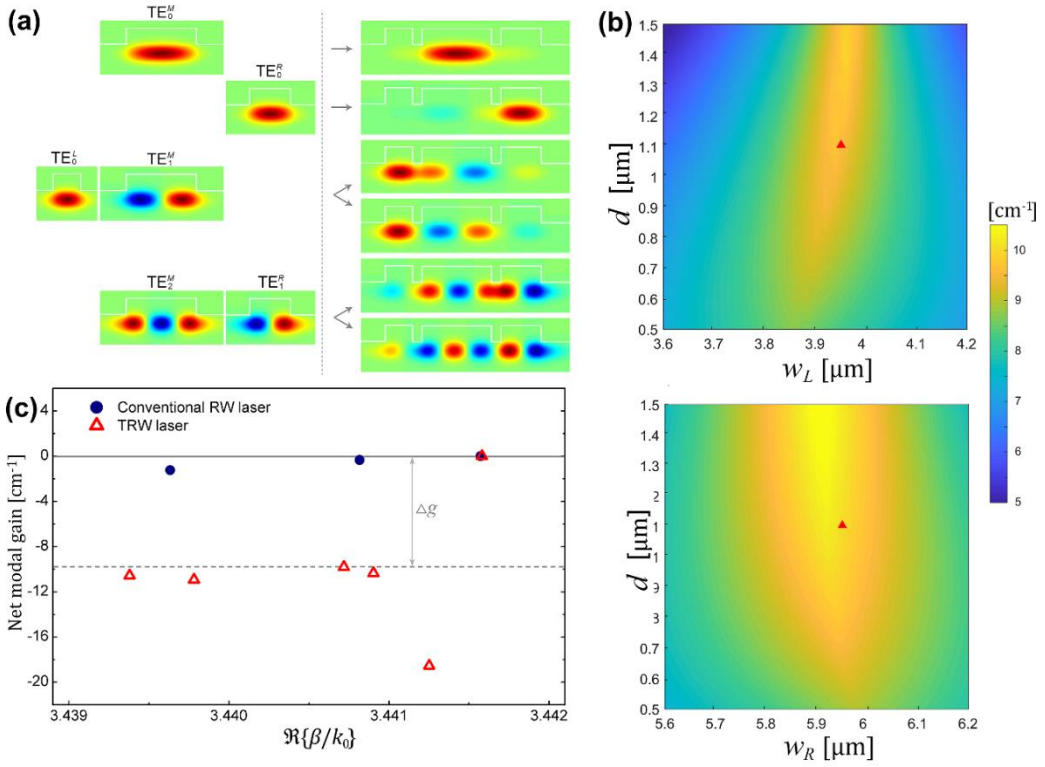

Figure 5.3 The mode analysis for TRW1 laser with the main waveguide width equal to 10μm. (a) Left: Electric field component Ex distributions of the TE modes supported by the isolated RW structures; Right: Ex distributions of the TE modes in the TRW structure sorted from the lowest-order (top) to the highest-order (bottom) mode (The geometric parameters are w_L = 3.95μm, w_M = 10μm, w_R = 5.95μm, and d = 1.1μm). (b) Upper: The sweeping result for the smaller modal discrimination of the supermodes formed by the coupling between TE_1^M and TE_0^L as a function of the left waveguide width w_L and trench width d. Lower: Sweeping result for coupling between TE_2^M and TE_1^R as a function of the right waveguide width w_R and trench width d. (c) The net modal gain of the modes in the conventional RW laser (solid circles) and the modes in the TRW1 laser structure (hollow triangles).

We first consider a TRW laser design with the main waveguide supporting three modes. In the simulation, only TE modes are considered because the gain for a compressively strained QW is much higher for the TE polarization [84]. In this design, the etching depth is set to be 900nm and accordingly, the effective index difference Δn_{eff} between the ridge and trench is about 3.5e-3. This relatively large built-in Δn_{eff} can effectively suppress the carrier induced anti-waveguide effects. At this etching depth, the isolated main RW with w_M = 10μm supports three TE modes, as shown in Figure 5.3(a). As depicted in the schematic diagram of Figure 5.2(c), the TE_0^L and the TE_0^R modes are respectively chosen to couple with the TE_1^M and the TE_2^M modes. It can be found in Figure 5.2(b) that the bottom horizontal dotted line (associated with the TE_2^M mode) also has an intersection with the TE1 dispersion curve at a relatively larger width, which can also be utilized to couple with the TE_2^M mode. Considering that the higher order modes are less confined and thus typically have larger coupling coefficients than lower order ones, TE_1^R mode is chosen to couple with TE_2^M in the design instead of TE_0^R. In order to find the optimum auxiliary waveguide widths and trench widths, parameter sweeping based on two waveguide coupling is performed. The upper panel of Figure 5.3(b) plot the sweeping result for the modal discrimination of the two coupled waveguides (the main waveguide and left side waveguide), where the modal discrimination is defined as the modal loss difference between the lowest-loss fundamental mode and the second lowest loss high order mode. It can be found that a larger trench width indicates a higher modal discrimination at the optimum auxiliary waveguide width but with a smaller margin of error. In practice, it is better to have a larger parameter margin to compensate the

fabrication errors, and therefore, a moderate trench width of 1.1μm is chosen in this design. The lower panel of Figure 5.3(b) shows the sweeping result for the coupling between the main waveguide and right waveguide. Owing to the larger coupling coefficient, a larger bright area, i.e., larger margin of error, is clearly observed. The triangle in Figure 5.3(b) indicates the final selected values for the waveguide and trench widths. Figure 5.3(c) shows the comparison of the net modal gain of the modes in the designed TRW laser structure (red triangles) and in the conventional RW laser (navy dots). Clearly, the modal discriminations in the conventional RW structure are very small. All the three modes are easy to reach their thresholds, leading to the multimode lasing and degraded beam quality. After introducing two lossy auxiliary waveguides, apart from the fundamental mode, the higher order modes couple with lossy modes and split into supermodes with much enhanced losses. With a large modal discrimination, the stable single mode lasing can be obtained. In the TRW laser, as indicated in the Figure 5.3(c), a high modal discrimination Δg =9.8 cm^{-1} is achieved for the single-mode operation.

As mentioned before, the proposed TRW structure is capable of filtering out more than two higher order modes. In what follows, a TRW2 laser design with w_M = 12μm is investigated. The etching depth is also assumed to be 900nm. In this case, the isolated main waveguide supports four modes, denoted as TE_0^M to TE_3^M, as shown in Figure 5.4(a). Same as the first design, a TE_0^L and a TE_1^R dissipative mode are utilized in the second design to couple with the TE_1^M and the TE_2^M mode, respectively. The panel *i* in Figure 5.4(b) shows the modal discrimination of the supermodes formed by the TE_1^M-TE_0^L

coupling as a function of the auxiliary waveguide and trench widths. We can see that the modal discrimination drops sharply at a larger trench width around 1.35μm, indicating a significant decrease in the coupling efficiency. A continual increase in the trench width will drive it into the so-called parity-time (PT) symmetry broken region [75], i.e., no coupling at all. It can be found that the critical trench width where PT-breaking occurs in this design is less than that in the TRW1 design, because the guided modes are better confined in a broader waveguide, leading to a smaller coupling coefficient at the same trench width. Therefore, a smaller trench width of 0.9μm is selected in this design, and accordingly, w_L is determined to be 4.9μm. In addition to the TE_0^L mode, this left auxiliary waveguide also supports a higher order mode TE_1^L, whose real propagation constant is close to that of the TE_3^M mode. Panel *ii* plots the parameter sweeping result for the TE_3^M-TE_1^L coupling. There is a very large parameter variation margin due to strong mode coupling. This is because both TE_3^M and TE_1^L have a long evanescent tail extending outside waveguide. The sweeping result for TE_2^M -TE_1^R coupling is plotted in Panel iii with the red triangle indicating the selected w_R and d values. Despite that the highest order mode TE_2^R supported by the right waveguide is far from the phase matching with TE_3^M, it helps to enhance the losses of the supermodes formed by TE_3^M and TE_1^L. The out-of-phase TE_3^M and TE_1^L supermode has a smaller $\Re\{\beta\}$, which is close to that of TE_2^R, and thus shows a higher loss than the in-phase supermode. The net modal gain of the modes of TRW2 is shown as the hollow triangles in Figure 5.4(c). Compared with the conventional RW (solid circles), the modal discrimination Δg for the single mode lasing is increased by 9.5cm^{-1}.

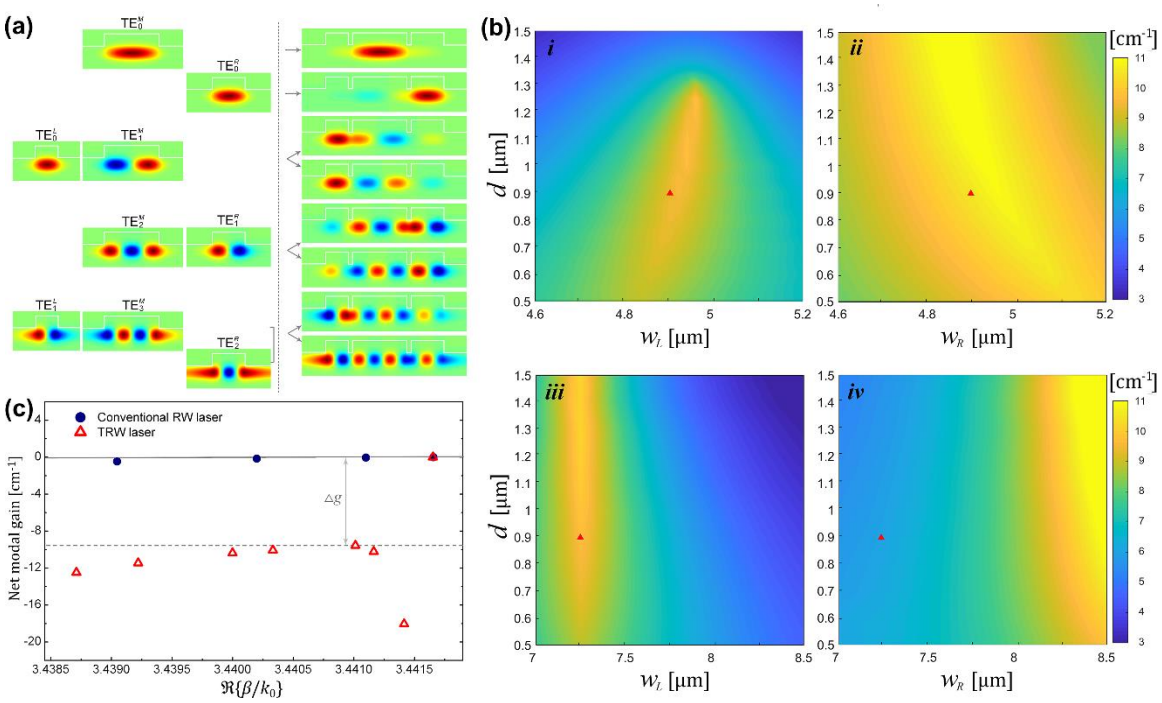

Figure 5.4 The mode analysis for TRW2 laser with the main waveguide width equal to 12μm. (a) Left: Electric field component *Ex* distributions of the TE modes supported by the isolated RW structures; Right: *Ex* distributions of the TE modes in the TRW structure sorted from the lowest-order (top) to the highest-order (bottom) mode (the geometric parameters are w_L = 4.9μm, w_M = 12μm, w_R = 7.25μm, and d = 0.9μm). (b) The sweeping results for the smaller modal discrimination of the supermodes formed by the coupling between: i). TE_1^M and TE_0^L modes; ii). TE_3^M and TE_1^L modes; iii). TE_2^M and TE_1^R modes, and iv). TE_3^M and TE_2^R modes. (c) The net modal gain of the modes in the conventional RW laser (solid circles) and the modes in the TRW2 laser structure (hollow triangles).

The lasing wavelength is determined by the longitudinal modes within the cavity. Given the broadband gain spectrum of the semiconductor quantum well, the lasing wavelength may exhibit some variation across different cavities. In Figure 5.5(a), the impact of this wavelength variation on modal discrimination Δg is illustrated. It is evident

that Δg changes by only 0.5 cm^{-1} as the wavelength increases by 60 nm, underscoring the system's robustness against the wavelength variation. Another parameter affecting the modal discrimination in practice is the etching depth. The impact of etching depth deviation on modal discrimination is shown in Figure 5.5(b). In the case of the TRW1 design, as the etching depth varies within a range of ±30nm, Δg shifts by approximately 2.2 cm^{-1} while still maintaining significant modal discrimination for the stable single mode operation.

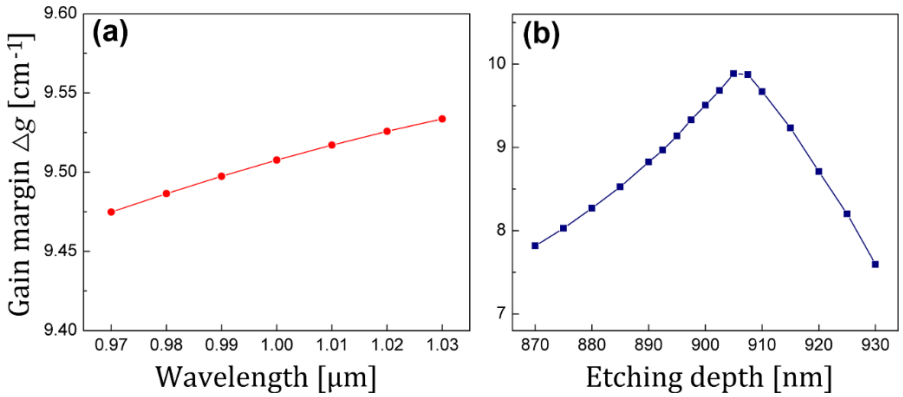

Figure 5.5 The effect of wavelength variation (a) and etching depth deviation (b) on the gain margin Δg for single mode operation in the TRW1 design.

5.2.2 Experimental implement

Following the above TRW designs, we fabricate TRW lasers with main waveguide width of w_M = 10μm and trench width d = 1.2μm. We explore various combinations of left and right auxiliary waveguide widths. Figure 5.6 displays the SEM image of the cross-section of a fabricated TRW laser. The fabricated TRW lasers are tested under Quasi-Continuous Wave (QCW) mode with a pulse width of 500nm and a duty cycle of 10%. The measured lateral far-field profiles at low injection current are

represented by the red curve in Figure 5.7. It exhibits a single-lobe Gaussian-like far-field profile with the Full Width at Half Maximum (FWHM) angle of 7.4°. For comparison, the far-field profile of a conventional RW laser with the same ridge width of 10μm is depicted as the blue curve in Figure 5.7, which displays a double-lobe pattern with a significantly larger FWHM angle of 14° at the same injection current. This contrast illustrates the filtering effect achieved by the TRW laser.

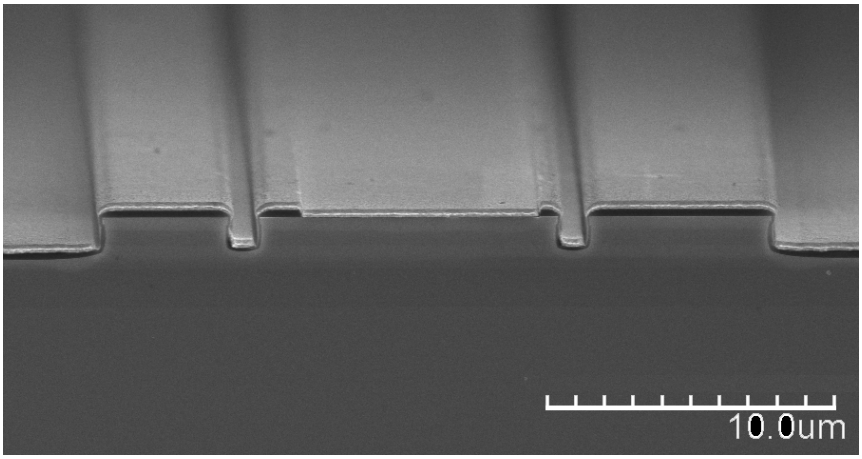

Figure 5.6 SEM image of the cross-section of the TRW laser.

However, the effectiveness of the mode filtering in TRW lasers diminishes as the injection current increases. In these TRW lasers, modal discrimination is solely provided by selective pump to the main waveguide. However, due to carrier diffusion issues, carriers in the quantum well can easily reach the two side auxiliary waveguides. This results in a small gain difference between the main and the auxiliary waveguides, leading to reduced modal discrimination. Consequently, higher order modes begin to lase at higher injection levels. As illustrated by Figure 5.8(b), which displays the near-field profile of the TRW laser, despite its lower intensity, we observe light distribution within

the auxiliary waveguide region. This indicates the issue of carrier diffusion, which provide gain in the auxiliary waveguide region. To address carrier diffusion, we can employ ion implantation within the trenches to create highly resistant areas, thereby hindering carrier diffusion. This can effectively turn the quantum well in the auxiliary waveguide into a source of loss instead of gain. Apart from this method, an alternative approach involves directly integrating additional loss mechanisms into the auxiliary waveguides, a subject we will elaborate on in the following section.

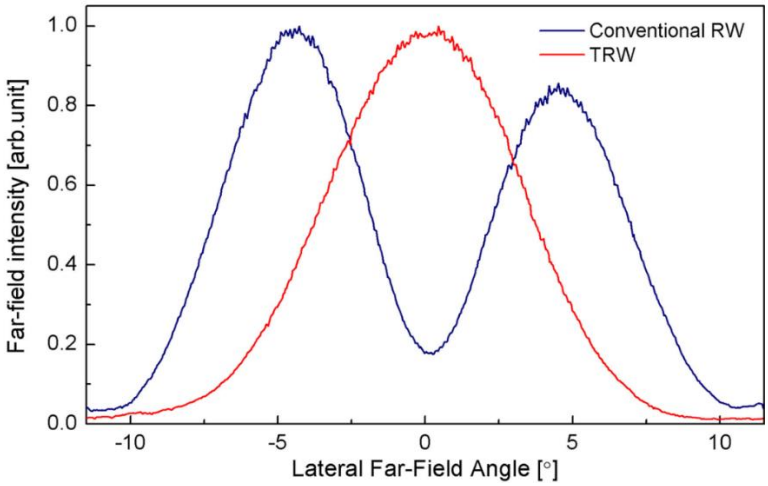

Figure 5.7 Lateral far-field profiles of a conventional RW laser with ridge width 10μm (navy) and a TRW laser (red).

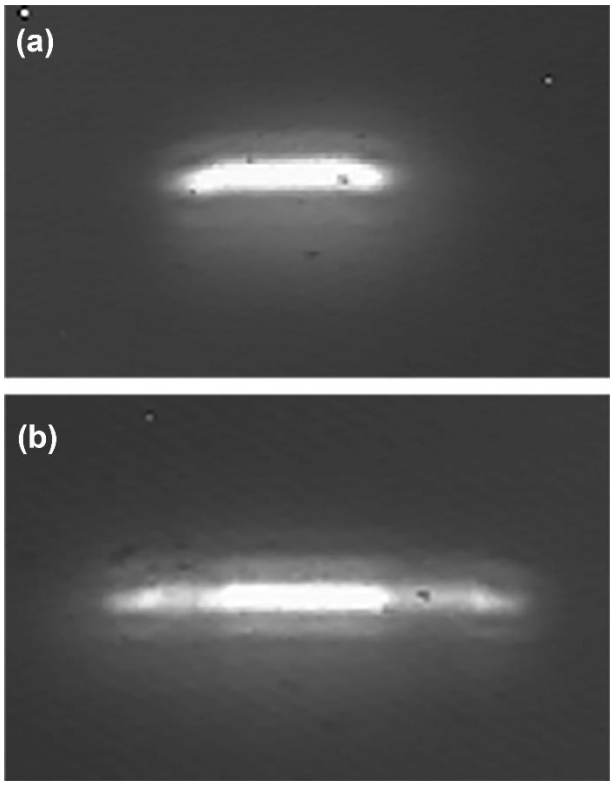

Figure 5.8 Near-field profiles of a conventional RW laser with ridge width 10μm (a) and a TRW laser (b).

5.3 TRW lasers with deep-etched trenches introducing extra loss in auxiliary partner waveguides

As discussed in Section 5.2, achieving high mode discrimination in TRW lasers at elevated output power levels is challenging without introducing additional loss to the auxiliary waveguides. The general methods for introducing extra loss to waveguides include ion implantation, selective area regrowth, depositing metallic films, and so on. In this context, we put forward a technique for introducing loss in the auxiliary waveguide by incorporating trapezoidal deep-etched trenches, as illustrated in Figure 5.9. This method can effectively enhance mode discrimination in TRW lasers and facilitate stable single-mode operation at higher output power levels.

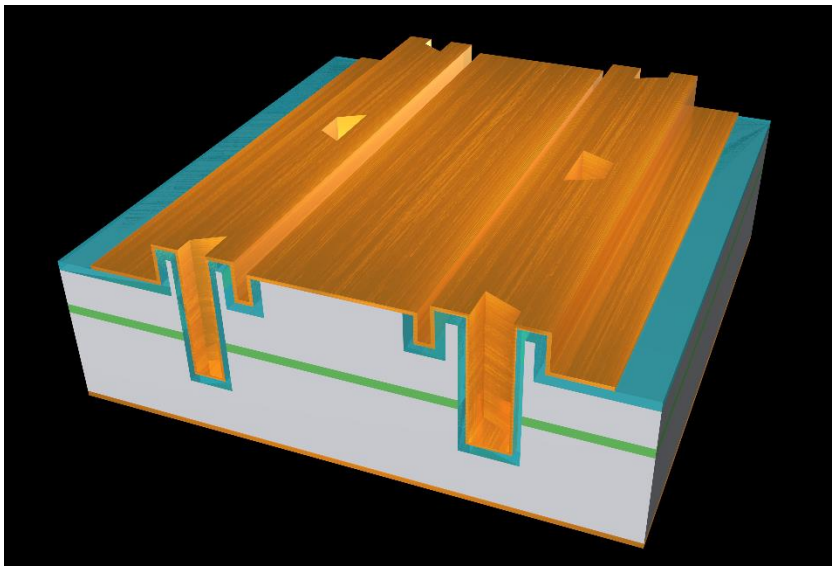

Figure 5.9 Schematic of the TRW laser structure incorporating trapezoidal deep-etched trenches

The deep-etched trenches effectively convert guided modes into leaky modes, thereby increasing the mode propagation loss. We design the trenches in a trapezoidal shape to maximize the introduced loss, as well as alter the propagating direction of leaky modes to mitigate the disruption with the fundamental mode. We simulate the propagation of TE mode through various deep trench shapes using Lumerical FDTD solutions. In the simulations, we utilize a mode source propagating in the positive *x*-direction. Figure 5.10 shows the electric field distribution near the active region. When the deep trench edge is oriented perpendicular (90^o) to the mode propagation direction (a) or at a 45^o angle (c), a portion of the guided mode are reflected back. However, when the deep trench edge forms a 63.5^o angle with the mode propagation direction (b), the guided mode will almost entirely transform into a leaky mode, propagating away from the main waveguide, without causing disturbance to the fundamental mode. This represents the

desired outcome. Compared with other methods of introducing loss, our proposed trapezoidal deep-etched trenches offer several advantages: it is compatible with standard ridge laser preparation technology, which facilitates easy fabrication; it can preserve the refractive index profile, streamlining the design process; and it can effectively introduce high loss to the auxiliary waveguide with no disruption to the fundamental mode.

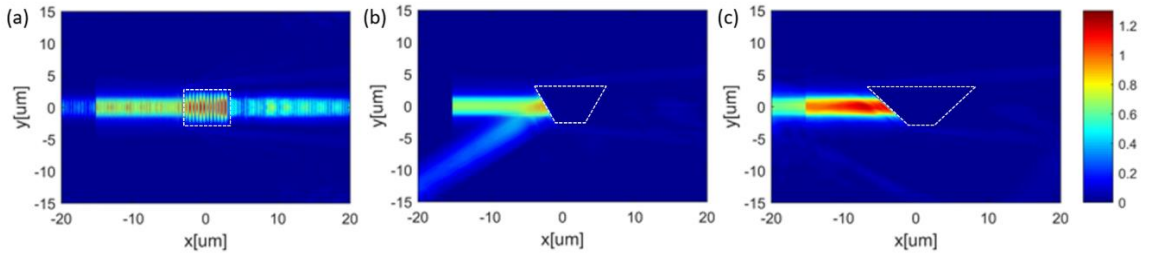

Figure 5.10 Electric field distribution of TE mode propagation through different deep trench shapes with inclined sides at various angles relative to the x-axis: (a) 90^{o}, (b) 63.5^{o}, and (c) 45^{o}.

5.4 Conclusion

In this chapter, we have demonstrated a novel TRW structure in edge-emitting semiconductor lasers, enabling high-power single-transverse-mode operation based on the principle of unbroken SUSY. This structure incorporates a pair of lossy auxiliary waveguides to suppress unwanted higher-order modes within the laser cavity. Through precise engineering of the TRW structural parameters, we achieve large modal discrimination for stable single-mode lasing. We further demonstrate that the proposed TRW laser exhibits robustness against variations in lasing wavelength and structural parameters, making it highly suitable for high-yield and mass production. Near-diffraction-limited output is experimentally observed in the proposed TRW laser,

demonstrating the effectiveness of the proposed mode filtering mechanism. To enhance the mode discrimination in practice, we propose to introduce trapezoidal deep-etched trenches in the auxiliary waveguide. The deep-etched trenches effectively convert guided modes into leaky modes, thereby effectively increasing propagation loss for undesired higher-order modes, thus achieving more stable single-mode operation at high power output.

Chapter 6

HIGH POWER NARROW LINEWIDTH ON-CHIP LASER BASED ON SELF-INJECTION LOCKING

In the previous chapters, our primary focus has been on achieving high-power and high-efficiency single transverse mode semiconductor laser outputs. A compelling demand for laser sources exhibiting narrow linewidth and low phase noise has arisen across a wide range of innovative technologies. These include, but are not limited to, advanced optical communication systems [85], highly sensitive sensor technologies [86], LIDAR systems for autonomous traffic [87], quantum optics [88], and atomic and molecular physics [89]. Given the intrinsic ease of integration of semiconductor lasers, the development of high-power, narrow linewidth semiconductor lasers holds the promise of substantially propelling the evolution of on-chip functional photonic circuits. Consequently, in this chapter, we employ the self-injection locking technique to combine our demonstrated high-power ridge waveguide Fabry–Pérot (FP) lasers with photonic integrated circuits (PICs), thus realizing high-power on-chip tunable narrow linewidth laser output.

6.1 Introduction

Hybrid integration of PIC chips with III-V gain medium represents a promising avenue for the development of compact, tunable, and narrow-linewidth lasers [90-94]. Many previous research efforts have involved the integration of photonic chips with III-V reflective semiconductor optical amplifiers (RSOAs), resulting in compact tunable narrow-linewidth external cavity lasers (ECLs) [91, 95, 96]. Nevertheless, a notable challenge in ECLs lies in the stringent requirements for minimizing reflections and coupling losses between the PIC and gain chips. Any loss or reflection can significantly affect the lasing dynamics, especially when operating at high power levels [97]. An alternative strategy for achieving narrow-linewidth hybrid integrated lasers is the utilization of self-injection-locking lasers. In contrast to ECLs, this category of lasers achieves linewidth narrowing by locking a semiconductor laser, such as a FP or DFB laser, to a high-quality-factor microresonator via the self-injection locking effect. Employing lasers instead of RSOAs offers the advantage of increased robustness to coupling loss and fluctuations in reflections. Recent studies have demonstrated self-injection locking lasers that offer ultra-narrow linewidth on-chip laser output with mode-hop-free fine-tuning capabilities of up to tens of GHz as well as broadband coarse tuning capabilities of up to tens of nanometers [98-101]. Nevertheless, the optical power of these lasers is comparatively low. Consequently, our focus is directed towards achieving high-power narrow-linewidth on-chip laser output.

Figure 6.1 shows the schematic of our self-injection locking laser, in which a ridge waveguide FP laser diode is butt-coupled to a high Q microring resonator. A

feedback loop mirror is placed at the drop port of the microring resonator to reflect a portion of the resonant light back towards the FP laser, thereby facilitating self-injection locking. To enable phase control, microheaters are integrated on top of the microring resonator and the bus waveguide. When the microring resonator is detuned from any modes of the FP laser, the microring is decoupled from the system, resulting in the hybrid system emitting laser output with multiple longitudinal modes. When the resonance frequency of the microring resonator is aligned with a longitudinal mode of the FP laser, some of lasing optical power will be reflected back to the laser cavity. If the external phase delay precisely enables constructive interference between the feedback field and the light field within the laser cavity, the hybrid system transitions into the locked regime. Consequently, it emits a stable single-frequency laser output characterized by a narrow linewidth.

In our self-injection locking laser setup, we employ 7μm-wide ridge waveguide FP lasers as the gain chips. For the passive chip component of our setup, we utilize the Silicon nitride (Si_3N_4) PIC platform, which incorporates a Si_3N_4 layer as the waveguide layer and silicon dioxide (SiO_2) as the cladding layer. The Si_3N_4 PIC platform offers numerous advantages, such as broadband transparency from visible to near-infrared wavelengths, low propagation loss waveguide construction, watt-range power handling due to minimal two-photon absorption, temperature stability for varying environmental conditions, and compatibility with CMOS technology for large-scale manufacturing [90, 102, 103].

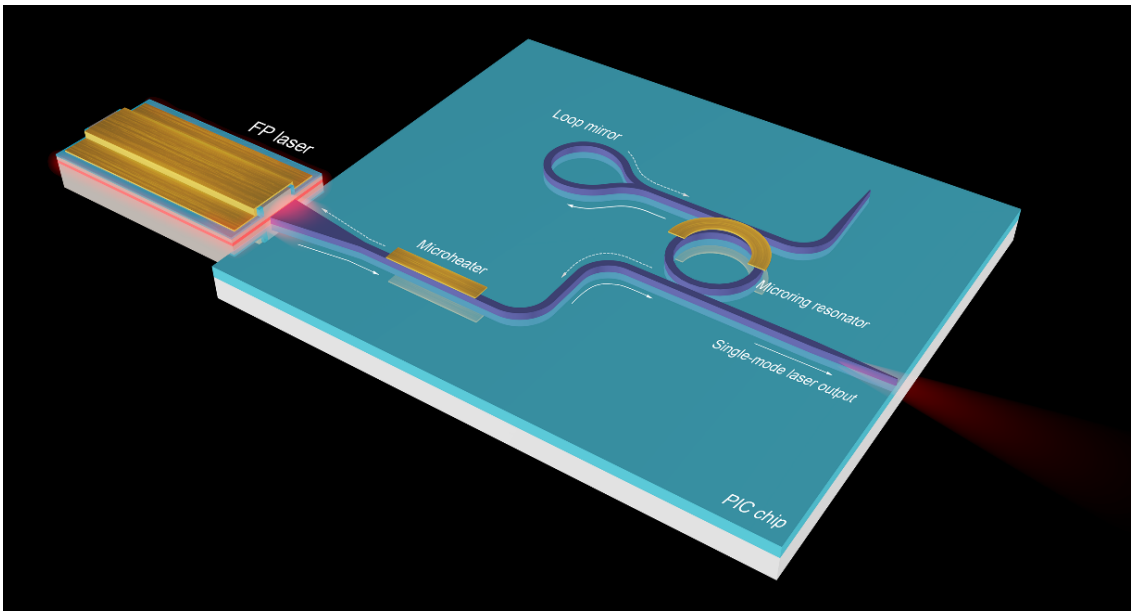

Figure 6.1 Schematic of the self-injection locking laser

In the following section, we will present the fabrication process utilized for our PIC chips. Subsequently, in Section 6.3, we will delve into the design of the PIC chips for self-injection locking lasers and provide their characterization results. Finally, in Section 6.4, we will discuss the experimental measurement results of our self-injection locking lasers.

6.2 Fabrication of PIC chips

Figure 6.2 present the fabrication process of our Si_3N_4 PIC chips. We procure 300nm-thick Si_3N_4 layer on a 4μm SiO_2/Si wafers from Waferpro, with the Si_3N_4 deposition achieved through Low-Pressure Chemical Vapor Deposition (LPCVD).

Step (a): Surface cleaning

This step involves a standard sample cleaning procedure and dehydration bake.

Step (b) and (c): Ebeam lithography (EBL) to write PIC layout pattern

ZEP520a is employed as EBL resist, and its recipe has been discussed in Section 3.1.2. However, when it comes to fabricating PIC with significantly smaller critical dimensions compared to ridge waveguide lasers, an anti-charging layer (Espacer300) should be applied following the coating of the EBL resist. The purpose of the anti-charging layer is to mitigate the accumulation of negative charges on the insulating substrate, such as SiO_2. These charges could potentially lead to pattern distortion. The recipe of Espacer 300 can be found in Table 6.1. Espacer300 does not require pre-baking or development steps. Upon finishing the EBL writing process, Espacer300 should be directly removed by rising with DI water.

Table 6.1 Recipe of Espacer 300

Parameter	Value
Spinning	Acc 2000rps/s, SS 2000rpm, Dwell 30s

Step (d): Si_3N_4 dry etching

We apply the procedure described in Section 3.1.2 for dry etching Si_3N_4, which is the same recipe used for SiO_2 dry etching. Please be aware that the etch rate of Si_3N_4 is slower than SiO_2, and the etch rate can vary significantly based on the condition of the chamber cleaning. If the test etching rate is significantly lower than the normal value (~2nm/s), please refrain from proceeding with the etching of real samples, because prolonged dry etching time can potentially result in the complete removal of the EBL resist.

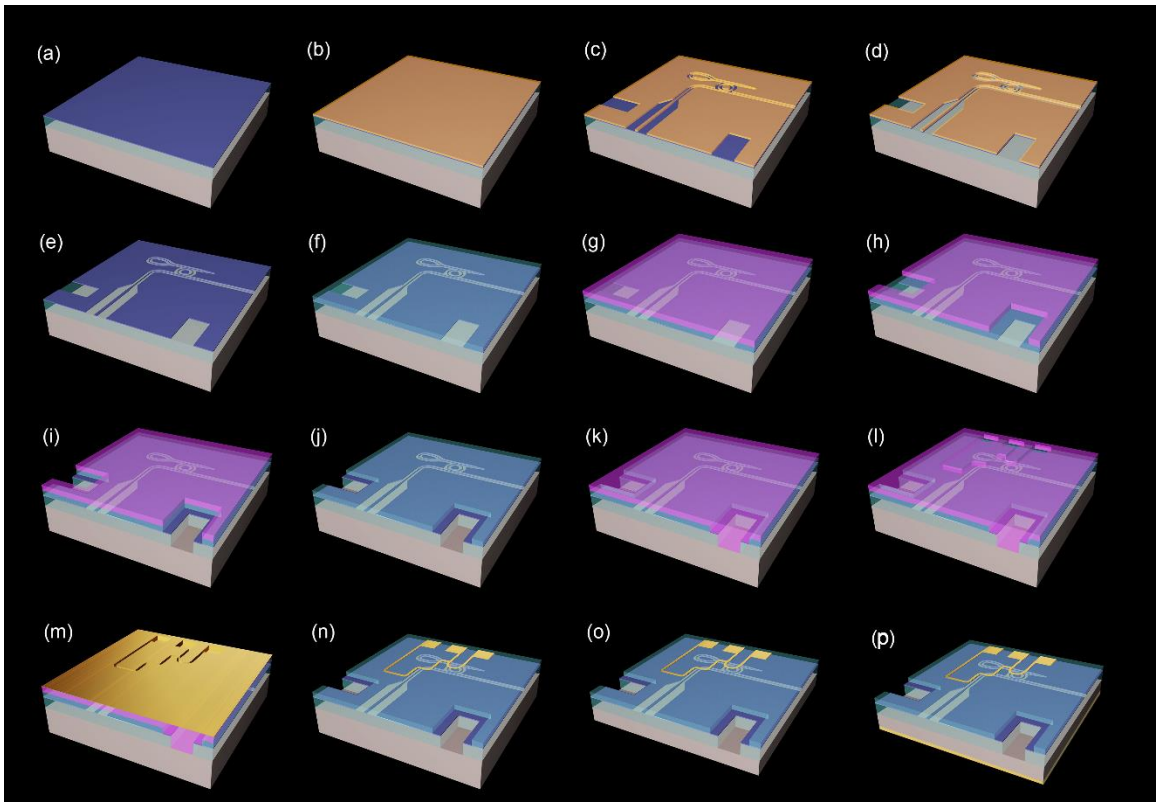

Figure 6.2 Fabrication processing flow of PIC chips on Si_3N_4/Si platform

Step(e): EBL resist removal

Step(f): SiO_2 deposition

2μm SiO_2 is deposited by using PECVD to serve as the up cladding layer.

Step (g) and (h): Photolithography for scribing window open

The scribe and break tool exhibits effectiveness solely with crystalline materials. As SiO_2 and Si_3N_4 are amorphous materials, the 6μm layer of SiO_2 on silicon substantially hampers the scribing process, leading to a notable decrease in the cleaving success rate. Therefore, it is crucial to pre-remove the SiO_2 near the intended scribing locations, thereby exposing the Si substrate.

It is advisable to use a positive photoresist here instead of a negative one. The key advantage of a positive photoresist lies in its requirement for exposure solely within the scribing window open areas. In contrast, a negative photoresist necessitates exposure across the entire sample area except for the scribing window open area. This distinction becomes particularly significant when considering the presence of contaminants or particles atop the photoresist layer. With a negative photoresist, these contaminants may lose the protection of the photoresist due to remaining unexposed. Consequently, this situation will result in damage to the cover cladding within the critical pattern area during the subsequent etching process. Utilizing a positive photoresist can effectively mitigate this issue.

Step (i): SiO_2 wet etching

We employ BOE to eliminate the SiO_2 within the scribing window open. SiO_2's etch rate in BOE is approximately several tens of nanometers per minute, depending on the window's size. Consequently, etching through 6μm of SiO_2 typically requires around 1 to 2 hours. It's important to note that between the upper and lower SiO_2 cladding layers, there is a 300nm Si_3N_4 waveguide core layer. Si_3N_4 exhibits an exceptionally slow etch rate in room-temperature BOE (almost negligible), at just a few nanometers per hour [104, 105]. Therefore, as depicted in the diagram of steps (c) and (d), we have used EBL and Si_3N_4 dry etching to remove the Si_3N_4 in the scribing window open areas.

To enhance the protective properties of the photoresist in BOE, a hard bake treatment is required (180°C for 10 minutes). When BOE etches through to the Si_3N_4

layer, the Si_3N_4's dry etch window can further serve as a hard mask to shield other SiO_2 areas from being etched by BOE.

Step (j): Photoresist removal

The removal of hard-baked photoresist demands an extended processing time. Hence, a method involving the utilization of heated NMP combined with ultrasonic agitation is employed for its elimination.

Step (k) and (j): Photolithography for micro-heater

Negative resist NR9-1500P is used. Its recipe has been discussed in Section 3.1.2

Step (m): Metal deposition

The metal layer employed for creating the micro-heater consists of a 450nm thick layer of Chromium (Cr) and a 50nm thick layer of Platinum (Pt).

Step(n): Lift-off

Step(o): Lapping

The sample is lapped down to approximately 170μm to achieve the best cleaving results and success rate.

Step(p): Backside metal deposition

In order to facilitate superior heat dissipation and enable optimal solder bonding of sample onto the thermal spreader, it is necessary to deposit a metallic layer on the backside of the sample.

Table 6.2 Scribe and break recipe for 170μm thick Silicon chips

Parameter	Value
Scribe mode	On wafer

Scribe angle	37^{o}
Scribe force	50gm
Break type	Anvil
Air pressure	12.5psi
Ibar height	240μm

Following the backside metal deposition, the final step is to cleave the sample to form the input and output coupling facet. In comparison to III-V group materials, silicon is a harder material and therefore more challenging to cleave. Figures 6.3(a) and (b) present instances of less-than-ideal cleavage in silicon samples, highlighting the presence of unwanted features that can affect the subsequent hybrid integration with lasers. Figure 6.3(c) illustrates the desired cleaved surface. For samples with thicknesses around 170μm, our optimal scribe and break parameters are listed in Table 6.2.

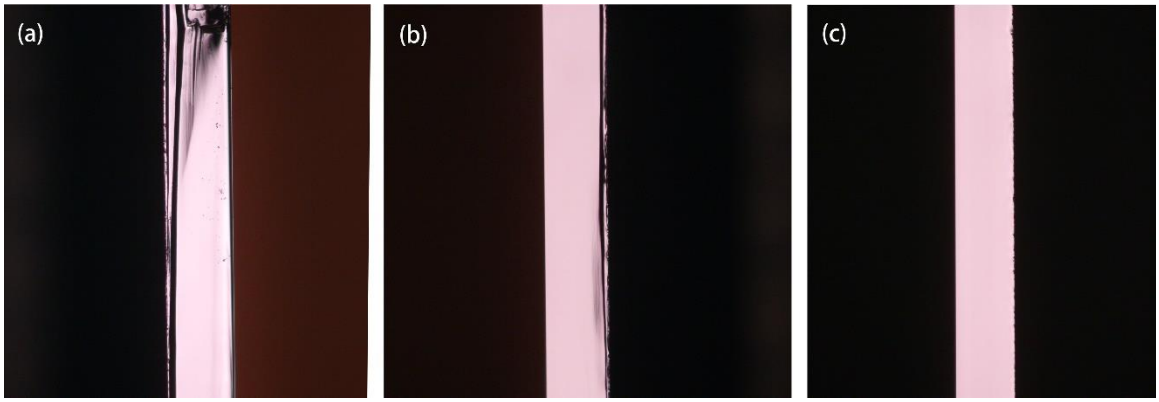

Figure 6.3 Microscope images of cleaved silicon facets

6.3 PIC chip design and characterization

6.3.1 Edge coupling

We use edge coupling method to realize the input and output coupling with the laser chip and lensed fiber. To enhance edge coupling efficiency, we utilize both regular

tapers and inversed tapers, as illustrated in Figure 6.4 (a) and (d), respectively. The regular taper features a horn-shaped design with a gradually increasing waveguide width to enlarge the mode size in the transverse direction while maintaining the mode size in the vertical direction. A typical mode profile at the end of a regular taper is depicted in Figure 6.4(b). In contrast, the inversed taper has a small tip at the end, allowing for the majority of mode to exist in the cladding layer in the form of evanescent waves, thereby expanding the mode size. The inversed taper can expand the mode size in both the vertical and transverse directions, as demonstrated in Figure 6.4(d).

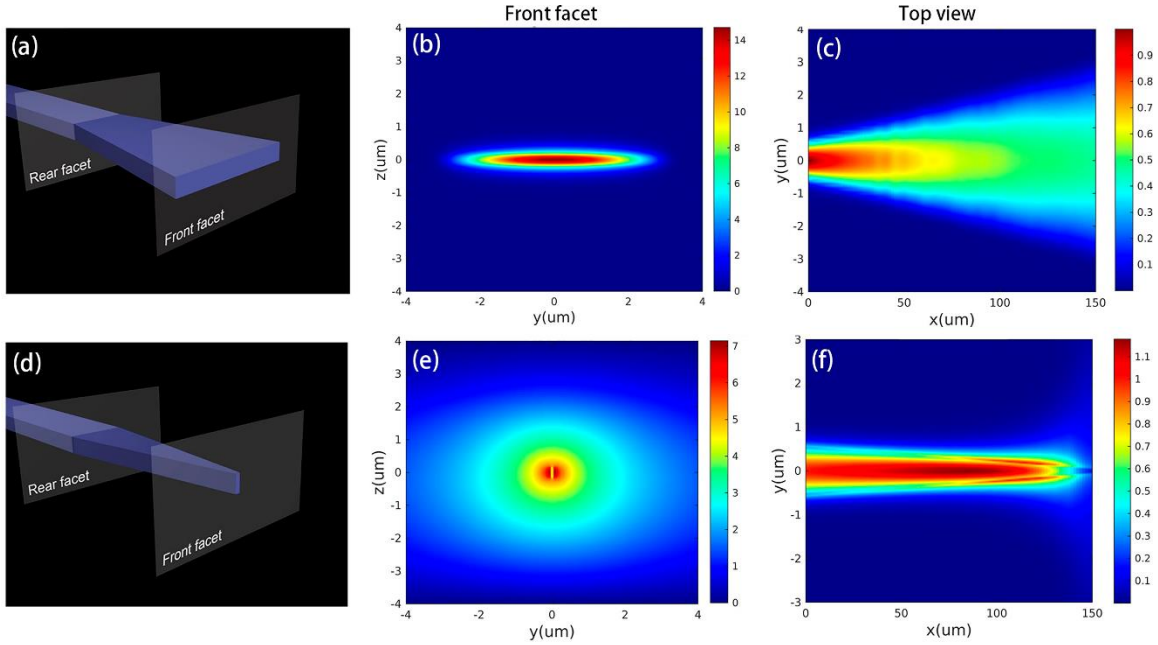

Figure 6.4 Schematic of a regular and an inverse taper with simulated mode profiles at the front facet and electric field distributions in the top view

For the input coupling terminal, we choose our ETAS-based RW laser with a 7μm wide ridge. We first simulate the power coupling efficiency as the taper end width changes, considering the overlap between the laser's fundamental mode and the mode at

the taper's output end. The simulations were conducted using Ansys Lumerical. The results, shown in Figure 6.5, indicate that for the regular/horn taper, the optimal taper end width is approximately 10μm, resulting in a coupling efficiency of 0.589 (-2.3dB). In the case of the inversed taper, the optimal taper end width is 0.12μm, with a coupling efficiency of 0.501 (-3dB). It's important to note that the etch depth of the laser ridge varies across the wafer during fabrication, and in addition, the actual lasing mode is affected by carrier-induced refractive index changes and thermal lens effects, which can impact the optimal taper width and coupling efficiency in practice.

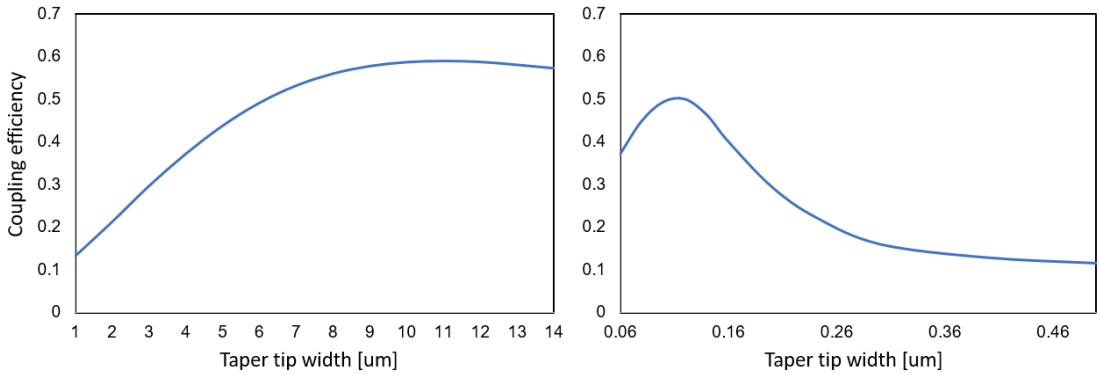

Figure 6.5 Evolution of power coupling efficiency for the overlap between the laser's fundamental mode and the mode at the taper's output end with varying taper end width. Simulation parameters: TE mode, RW laser ridge width 7μm, etch depth 1.1μm; Si_3N_4 core layer thickness 300nm, SiO_2 cover cladding thickness 2μm.

For the output coupling terminal, we utilize an AR-coated lensed fiber with a spot size (MFD $1/e^2$) of 2μm to collect the output from the PIC chips. We also simulate the power coupling efficiency for the overlap between the lensed fiber spot size mode and the mode at the taper's output end as a function of the taper end width. This simulation results are presented in Figure 6.6. It is found that the highest coupling efficiency, reaching 0.44

(-3.5dB), is achieved with a taper end width of 3μm in the case of a regular taper. Conversely, for the inverse taper, the maximum coupling efficiency is as high as 0.89 (-0.51dB) with a taper end width of 0.16μm.

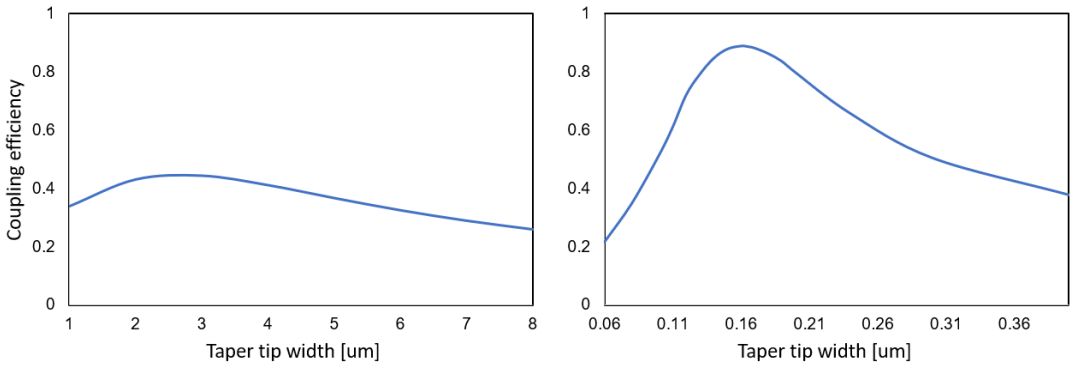

Figure 6.6 Evolution of power coupling efficiency for the overlap between the lensed fiber's spot size mode and the mode at the taper's output end with varying taper end width. Simulation parameters: TE mode, lensed fiber spot size MFD($1/e^2$) 2um; Si_3N_4 core layer thickness 300nm, SiO_2 cover cladding thickness 2μm.

Once the width of the taper tip end is established, the next step is to determine the length of the taper. If the taper is too short, it can result in coupling between the fundamental mode and higher-order modes during propagation, leading to a reduction in the transmission of the fundamental mode. To examine the impact of taper length on transmission, we will perform a transmission sweep simulation using the Ansys Lumerical eigenmode expansion (EME) solver. For the linear inverse taper, it needs a much longer taper length to obtain the transmission closed to 1. Curved inverse taper helps to shorten the taper length. The curved inverse taper can be parameterizing as follows:

$$
\begin{aligned}
w(x) &= \alpha\left(L - x\right)^m + w_2 \\
w(0) &= w_1, \\
w(L) &= w_2, \\
\alpha &= \left(w_1 - w_2\right)/L^m
\end{aligned}
\tag{6.1}
$$

where w_1 represents the end tip width of the inverse taper, and w_2 represents the width of the bus waveguide. In this case, the width of the inverse taper will be proportional to x to the power of exponent m. m =1 corresponds to a linear inverse taper. Figure 6.7 (a) and (b) respectively displays the taper shape for m = 0.5 and m = 2. Figure 6.7 (c) shows the simulated transmission sweep over the length of inverse taper for various values of m, which clearly demonstrates that, for an equivalent inverse taper length, a smaller value of m contributes to an enhanced transmission.

Table 6.3 summarizes the simulated and measured coupling loss between various taper designs and lensed fibers. In the coupling loss measurement setup shown in Figure 6.8, a lensed fiber is used to couple the output of a tunable laser, known for its power, into the tested taper. An optical power meter is then used to capture the laser power from the output end taper. The input and output ends are oriented in perpendicular facets, ensuring that the input laser does not affect the power reading on the output end optical power meter, thereby guaranteeing the accuracy of the results. The coupling loss obtained through this method encompasses the transmission loss in the waveguide, so the actual taper coupling loss should be slightly less than this value. The highest coupling efficiency is achieved by employing an inverted taper with a tip end of 160nm and a lensed fiber featuring a spot size of 2μm, resulting in a minimal coupling loss of approximately -2.1dB.

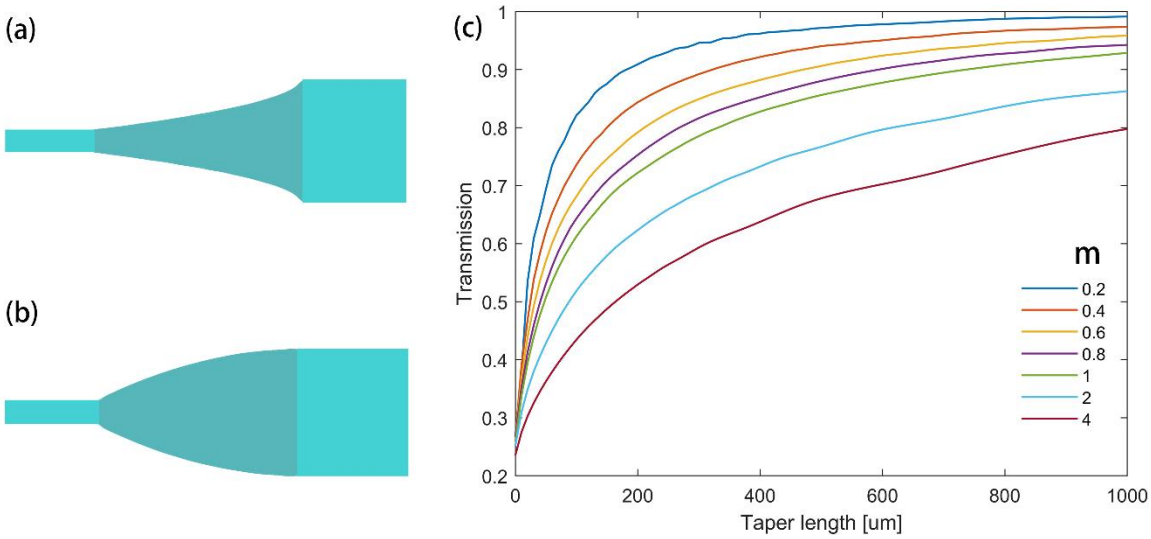

Figure 6.7 Curved inverse tapers for m = 0.5 (a) and m = 2 (b). (c) Transmission sweep over the length of inverse taper for various values of m (w_1 = 100nm, w_2 = 600nm, Si_3N_4 waveguide thickness 300nm).

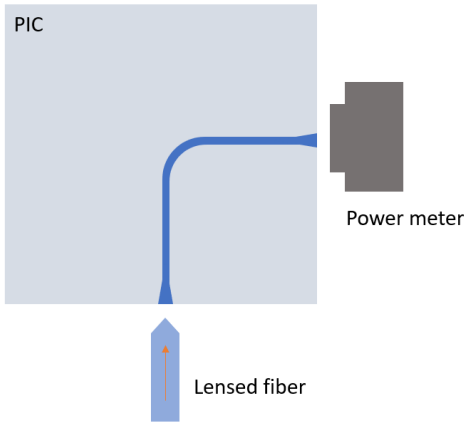

Figure 6.8 Experimental setup for coupling loss measurement between a taper and a lensed fiber

Table 6.3 Summary of simulated and measured coupling loss between various taper designs and lensed fibers

Taper end width [μm]	Lensed fiber spot size [μm]	Simulated coupling loss [dB]	Measured coupling loss [dB]
6	4.5	-6.65	-6.27
6	2	-4.87	-7.1
4	4.5	-7.09	-7.55
0.16	2	-0.51	-2.1
0.1	2	-2.68	-3

6.3.2 Microring resonator

In microring resonator design, our primary concerns revolve around the Free Spectral Range (FSR) and the loaded quality factor (Q_L). FSR can be determined using the expression, $FSR = \lambda^2 / \left(2\pi R n_g\right)$, where R represents the ring radius and n_g is the group index of the optical mode. A larger FSR, and consequently, a smaller ring radius, is desirable to achieve a broader wavelength tuning range. However, a smaller radius would lead to a reduction in the length of the micro heater positioned above the microring, which, in turn, would require higher voltage for achieving a 2π phase shift.

Q_L can be calculated by expression $Q_L = \omega_0 / \Delta\omega$, where ω_0 and $\Delta\omega$ respectively represents the resonance frequency and the linewidth of the resonance. Q_L is influenced by the intrinsic quality factor Q_i and the coupling quality factor Q_e. Q_i is associated with the total optical loss (absorption and scattering) within the resonator and the additional loss incurred by coupling region. Q_e is associated with the coupling efficiency to the bus

and the drop waveguides. Figure 6.9(a) depicts the simulated coupling efficiency as a function of the coupling gap for various ring radius, illustrating that when the coupling gap remains constant, a larger ring radius leads to a greater coupling efficiency.

The coupling efficiency is also influenced by the waveguide width, as a narrower waveguide width results in more evanescent waves in the cladding, leading to a larger overlap with the other coupling waveguide, and consequently, a higher coupling efficiency under the same coupling gap conditions. In Figure 6.9(b), the relationship between the coupling gap and ring radius required to achieve a coupling efficiency of 0.05 is depicted. Here, we consider two waveguide widths, 600nm (in blue) and 800nm (in red). As expected, when the ring radius remains constant, a narrower waveguide width necessitates a larger coupling gap to achieve the same coupling efficiency.

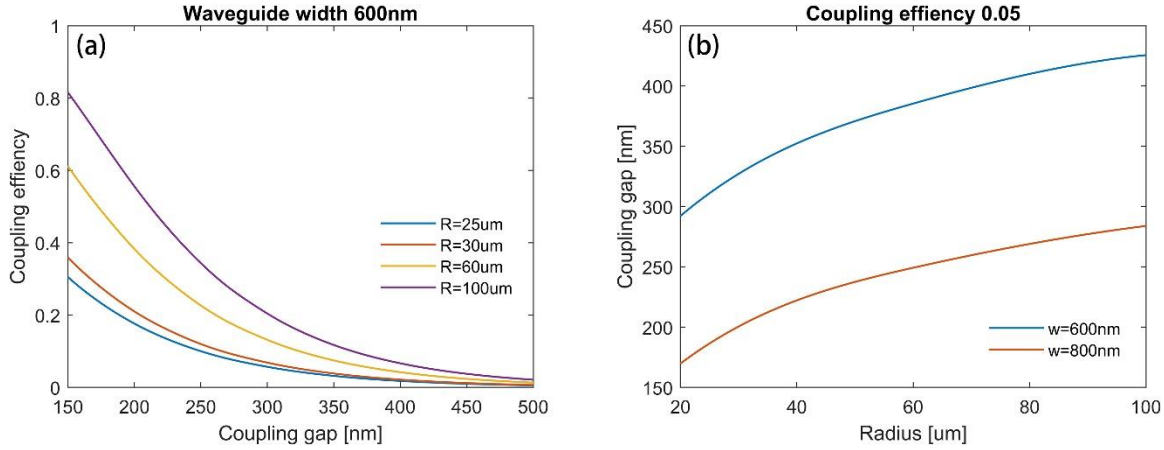

Figure 6.9 (a) Simulated coupling efficiency as a function of coupling gap for various ring radius (waveguide width is set to be 600nm) (b) The correlation between the coupling gap and ring radius required to achieve a coupling efficiency of 0.05, considering two different waveguide widths, 600nm (in blue) and 800nm (in red).

6.3.3 Loop mirror

Loop mirror is used at the drop port of the microring resonator to reflect part of the resonant light back towards the FP laser, resulting in self-injection locking. This loop mirror comprises a symmetrical 1 x 2 splitter with interconnected output ports, with multimode interference (MMI) couplers serving as the 1 x 2 splitters. The design of the MMI is carried out using the EME solver from Lumerical. Figure 6.10 shows the geometry of the designed MMI and the simulated power transmission for one of the output ports. The graph displays a peak transmission of approximately 50% at a wavelength around 970nm and a wide transmission band. Consequently, even if the wavelength of the FP laser shifts, there is only minimal loss introduced by the feedback loop mirror.

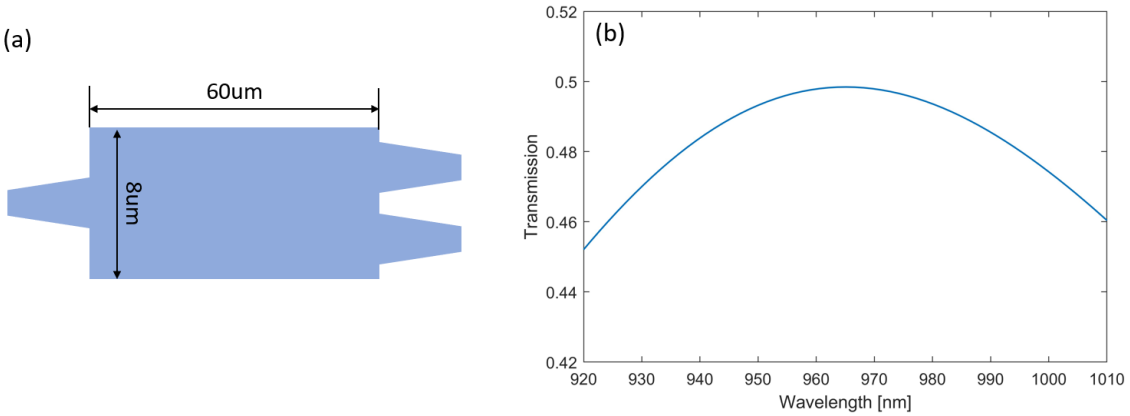

Figure 6.10 The geometry of the designed MMI and its simulated power transmission of one of the output ports.

6.3.4 Microheater

We employ microheaters to induce a phase shift in the bus waveguide and tune the resonance wavelength of the microring. The separation distance between the

microheaters and the Si_3N_4 waveguide layer is specifically set at 2μm. To simulate the thermally induced phase shift of the Si_3N_4 waveguide by the microheaters, we utilize the Heater and FDE solvers within the Ansys Lumerical software platform. The HEAT solver is employed to model the temperature distribution of the waveguide under various input power conditions. Subsequently, this temperature profile data is imported into the FDE solver to analyze the effective refractive index and phase shift as a function of the input power. In our simulation, the thermo-optic coefficient for Si_3N_4 and SiO_2 are set to 2.51e-5 1/K and 9.6e-6 1/K, respectively [106, 107]. Figure 6.11 illustrates the simulated phase shift for a 600μm long Si_3N_4 waveguide with varying widths, as a function of the input power. The results clearly demonstrate that microheaters with narrower widths require less power to achieve a 2π phase shift. Moreover, simulation results indicate that altering the length of the heater does not affect the power required to achieve a 2π phase shift. Nevertheless, extending the heater's length can reduce the temperature change and current required for a 2π phase shift.

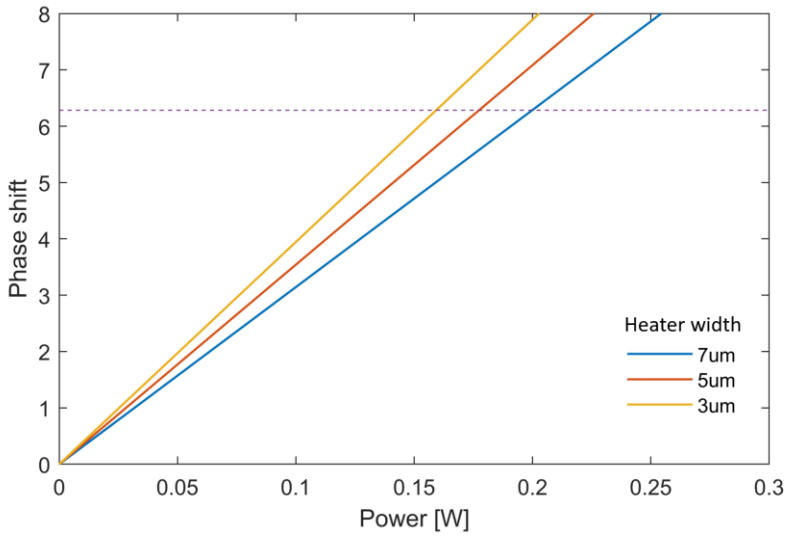

Figure 6.11 Simulated phase shift in relation to input power for a Si_3N_4 waveguide with different widths. Heater length is assumed to be 600μm.

Figure 6.12 (a) shows the measured transmission spectra of the microring under different levels of voltage applied to the microheater, revealing a redshift in the resonance wavelength as the applied voltage/power is incrementally increased. The relationship between the extracted resonance wavelength and the applied voltage is shown in Figure 6.12(b), indicating the attainment of a 2π phase shift at ~10.7V. Considering the total measured resistance is around 350Ω, it can be calculated that the 2π phase shift power is 0.32W.

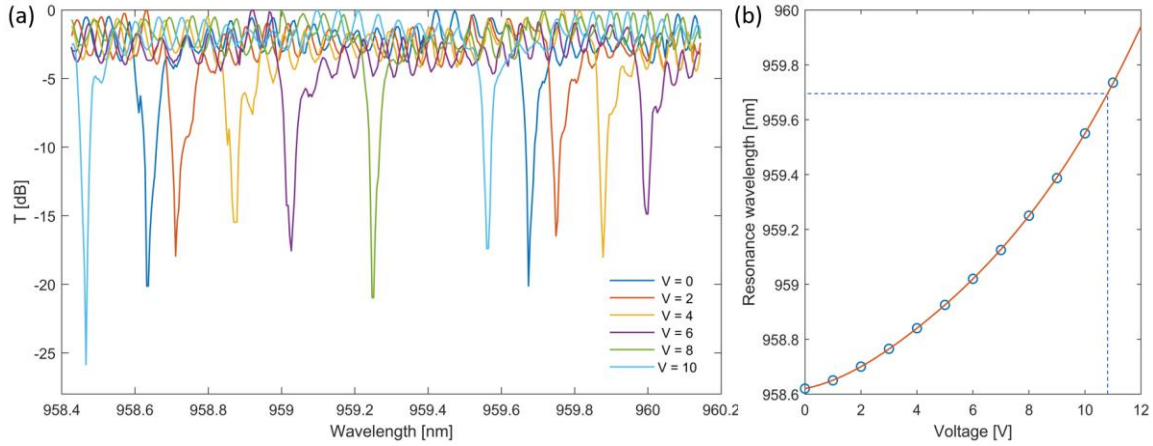

Figure 6.12 (a) Measured transmission spectra of the microring at various applied voltages on the microheater. (b) The relationship between the resonance wavelength shift and the applied voltage. Notably, the microring has a radius of 40μm, the microheater's length and width is 335μm and 7μm, respectively.

6.4 Experimental results of self-injection locking lasers

Figures 6.13 depict the experimental setup, showing that a FP laser diode chip is butt-coupled to a PIC chip and the output radiation is collected by a lensed fiber. Both the laser and PIC chip are securely mounted on a water-cooled stage. The positioning of the laser chip is controlled using the Thorlabs Nanomax stage to manage its xyz coordinates, while the PIC chip is placed on a Thorlabs Tip, Tilt, and Rotation Stage (TTR001) to control its θ_x, θ_y, and θ_z angles. This setup allows for improved alignment of the two chips, thereby enhancing coupling efficiency. The FP laser is p-side up mounted on C mount. The PIC chip is mounted onto a copper block, with a specifically designed PCB positioned on top to facilitate the wiring of the microheater electrodes.

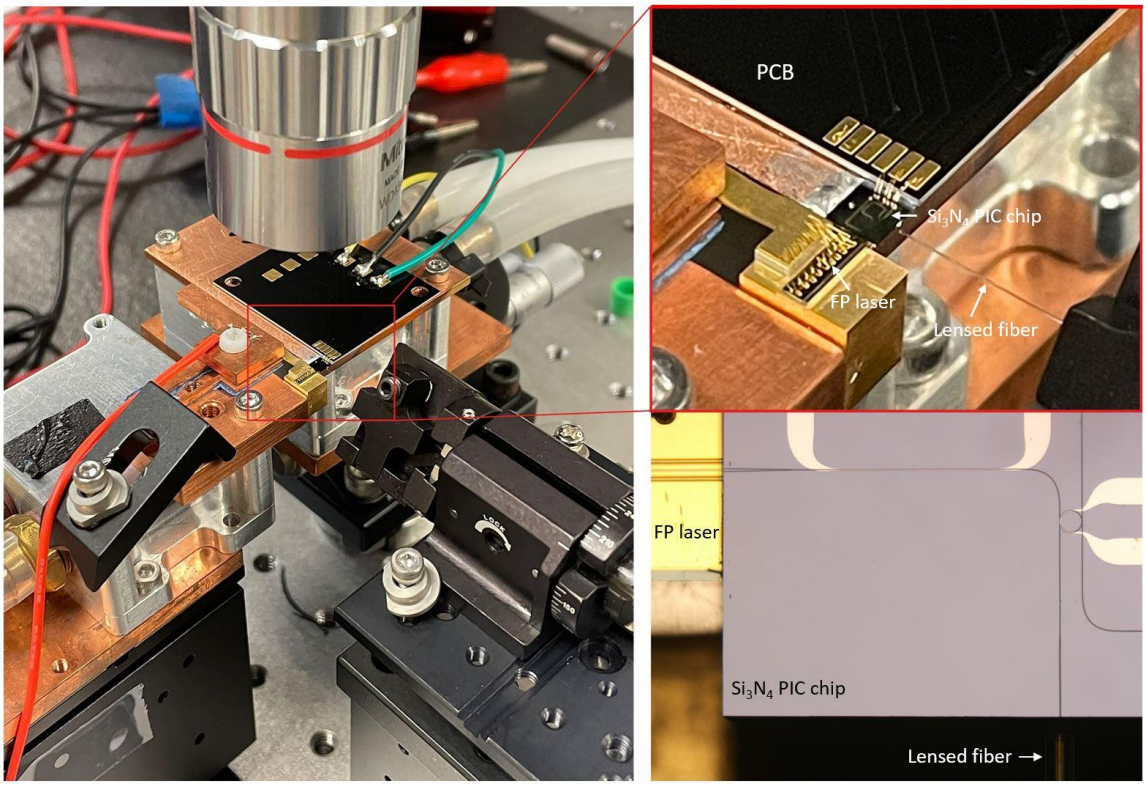

Figure 6.13 Photo of the experimental setup of self-injection locking laser

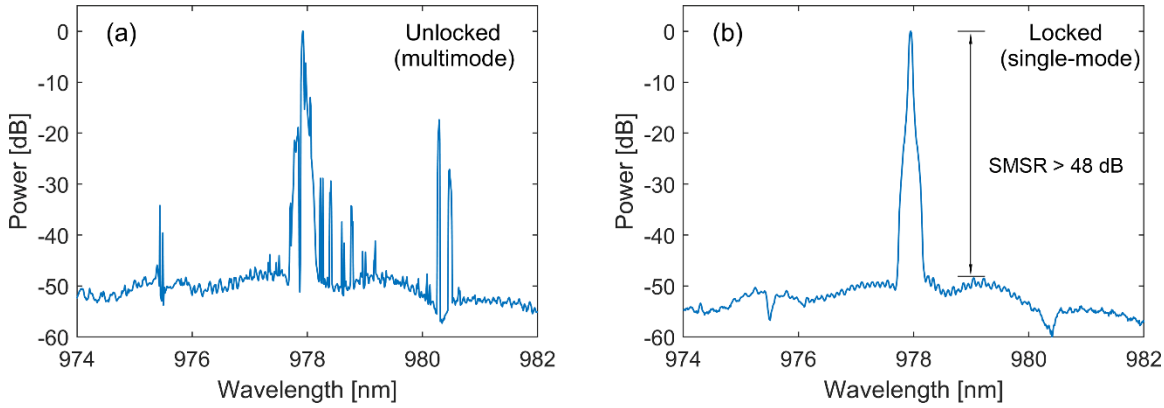

Figure 6.14 The measured optical spectra of the hybrid system in the unlocked (a) and locked (b) regime. The optical spectra are measured using optical spectrum analyzer with resolution of 0.05nm

When the resonance of the microring is detuned from the modes of the FP laser

diode, or when the phase of the reflected light fails to facilitate constructive interference with the FP mode within the FP laser, the hybrid system operates in the unlocked state, resulting in the emission of unstable multiple lasing modes, as observed in Figure 6.14(a). When the resonance of microring aligns with a mode of FP laser, allowing the feedback loop to reflect a portion of the light back into the laser, and the phase of reflected light is further adjusted to constructively interfere with the light inside the laser, self-injection-locking occurs. In the locked state, the reflected light functions as an effective additional gain for the chosen wavelength, leading the longitudinal mode at that wavelength to win in mode competition. Consequently, the optical power distributed among other longitudinal modes collapse into the selected mode. Illustrated in Figure 6.14(b) of the optical spectrum of a locked hybrid laser, all the longitudinal modes are converted into a single-frequency, narrow-linewidth lasing mode with a high Signal-to-Mode Suppression Ratio (SMSR) exceeding 48dB. Figure 6.15 shows the microscopic image of the PIC chip when the hybrid laser is locked. We can observe strong scattered light around the ring and the loop mirror using IR CCD camera. In the locked state, the laser output maintains a stable spot of light. Conversely, when it is not locked, the feedback light from the PIC chip perturbs the laser dynamics, causing oscillations in laser output, which are observed as flickering spots of light in the CCD camera.

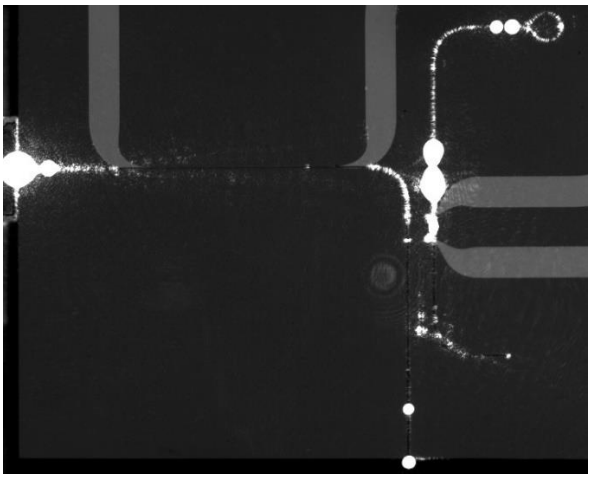

Figure 6.15 Microscope image of the PIC chip when the FP laser is self-injection locked

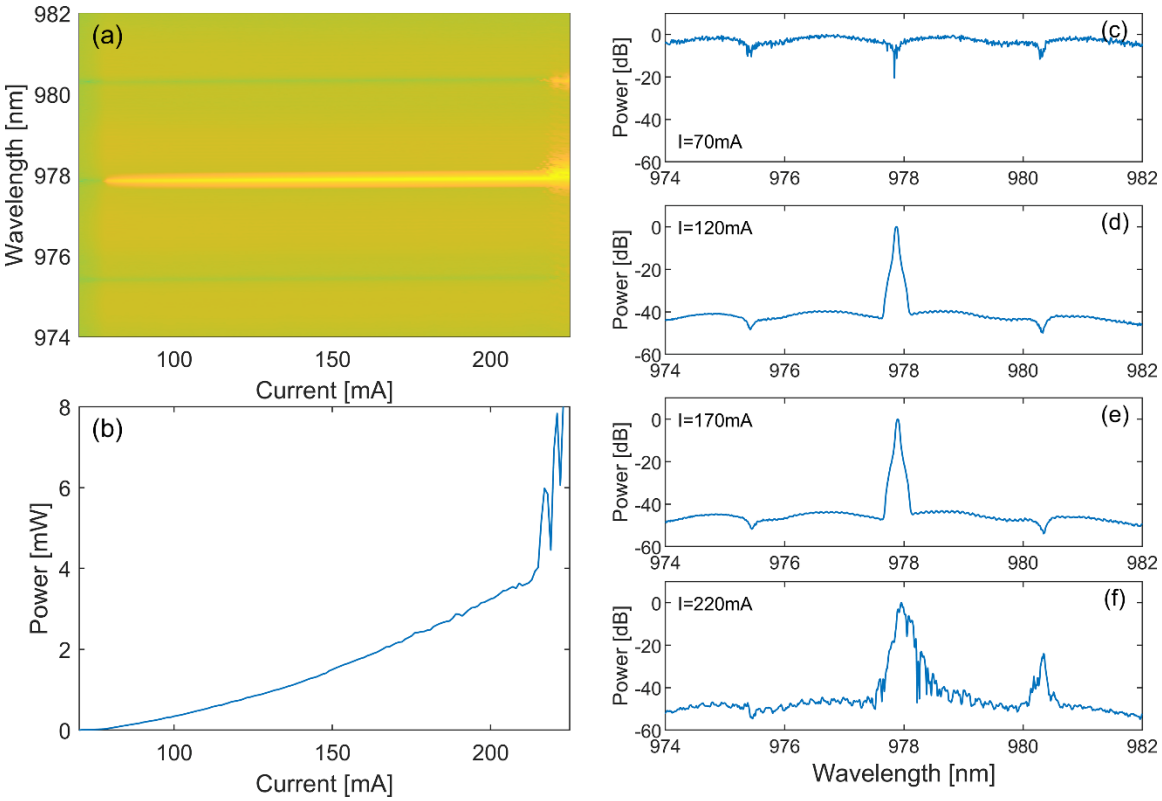

Figure 6.16 Spectrogram (a) and fiber coupled output power (b) of the hybrid laser while linearly sweeping the injection current of the FP diode laser.

For an independent FP laser diode, its lasing wavelength changes with variations in injection current and operating temperature. However, in the case of a self-injection locking laser, when it reaches the locked regime, the frequency-pulling effect allows its lasing wavelength to lock onto the microring resonance wavelength. Therefore, within a certain range, the lasing wavelength can remain constant while altering the injection current. This frequency-pulling characteristic is unique to self-injection-locking lasers, and ECLs do not possess this feature. Figure 6.16 (a) and (b) respectively plots the spectrogram and the fiber coupled output power of our hybrid system when linearly sweeping the injection current of the FP laser. Below threshold, as shown in Figure 16 (c), the optical gain is insufficient to induce lasing, resulting in incoherent light emitted through spontaneous emission. The spectrum displays the gain profile shape of the FP laser, with transmission dips occurring at the resonance wavelengths of the microring. After reaching the threshold current, the hybrid laser maintains in the locked state of single-mode operation across a wide current range up to approximately 210mA. Figures 6.16 (d) and (e) depict its spectra at currents of 120mA and 170mA, respectively, revealing a single-frequency output with the wavelength fixed at ~977.8nm. Additionally, it is noticeable that in the locked state, the power steadily rises with increasing current. At 210mA, it provides a fiber-coupled single-frequency output of 3.5mW. As the current is further increased, the locked state is broken, causing the laser to emit with multimode frequencies and the power to exhibit oscillations. With careful adjustments to the phase of the feedback light in real-time, the hybrid laser can be restored to a locked state at higher levels of current injection.

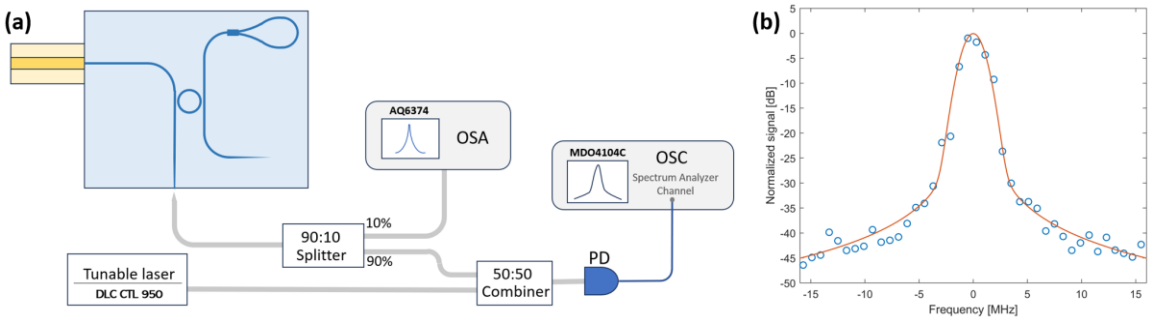

Figure 6.17 (a) Experimental setup for the linewidth measurement of the self-injection locking hybrid laser. (b) Heterodyne beat signal between the self-injection-locking hybrid laser and the narrow-linewidth reference laser

We utilize the heterodyne beat note measurement technique to evaluate the linewidths of our self-injection locking hybrid laser. In the heterodyne measurement, the laser signal under examination is mixed with a reference laser incoherent with the former. The resulting heterodyne beat signal's power spectral density (PSD) is then measured to analyze the linewidth of the laser under examination. As we know, the mixed signal of two incoherent lasers, each exhibiting a Lorentzian line shape, maintains a Lorentzian line shape. The power spectral density (PSD) of the beat notes can be expressed as [108]

$$s(\nu) = \frac{\Delta\nu}{2\pi\left[\left(\nu-\nu_b\right)^2+\left(\Delta\nu/2\right)^2\right]} \tag{6.1}$$

where $\Delta\nu = \Delta\nu_t + \Delta\nu_r$ represents the total linewidth, comprised of the linewidths of the tested laser (ν_t) and the reference laser (ν_r). ν_b denotes the center frequency of the beat notes, that is, the difference between the lasing frequencies of the test and reference lasers.

Figure 6.17 (a) illustrates our measurement setup, which utilizes a commercial narrow-linewidth tunable laser (Topica DLC CTL 950) to act as the reference laser. The

mixed signal of the tunable laser and the hybrid laser is received by a photodetector (PD) and transmitted to the spectrum analyzer channel of the oscilloscope (OSC). An optical spectrum analyzer (OSA) is used to monitor the lasing wavelength of the hybrid laser. The lasing wavelength of the tunable laser is finely adjusted with a slight detuning relative to that of the hybrid laser, ensuring that the beat note signal falls within the bandwidth of the spectrum analyzer channel.

The lineshape of the measured heterodyne beat signal reflects the frequency noise spectral density in relation to the reference laser. This noise includes both white noise, and 1/f (flicker) noise [109]. The white noise defines the intrinsic linewidth and yields a Lorentzian lineshape spectrum. The flicker and technical noise depend on, for example, the acquisition time of the electrical-signal spectral analyzer, as well as the stability of current, power and temperature controller, contributing to a Gaussian lineshape spectrum. Therefore, the measured beat signal spectrum exhibits the Voigt profile [110, 111], which is essentially a convolution of a Lorentzian spectrum ($L(v)$) with a Gaussian spectrum ($G(v)$), that is:

$$V(v) = \int_{-\infty}^{+\infty} G(v';\sigma) L(v - v';\psi)\, dv' \tag{6.2}$$

$$G(v;\sigma) = \frac{\exp^{-v^2/2\sigma^2}}{\sigma\sqrt{2\pi}} \tag{6.3}$$

$$L(v;\psi) = \frac{\gamma}{\pi\left(v^2 + \psi^2\right)} \tag{6.4}$$

where v indicates the frequency shift with respect to the center of the beat signal. The FWHM of the Gaussian lineshape is $\Delta v_G = 2\sigma$ and for the Lorentzian, $\Delta v_L = 2\psi$. On the

wings of the beat profile, the signal is primarily influenced by the white noise parameterized by ψ. Conversely, in the central area of the beat profile, the signal is additionally affected by flicker and technical noise scaled by σ. Figure 6.17(b) shows the measured heterodyne beat signal (blue circles) between the self-injection-locking laser and the reference laser and its Voigt fitting (red line) with $\Delta\nu_L$ = 25 kHz and $\Delta\nu_G$ = 1.5MHz. The Lorentzian linewidth of 25 kHz should be the sum of the intrinsic linewidth of the commercial tunable laser and the self-injection-locking laser. Despite lacking precise knowledge of the intrinsic linewidth value of the commercial reference laser, we can infer that the self-injection-locking laser possesses an intrinsic linewidth less than 25kHz. However, the Gaussian linewidth is relatively high, prompting the need for further investigation to reduce flicker and technical noise levels.

6.5 Conclusion

In this chapter, we demonstrate an on-chip self-injection locking laser by hybrid integration of our ridge waveguide FP laser with a Si_3N_4 PIC chip. This integration has successfully yielded a stable narrow-linewidth single-frequency laser output with fiber-coupled power of up to 3.5mW and an impressive SMSR exceeding 48dB. Heterodyne beat note measurement and Voigt fitting shows the self-injection locking laser has an intrinsic linewidth smaller than 25kHz. Further optimization of the mode matching and phase control would allow more high power on chip laser output, and smaller effective linewidth. The narrow-linewidth single-frequency hybrid laser requires only a FP laser, eliminating the necessity for an RSOA with low AR coating and a single-frequency DFB

laser. Our work showcases a promising strategy for realizing a fully integrated, highly coherent, high-power on-chip laser source.

Chapter 7

CONCLUSION

In summary, this thesis has primarily delved into the intricacies of designing, fabricating, and characterizing advanced high-power single-mode edge-emitting diode lasers with a lasing wavelength of 9xx nm.

Initially, the focus is on exploring strategies for designing laser epitaxial structures aiming at both high power output and efficiency. Through the introduction of a semi-analytical calculation method, we propose an optimization approach for the ETAS epitaxial structure, effectively accounting for LSHB and TPA effects. The calculated results underscored the significance of maintaining a relatively large confinement, approximately 0.6%, to sustain optimal performance across varying injection currents and cavity lengths for ETAS-based broad area lasers. The optimized epitaxial structure serves as the foundation for subsequent endeavors in developing high-power high-efficiency single-mode lasers.

Subsequently, we demonstrate high-power, high-efficiency RW lasers utilizing the optimized ETAS epitaxial structure. The 7μm-wide, 4mm-long RW laser, fabricated with both AR and HR coatings and mounted p-side up on a C-mount, exhibits kink-free output and near-Gaussian far-field profiles, achieving a maximum power exceeding 1.6W

under CW operation mode. At a current of 1.06A and output power of 1W, it reaches its peak efficiency of 62%. Remarkably, efficiency maintains a high level, registering at 60.2% even at 1.6A and 1.52W. Additionally, we fabricate 5μm-wide RW lasers using an enhanced epitaxial structure with reduced aluminum content in the p-cladding layer. These 5μm-wide, 5mm-long RW lasers demonstrate kink-free output up to 1W, boasting a high efficiency of 59.3%. Notably, the measured M^2 value consistently maintains close to 1, proving stable near-diffractive limit single-mode emission. By passivating the laser facets and applying AR/HR coatings and p-side down bonding, we anticipate that this batch of lasers can achieve higher single-mode output power.

We further present a novel TRW structure grounded in the unbroken SUSY principle, facilitating high-power single-transverse-mode operation with a larger emission aperture. This design integrates a pair of lossy auxiliary waveguides to suppress unwanted higher-order modes within the laser cavity. Through precise engineering of the TRW structural parameters, we achieve significant modal discrimination, ensuring stable single-mode lasing. Experimental results demonstrate near-diffraction-limited output in the proposed TRW laser, validating the efficacy of the mode filtering mechanism. This proposed TRW design offers several advantages: it enhances mode discrimination without affecting the fundamental mode, maintains stable single-mode operation at high injection currents by reducing susceptibility to carrier-induced index suppression, imposes no specific requirements on epitaxial structure, and is compatible with conventional RW laser fabrication techniques, facilitating cost-effective mass production. To further enhance mode discrimination, we propose the incorporation of trapezoidal

deep-etched trenches in the auxiliary waveguide. These trenches effectively convert guided modes into leaky modes, increasing propagation loss for undesired higher-order modes and promoting more stable single-mode operation at higher power outputs. Currently, we are in the process of fabricating TRW lasers with trapezoidal trenches, with the expectation of much better single-mode performance.

Finally, we achieve hybrid integration of our RW laser with a Si_3N_4 nitride PIC chip using the self-injection locking technique, resulting in a narrow-linewidth single-frequency on-chip laser source. Our experiments demonstrate stable laser output characterized by a fiber-coupled power of up to 3.5mW, SMSR exceeding 48dB, and an intrinsic linewidth smaller than 25kHz. The intrinsic linewidth is determined via heterodyne beat note technique, utilizing a commercial narrow-linewidth tunable laser as a reference. However, as the intrinsic linewidth of the commercial laser remains uncertain, this measurement provides only an estimate of the possible maximum intrinsic linewidth of our self-injection locking laser. Future research will involve self-heterodyne and phase noise measurements to provide a more precise evaluation of the linewidth. Additionally, we will investigate further into the flicker and technical noise of our current setup. Currently, the laser and PIC are mounted on a transform stage, leading to variable relative positions. To address this, we plan to utilize epoxy and our new active alignment machine, ficonTEC A300, to secure their relative position and ensure a more stable narrow-linewidth output.

BIBLIOGRAPHY

[1] Diehl, R.D., *High-power diode lasers: fundamentals, technology, applications*. Vol. 78. 2000: Springer Science & Business Media.

[2] Gmachl, C., et al., *Ultra-broadband semiconductor laser*. Nature, 2002. **415**(6874): p. 883-887.

[3] Li, L., *The advances and characteristics of high-power diode laser materials processing.* Optics and lasers in engineering, 2000. **34**(4-6): p. 231-253.

[4] Fritsche, H., et al. *High brightness direct diode laser with kW output power*. in *High-Power Diode Laser Technology and Applications XII*. 2014. SPIE.

[5] Kruschke, B., et al. *Beam combining techniques for high-power high-brightness diode lasers*. in *Components and Packaging for Laser Systems*. 2015. SPIE.

[6] Haas, M., et al., *Beam quality deterioration in dense wavelength beam-combined broad-area diode lasers.* IEEE Journal of Quantum Electronics, 2017. **53**(3): p. 1-11.

[7] Herzog, W., B. Goldberg, and M. Unlu, *Beam steering in narrow-stripe high-power 980-nm laser diodes.* IEEE Photonics Technology Letters, 2000. **12**(12): p. 1604-1606.

[8] Achtenhagen, M., A. Hardy, and C.S. Harder, *Lateral mode discrimination and self-stabilization in ridge waveguide laser diodes.* IEEE photonics technology letters, 2006. **18**(3): p. 526-528.

[9] Chan, P.K., et al., *Temperature mapping and thermal lensing in large-mode, high-power laser diodes.* Applied physics letters, 2006. **89**(20).

[10] Wenzel, H., M. Dallmer, and G. Erbert, *Thermal lensing in high-power ridge-waveguide lasers.* Optical and quantum electronics, 2008. **40**: p. 379-384.

[11] Kringlebotn, J., et al., *Efficient diode-pumped single-frequency erbium: ytterbium fiber laser.* IEEE photonics technology letters, 1993. **5**(10): p. 1162-1164.

[12] Rabinovich, W.S., et al. *InGaAs multiple quantum well modulating retro-reflector for free-space optical communications*. in *Free-Space Laser Communication and Laser Imaging*. 2002. SPIE.

[13] Durry, G., et al., *Shot-noise-limited dual-beam detector for atmospheric trace-gas monitoring with near-infrared diode lasers.* Applied optics, 2000. **39**(30): p. 5609-5619.

[14] Bachmann, F., *Industrial applications of high power diode lasers in materials processing.* Applied surface science, 2003. **208**: p. 125-136.

[15] Strohmaier, S., et al., *High-power, high-brightness direct-diode lasers.* Optics and Photonics News, 2010. **21**(10): p. 24-29.

[16] Gao, Y., et al., *High-Power, Narrow-Linewidth, Miniaturized Silicon Photonic Tunable Laser With Accurate Frequency Control.* Journal of Lightwave Technology, 2020. **38**(2): p. 265-271.

[17] Guan, H., et al., *Widely-tunable, narrow-linewidth III-V/silicon hybrid external-cavity laser for coherent communication.* Optics Express, 2018. **26**(7): p. 7920-7933.
[18] Hu, H. and L.K. Oxenløwe, *Chip-based optical frequency combs for high-capacity optical communications.* Nanophotonics, 2021. **10**(5): p. 1367-1385.
[19] Zhou, Z., et al., *Prospects and applications of on-chip lasers.* eLight, 2023. **3**(1): p. 1.
[20] Alkhazraji, E., et al., *Linewidth narrowing in self-injection-locked on-chip lasers.* Light: Science & Applications, 2023. **12**(1): p. 162.
[21] Xiang, C., P.A. Morton, and J.E. Bowers, *Ultra-narrow linewidth laser based on a semiconductor gain chip and extended Si3N4 Bragg grating.* Optics Letters, 2019. **44**(15): p. 3825-3828.
[22] Agrawal, G.P. and N.K. Dutta, *Semiconductor lasers*. 2013: Springer Science & Business Media.
[23] Ohtsubo, J. and J. Ohtsubo, *Semiconductor lasers and theory*. 2017: Springer.
[24] Chow, W.W. and S.W. Koch, *Semiconductor-laser fundamentals: physics of the gain materials*. 1999: Springer Science & Business Media.
[25] Bachmann, F., P. Loosen, and R. Poprawe, *High power diode lasers: technology and applications*. Vol. 128. 2007: Springer.
[26] Piprek, J., *Semiconductor optoelectronic devices: introduction to physics and simulation*. 2013: Elsevier.
[27] Coldren, L.A., S.W. Corzine, and M.L. Mashanovitch, *Diode lasers and photonic integrated circuits*. 2012: John Wiley & Sons.
[28] Marko, I.P., et al., *Effect of non‐pinned carrier density above threshold in InAs quantum dot and quantum dash lasers.* IET Optoelectronics, 2014. **8**(2): p. 88-93.
[29] Kaul, T., et al., *Impact of carrier nonpinning effect on thermal power saturation in GaAs-based high power diode lasers.* IEEE Journal of Selected Topics in Quantum Electronics, 2019. **25**(6): p. 1-10.
[30] Crump, P., et al., *Efficient high-power laser diodes.* IEEE Journal of Selected Topics in Quantum Electronics, 2013. **19**(4): p. 1501211-1501211.
[31] Hasler, K., et al., *Comparative theoretical and experimental studies of two designs of high-power diode lasers.* Semiconductor Science and Technology, 2014. **29**(4): p. 045010.
[32] Kaul, T., et al. *Studies of limitations to peak power and efficiency in diode lasers using extreme-double-asymmetric vertical designs*. in *2016 International Semiconductor Laser Conference (ISLC)*. 2016. IEEE.
[33] Yamagata, Y., et al. *915nm high-power broad area laser diodes with ultra-small optical confinement based on Asymmetric Decoupled Confinement Heterostructure (ADCH)*. in *High-Power Diode Laser Technology and Applications Xiii*. 2015. SPIE.
[34] Kaul, T., et al. *Extreme triple asymmetric (ETAS) epitaxial designs for increased efficiency at high powers in 9xx-nm diode lasers*. in *High-Power Diode Laser Technology XVI*. 2018. SPIE.

[35] Boni, A., et al. *Efficiency optimization of high-power GaAs lasers by balancing confinement and threshold*. in *2021 27th International Semiconductor Laser Conference (ISLC)*. 2021. IEEE.
[36] Boni, A., et al. *Epitaxial design progress for high power, efficiency, and brightness in 970 nm broad area lasers*. in *High-Power Diode Laser Technology XIX*. 2021. SPIE.
[37] Crump, P., et al. *Increased conversion efficiency at 800 w continuous wave output from single 1-cm diode laser bars at 940 nm*. in *The European Conference on Lasers and Electro-Optics*. 2021. Optica Publishing Group.
[38] Rinner, F., et al., *Longitudinal carrier density measurement of high power broad area laser diodes.* Applied physics letters, 2002. **80**(1): p. 19-21.
[39] Wenzel, H., et al., *Theoretical and experimental investigations of the limits to the maximum output power of laser diodes.* New Journal of Physics, 2010. **12**(8): p. 085007.
[40] Chen, Z., et al. *Performance limitation and mitigation of longitudinal spatial hole burning in high-power diode lasers*. in *Novel In-Plane Semiconductor Lasers XI*. 2012. SPIE.
[41] Piprek, J. and Z.-M. Li, *What causes the pulse power saturation of GaAs-based broad-area lasers?* IEEE Photonics Technology Letters, 2018. **30**(10): p. 963-966.
[42] Avrutin, E.A. and B.S. Ryvkin, *Effect of spatial hole burning on output characteristics of high power edge emitting semiconductor lasers: A universal analytical estimate and numerical analysis.* Journal of Applied Physics, 2019. **125**(2).
[43] Dogan, M., et al. *Two photon absorption in high power broad area laser diodes*. in *High-Power Diode Laser Technology and Applications XII*. 2014. SPIE.
[44] Demir, A., et al., *Semiconductor laser power enhancement by control of gain and power profiles.* IEEE Photonics Technology Letters, 2015. **27**(20): p. 2178-2181.
[45] Avrutin, E. and B. Ryvkin, *Theory of direct and indirect effect of two-photon absorption on nonlinear optical losses in high power semiconductor lasers.* Semiconductor science and technology, 2016. **32**(1): p. 015004.
[46] Arslan, S., et al. *Approaches for higher power in GaAs-based broad area diode lasers*. in *2019 IEEE High Power Diode Lasers and Systems Conference (HPD)*. 2019. IEEE.
[47] Kaul, T., et al., *Suppressed power saturation due to optimized optical confinement in 9xx nm high-power diode lasers that use extreme double asymmetric vertical designs.* Semiconductor Science and technology, 2018. **33**(3): p. 035005.
[48] Wilson, J. *Thermal conductivity of common alloys in electronics packaging*. 2007; Available from: https://www.electronics-cooling.com/2007/02/thermal-conductivity-of-common-alloys-inelectronics-packaging.
[49] Adachi, S., *Properties of semiconductor alloys: group-IV, III-V and II-VI semiconductors*. 2009: John Wiley & Sons.

[50] Jiang, G., et al., *Understanding lasers, laser diodes, laser diode packaging and their relationship to tungsten copper*. Advanced Thermal Management Materials, 2013: p. 123-140.
[51] Liu, X., et al. *Packaging and performance of high power semiconductor lasers of high heat flux up to 2000 W/cm/sup 2*. in *Proceedings Electronic Components and Technology, 2005. ECTC'05.* 2005. IEEE.
[52] Hassan, M.R.A., et al., *Cavity-based mid-IR fiber gas laser pumped by a diode laser*. Optica, 2016. **3**(3): p. 218-221.
[53] Wenzel, H., et al. *High pulse power wavelength stabilized 905 nm laser bars for automotive LiDAR*. in *2019 IEEE High Power Diode Lasers and Systems Conference (HPD)*. 2019. IEEE.
[54] Pietrzak, A., et al. *Development of highly efficient laser diodes emitting around 1060nm for medical and industrial applications*. in *High-Power Diode Laser Technology XVII*. 2019. SPIE.
[55] Schneider, S., et al. *Power scaling of kW-diode lasers optimized for material processing applications*. in *High-Power Diode Laser Technology and Applications XIII*. 2015. SPIE.
[56] Brauch, U., P. Loosen, and H. Opower, *High-power diode lasers for direct applications*, in *High-Power Diode Lasers: Fundamentals, Technology, Applications: With Contributions by Numerous Experts*. 2000, Springer. p. 303-368.
[57] Agrawal, G.P., *Lateral‐mode analysis of gain‐guided and index‐guided semiconductor‐laser arrays.* Journal of applied physics, 1985. **58**(8): p. 2922-2931.
[58] Bartolo, R., et al., *Mid-infrared angled-grating distributed feedback laser.* Applied Physics Letters, 2000. **76**(22): p. 3164-3166.
[59] Zhu, L., et al., *Electrically-pumped, broad-area, single-mode photonic crystal lasers.* Optics Express, 2007. **15**(10): p. 5966-5975.
[60] Kanskar, M., et al. *Performace and reliability of ARROW single-mode and 100-um laser diode and the use of NAM in Al-free lasers*. in *Novel In-Plane Semiconductor Lasers II*. 2003. SPIE.
[61] Hirose, K., et al., *Watt-class high-power, high-beam-quality photonic-crystal lasers.* Nature photonics, 2014. **8**(5): p. 406-411.
[62] Yoshida, M., et al., *Double-lattice photonic-crystal resonators enabling high-brightness semiconductor lasers with symmetric narrow-divergence beams.* Nature materials, 2019. **18**(2): p. 121-128.
[63] Song, A.Y., et al., *Controllable finite ultra-narrow quality-factor peak in a perturbed Dirac-cone band structure of a photonic-crystal slab.* Applied Physics Letters, 2021. **119**(3).
[64] Hodaei, H., et al., *Single mode lasing in transversely multi‐moded PT‐symmetric microring resonators.* Laser & Photonics Reviews, 2016. **10**(3): p. 494-499.

[65] Hayenga, W.E., et al., *Electrically pumped microring parity-time-symmetric lasers.* Proceedings of the IEEE, 2019. **108**(5): p. 827-836.
[66] El-Ganainy, R., et al., *Supersymmetric laser arrays.* Physical Review A, 2015. **92**(3): p. 033818.
[67] Hokmabadi, M.P., et al., *Supersymmetric laser arrays.* Science, 2019. **363**(6427): p. 623-626.
[68] Midya, B., et al., *Supersymmetric microring laser arrays.* Photonics Research, 2019. **7**(3): p. 363-367.
[69] Qiao, X., et al., *Higher-dimensional supersymmetric microlaser arrays.* Science, 2021. **372**(6540): p. 403-408.
[70] Shankar, R., *Principles of quantum mechanics*. 2012: Springer Science & Business Media.
[71] Bender, C.M. and S. Boettcher, *Real spectra in non-Hermitian Hamiltonians having P T symmetry.* Physical review letters, 1998. **80**(24): p. 5243.
[72] Makris, K.G., et al., *Beam dynamics in P T symmetric optical lattices.* Physical Review Letters, 2008. **100**(10): p. 103904.
[73] Regensburger, A., et al., *Parity–time synthetic photonic lattices.* Nature, 2012. **488**(7410): p. 167-171.
[74] Guo, A., et al., *Observation of P T-symmetry breaking in complex optical potentials.* Physical review letters, 2009. **103**(9): p. 093902.
[75] Rüter, C.E., et al., *Observation of parity–time symmetry in optics.* Nature physics, 2010. **6**(3): p. 192-195.
[76] Cooper, F., A. Khare, and U. Sukhatme, *Supersymmetry and quantum mechanics.* Physics Reports, 1995. **251**(5-6): p. 267-385.
[77] Sukumar, C. *Supersymmetric quantum mechanics and its applications*. in *AIP Conference Proceedings*. 2004. American Institute of Physics.
[78] Sourlas, N., *Introduction to supersymmetry in condensed matter physics.* Physica D: Nonlinear Phenomena, 1985. **15**(1-2): p. 115-122.
[79] Miri, M.-A., et al., *Supersymmetric optical structures.* Physical review letters, 2013. **110**(23): p. 233902.
[80] Heinrich, M., et al. *Supersymmetric mode converters*. in *Photonic Fiber and Crystal Devices: Advances in Materials and Innovations in Device Applications IX*. 2015. SPIE.
[81] Buda, M., et al., *Improvement of the kink-free operation in ridge-waveguide laser diodes due to coupling of the optical field to the metal layers outside the ridge.* IEEE Photonics Technology Letters, 2003. **15**(12): p. 1686-1688.
[82] Leidner, J.P. and J.R. Marciante, *Beam quality improvement in broad-area semiconductor lasers via evanescent spatial filtering.* IEEE Journal of Quantum Electronics, 2012. **48**(10): p. 1269-1274.
[83] Wenzel, H., et al., *Suppression of higher-order lateral modes in broad-area diode lasers by resonant anti-guiding.* IEEE Journal of Quantum Electronics, 2013. **49**(12): p. 1102-1108.

[84] Gao, C., et al., *Analysis of optical gain and threshold current density of 980 nm InGaAs/GaAs compressively strained quantum well lasers.* Computational materials science, 2004. **30**(3-4): p. 296-302.
[85] Al-Taiy, H., et al., *Ultra-narrow linewidth, stable and tunable laser source for optical communication systems and spectroscopy.* Optics Letters, 2014. **39**(20): p. 5826-5829.
[86] Wicht, A., et al. *Narrow linewidth diode laser modules for quantum optical sensor applications in the field and in space*. in *Components and packaging for laser systems III*. 2017. SPIE.
[87] Kadlec, E.A., et al. *Coherent Lidar for Autonomous Vehicle Applications*. in *2019 24th OptoElectronics and Communications Conference (OECC) and 2019 International Conference on Photonics in Switching and Computing (PSC)*. 2019.
[88] Moody, G., et al., *2022 roadmap on integrated quantum photonics.* Journal of Physics: Photonics, 2022. **4**(1): p. 012501.
[89] Mitra, D., K. Leung, and T. Zelevinsky, *Quantum control of molecules for fundamental physics.* Physical Review A, 2022. **105**(4): p. 040101.
[90] Stern, B., et al., *Compact narrow-linewidth integrated laser based on a low-loss silicon nitride ring resonator.* Optics letters, 2017. **42**(21): p. 4541-4544.
[91] Tran, M.A., D. Huang, and J.E. Bowers, *Tutorial on narrow linewidth tunable semiconductor lasers using Si/III-V heterogeneous integration.* APL photonics, 2019. **4**(11).
[92] Huang, D., et al., *High-power sub-kHz linewidth lasers fully integrated on silicon.* Optica, 2019. **6**(6): p. 745-752.
[93] Komljenovic, T., et al., *Widely tunable narrow-linewidth monolithically integrated external-cavity semiconductor lasers.* IEEE Journal of Selected Topics in Quantum Electronics, 2015. **21**(6): p. 214-222.
[94] Fan, Y., et al., *Hybrid integrated InP-Si 3 N 4 diode laser with a 40-Hz intrinsic linewidth.* Optics express, 2020. **28**(15): p. 21713-21728.
[95] Guo, Y., et al., *Hybrid integrated external cavity laser with a 172-nm tuning range.* APL Photonics, 2022. **7**(6).
[96] Fan, Y., et al., *Optically Integrated InP–Si $ _3 $ N $ _4 $ Hybrid Laser.* IEEE photonics journal, 2016. **8**(6): p. 1-11.
[97] Gil-Molina, A., et al. *Robust hybrid III-V/Si 3 N 4 laser with kHz-linewidth and GHz-pulling range*. in *2020 Conference on Lasers and Electro-Optics (CLEO)*. 2020. IEEE.
[98] Tang, L., et al., *Hybrid integrated low-noise linear chirp frequency-modulated continuous-wave laser source based on self-injection to an external cavity.* Photonics Research, 2021. **9**(10): p. 1948-1957.
[99] Lihachev, G., et al., *Low-noise frequency-agile photonic integrated lasers for coherent ranging.* Nature Communications, 2022. **13**(1): p. 3522.
[100] Corato-Zanarella, M., et al., *Widely tunable and narrow-linewidth chip-scale lasers from near-ultraviolet to near-infrared wavelengths.* Nature Photonics, 2023. **17**(2): p. 157-164.

[101] Shim, E., et al., *Tunable single-mode chip-scale mid-infrared laser*. Communications Physics, 2021. **4**(1): p. 268.
[102] Blumenthal, D.J., et al., *Silicon nitride in silicon photonics.* Proceedings of the IEEE, 2018. **106**(12): p. 2209-2231.
[103] Liu, J., et al., *High-yield, wafer-scale fabrication of ultralow-loss, dispersion-engineered silicon nitride photonic circuits.* Nature communications, 2021. **12**(1): p. 2236.
[104] Burham, N., A.A. Hamzah, and B.Y. Majlis. *Effect of isopropyl alcohol (IPA) on etching rate and surface roughness of silicon etched in KOH solution*. in *2015 IEEE Regional Symposium on Micro and Nanoelectronics (RSM)*. 2015. IEEE.
[105] Burham, N., et al. *Effect of temperature on the etching rate of nitride and oxide layer using Buffered Oxide Etch*. in *2016 International Conference on Advances in Electrical, Electronic and Systems Engineering (ICAEES)*. 2016. IEEE.
[106] Arbabi, A. and L.L. Goddard, *Measurements of the refractive indices and thermo-optic coefficients of Si 3 N 4 and SiO x using microring resonances.* Optics letters, 2013. **38**(19): p. 3878-3881.
[107] Elshaari, A.W., et al., *Thermo-optic characterization of silicon nitride resonators for cryogenic photonic circuits.* IEEE Photonics Journal, 2016. **8**(3): p. 1-9.
[108] Numai, T. and T. Numai, *Fundamentals of semiconductor lasers*. 2015: Springer.
[109] Mercer, L.B., *1/f frequency noise effects on self-heterodyne linewidth measurements.* Journal of Lightwave Technology, 1991. **9**(4): p. 485-493.
[110] Raja, A.S., et al., *Electrically pumped photonic integrated soliton microcomb.* Nature communications, 2019. **10**(1): p. 680.
[111] Chang, H., et al., *High-precision, accurate optical frequency reference using a Fabry–Perot diode laser.* Review of Scientific Instruments, 2017. **88**(6).